The utilisation of µ-computed tomography for the investigation of equine papilla/lamella-associated foot lameness

Emily Katy Paul, BSc.

Thesis submitted to the University of Nottingham for the degree of Master of Research

July 2016

Abstract

Equine foot lameness is a prevalent condition, with high welfare and economic impacts. As the most common cause for equine euthanasia, foot pathologies associated with the lamellae, termed ‘laminitis’, are of particular concern. Taking a novel, interdisciplinary approach, micro-computed tomography was utilised to investigate the full extent of the equine foot in order to gain insight on its structures in a normal state and information on the pathological changes associated with laminitis-like lesions.

Equine feet were collected from an abattoir and the blood vessels flushed with phosphate-buffered saline before pressurised perfusion with paraformaldehyde. Micro-computed tomography was performed on the whole feet and on sections cut from the coronet region in a laboratory scanner, and a region of interest scan of the dorsal coronet region was carried out on a whole foot at a synchrotron radiation source. The whole-foot tomographic images procured from the laboratory scanner were assessed for indicators of hoof deformity and chronic laminitis, and analyses of the bone and the vasculature were carried out. The synchrotron-sourced images were used to assess the viability of future research.

Positive dorsal hoof wall curvature was found to be a primary physical descriptor, correlating positively with rotation of the third phalanx. Changes in the structure and morphology of the bone, in terms of curvature, cortical thickness and trabecular pore enlargement, were observed alongside increasing curvature, and indicated that force rebalances within the foot occurred in conjunction with the capsular changes, and put the direction of causality between lamellar damage and pathomorphological changes such as the rotation of the third phalanx under question. Finally, the visibility of the vasculature and of important microstructures, such as the dermal papillae, showed the scope for future research.

Acknowledgements

As, with some disbelief, I draw the writing of my thesis to a close, I think back on the rollercoaster of a journey the last year has been, and on the many wonderful people who have enabled me to reach this point. I would like to start by thanking my supervisors Dr Cyril Rauch and Dr Catrin Rutland – for two more inspiring and supportive supervisors I could not have hoped. Ever smiling in the face of adversity, their belief in me did not once seem to falter. So merci Cyril, pour bien plus que ce que tu m'a appris sur la physique et les maths, and thank you Catrin for your unwavering support, not just in my work.

From the vet school, I would also like to thank Dr Stuart Pain, without whom I would never have met Cyril and been involved with this project; Dr Julia Kydd for her support and advice when the going got tough; Dr Richard Payne for patiently teaching me the art of blood vessel perfusion and for being enthusiastic about everything; the technical staff in the dissection and research labs for allowing me to make a horrible mess; Ramzi Al-Agele for all his help with hoof collection and preparation, and for being such an interesting, hard-working person to study alongside; Vinnie the friendly cleaner who told me not to hope, but to believe; and my fellow postgraduates, a supportive bunch who are always a pleasure to be around. At the University of Nottingham more broadly, I wish to thank Dr Craig Sturrock and Brian Atkinson at the Hounsfield Facility for the many feet that they carefully scanned, for allowing me to use their big computers, and for explaining the basics of image analysis; Chris Barr, Helen Coombes and everyone from the University's amazing support services; and the Weston Award Scholarship for funding my studies. Outside of the University, I would very much like to thank Dr Martin Nelson for such patient explanations of the maths; Tom Ryan, the most inspiring farrier there ever was and a true friend to horses; Professor Pat Harris for the interesting laminitis conversations, and Waltham Pet Nutrition as a whole for enabling the purchase of an imaging computer; and Michael Drakopoulos, Robert Atwood and Nghia Vo at Diamond Light Source for all your hard work to get that data, for answering all of my daft questions, for giving me and Cyril the amazing but wacky opportunity to take a horse's foot to a particle accelerator, and for the overall phenomenal experience that I had there.

And now to the family. I would like to thank my parents for the unconditional love and support they always show me, no matter what I choose to do. I have learnt many things this year, and how lucky I am to have them is among the top. I am grateful my sisters Helen and Julia, their husbands/partners James and Martin (you get two mentions!), and my two little nieces Melissa and Imogen, for their support and interest. I would also like to thank my boyfriend Ben for all his support and encouragement, for putting up with me through the effects of

thesis writing, for loving me and all my crazy ways, for truly understanding me, and for giving me a sense of purpose and the feeling of truly belonging that I so needed. Finally, I must thank the creatures: Ratty, Pingu and Marinski for being ever-entertaining, always there, and (surprisingly) wise; Robin for being the bumbly ginger monster that I so love; Sapphire, who I miss dearly; Marina, the cuddliest cat in the world who knows just how to help; Orrie, the cheery little fellow with the big attitude; and Tequila, my love and inspiration.

Abbreviations

Z	Atomic number
BM	Basement membrane
CV	Coefficient of variation
CDET	Common digital extensor tendon
CT	Computed tomography
DDFT	Deep digital flexor tendon
Dll4	Delta-like ligand 4
P1	First phalanx
μ	Linear attenuation coefficient
MIL	Mean intercept length
M-CT/μ-CT	Micro-computed tomography
PFA	Paraformaldehyde
PTH	Parathyroid hormone
PBS	Phosphate-buffered saline
E	Photon energy
I	Photon intensity
RGB	Red green blue colour model
ROI	Region of interest
P2	Second phalanx
SD	Standard deviation
SDFT	Superficial digital flexor tendon
P3	Third phalanx
VEGF	Vascular endothelial growth factor

Contents

Abstract 1
Acknowledgements 2
Abbreviations 4
1 Introduction 8
1.1 Anatomy of the Equine Foot 9
1.2 Bones of the Equine Foot 13
1.2.1 Physiology of Bone 13
1.2.2 Anatomy of the Third Phalanx 17
1.3 Vascularisation of the Equine Foot 19
1.3.1 Vascular Physiology 19
1.3.2 Vascular Anatomy of the Equine Foot 20
1.4 Papillae, Lamellae, and Growth of the Equine Hoof 22
1.5 Lameness and Laminitis 24
1.6 The Use of X-ray Micro-Computed Tomography 26
1.7 Aims and Hypotheses 29
2 Materials and methods 31
2.2 Foot collection and preparation 31
2.3 CT scanning 33
2.3.1 Laboratory Micro-Tomography 33
2.3.2 Synchrotron Micro-Tomography 34
2.4 CT image processing 35
2.4.1 Hoof Orientation and Planar Adjustments 35
2.4.2 Bone Segregation 35
2.4.3 Vasculature Isolation 36
2.4.4 Microstructures 36
2.5 Physical Descriptors 39
2.5.1 Dorsal Curvature 39
2.5.2 Dorsal Angle 40
2.5.3 Curvature and Angle Relationship 41
2.5.4 Displacement of the Third Phalanx 44
2.6 Bone Analysis 47

2.6.1 Bone Curvature 47
2.6.2 Cortical Bone Thickness 47
2.6.3 Trabecular Bone Distortion 47
2.7 Vasculature Analysis 51
2.8 Microstructure Analysis 52
2.9 Immunohistochemistry 53
2.10 Anatomical Image Rendering 54
2.11 Statistical Analysis 55
3 Results 56
3.2 Physical Descriptors 56
3.2.1 Dorsal Wall Curvature and Angle 56
3.2.2 Displacement of the Third Phalanx 57
3.3 Bone 59
3.3.1 Bone Rendered CT Images 59
3.3.2 Bone Curvature 66
3.3.3 Cortical Bone Thickness 66
3.3.4 Trabecular Bone Distortion 71
3.4 Vasculature 73
3.4.1 Vasculature Rendered CT Images 73
3.4.2 Software Development 78
3.4.3 Vasculature Diameter 78
3.5 Lamellae, Papillae and Keratogenesis 80
3.5.1 Microstructure Rendered CT Images 80
3.5.2 Papilla Morphology 82
3.5.3 Coronary Epidermal Cell Proliferation 84
4 Discussion 86
4.2 Characterisation of Pathomorphology 86
4.3 Bone Remodelling 89
4.4 Vascular Remodelling 93
4.5 Papilla Morphology and Keratogenesis 94
4.6 Future Research 96
4.6.1 Laboratory M-CT 96

4.6.2 Synchrotron M-CT 97
5 Conclusions 100
Publications 102
References 103
Appendices 108
Appendix I – Curvature/Angle Relationship Calculations 108
Appendix II – Anatomical Movies DVD 110
Appendix III – Immunohistochemistry Protocol 111

1 Introduction

Equine laminitis is a debilitating and destructive disease of the foot that can affect any horse, pony or donkey; it has a high welfare and economic bearing, being the predominant cause for equine euthanasia in the UK (Ireland et al., 2011, Rendle, 2014, Anonymous, 2004). Despite intense research efforts, very little is understood about the condition, perhaps due in part to the complexity of the equine foot, which has a multiple organ system composition (Engiles, 2010).

As the term implies, laminitis affects the lamellae of the feet, connecting the horny hoof capsule and the bone beneath (Boden, 2007). Many theories surrounding the aetiology of the observed pathological changes to the lamellae during an episode of laminitis exist (Heymering, 2010). Little consideration has, however, been given to the biophysical effects of the growth of the solid hoof wall, and its movement with respect to the internal components of the foot. In order to investigate this notion, it is necessary to understand the anatomy and histology of the tissue and vasculature of the normal hoof. This introduction explores what is presently known, and examines the techniques employed throughout this research.

1.1 Anatomy of the Equine Foot

As perissodactyls, or odd-toed ungulates, horses have a strong outer capsule, the hoof, protecting the internal structures of each single-digit foot (Fig. 1.1) (Prothero, 2001).

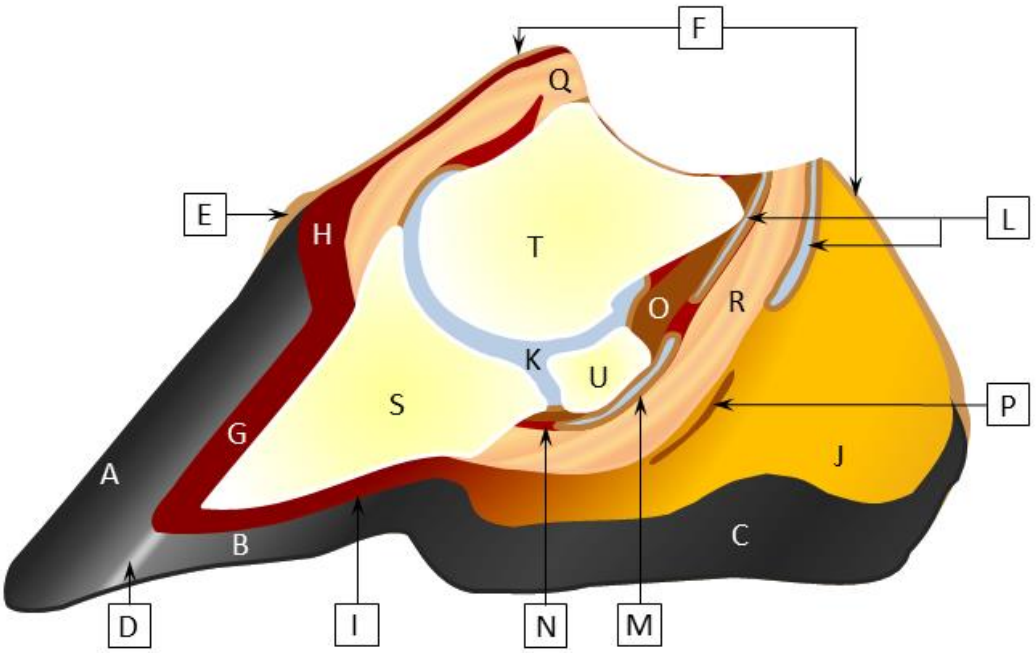


Figure 1.1: Anatomy of the equine foot. This diagram shows the principal anatomical structures of the horse's foot from a sagittal view. The letters indicate the following anatomical features:

- **A.** Hoof Wall
- **B.** Sole
- **C.** Frog
- **D.** White Line
- **E.** Periople
- **F.** Skin
- **G.** Lamellar Corium
- **H.** Coronary Corium
- **I.** Solar Corium
- **J.** Digital Cushion
- **K.** Distal Interphalangeal Joint
- **L.** Distal Synovial Sheaths
- **M.** Navicular Synovial Bursa
- **N.** Distal Navicular Ligament
- **O.** Navicular Suspensory Ligament
- **P.** Distal Digital Annular Ligament
- **Q.** Common Digital Extensor Tendon
- **R.** Deep Digital Flexor Tendon
- **S.** Third Phalanx
- **T.** Second Phalanx
- **U.** Navicular Bone

Source information includes: (Davies and Philip, 2007) and (Goody, 2000).

The hoof is composed of horn, derived from epidermal tissue which has been keratinised to a varying extent (Pollitt, 2004). Horn is largely arranged into a series of parallel microscopic tubules, interconnected by intertubular horn (Pollitt, 2007). This structure is particularly visible in the hoof wall (Fig. 1.1 and 1.2 and Movie 1 in appendix II), which plays a substantial role in load-bearing, and encapsulates almost the entire circumference of the foot, curling inwards towards the rear to form the bars which provide additional support to the heels

(Goody, 2000). Encasing the palmar/plantar surface of the foot is the sole, which is concave and has a similar, but softer and more flexible, composition to the hoof wall (Goody, 2000). The hoof joins to the skin at the coronet where it is protected by a waterproof band of soft tubular horn, the periople (Davies and Philip, 2007). Connecting the periphery of the sole to the hoof wall is the white line, which is derived from the epidermal lamellae and is highly elastic. Composed of supple, incompletely keratinised horn, the frog is an elastic triangular shaped structure which plays roles in shock absorption, blood circulation, and in slip prevention (Goody, 2000). The frog extends inwards to the digital cushion which, being composed of poorly vascularised adipose tissue embedded in a fibroelastic mesh, acts to further enhance the frog's shock absorbing and blood pumping properties (Davies et al., 2007, Goody, 2000). The digital cushion is segregated from the deep digital flexor tendon (DDFT) by the presence of the distal digital annular ligament (Goody, 2000).

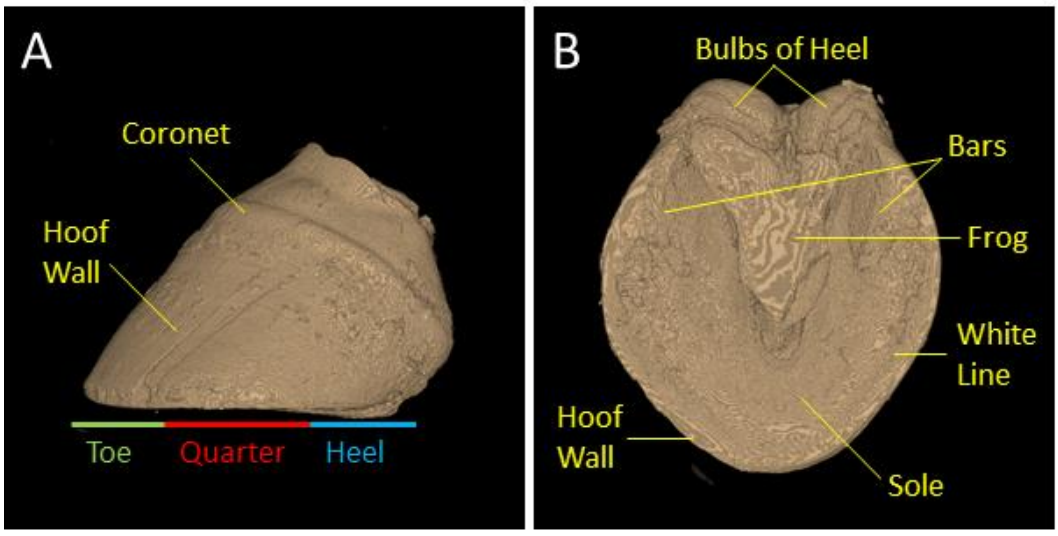


Figure 1.2: Anatomy of the hoof capsule. 3D reconstructions of CT images showing (**A**) a lateral/medial view, and (**B**) a palmar/plantar view. Images obtained from the study, but source information includes (O'Brien, 2007).

The bones of the equine foot comprise the third phalanx (P3), the second phalanx (P2), and the navicular bone (see Fig 1.1). P3, also referred to as the pedal or coffin bone, is the foot's principal bone, occupying its most distal position, and attaching to the hoof capsule via the lamellar and solar coria (Davies et al., 2007). P3 has a very particular shape owing to its function of supporting and stabilising the hoof capsule, and is highly porous due to the prolificacy of nutrient foramina (Davies et al., 2007). P2, or short pastern, forms the proximal interphalageal, or pastern, joint with the first phalanx (P1), and the distal interphalangeal, or coffin, joint with P3 (Goody, 2000). Its short, almost cuboidal, composure makes P2 resilient to a broad range of stresses (Davies et al., 2007). The navicular, or distal sesamoid bone, is a small, smooth bone

located caudal to the distal interphalangeal joint. Coated ventrally in smooth fibrocartilage, it fulfils a pulley-like role, allowing the DDFT to glide smoothly under the distal interphalangeal joint without interference from the other bones (Goody, 2000). The navicular synovial bursa and distal synovial sheathes further aid the smooth action of the DDFT via the secretion of lubricating synovial fluid (Goody, 2000).

Along with the DDFT, which descends from the deep digital flexor muscle in the forearm to the flexor surface of P3, the superficial digital flexor tendon (SDFT) forms part of the back tendon pair which permits flexion of the interphalangeal joints (Goody, 2000, Davies and Philip, 2007). Descending from the superficial digital flexor muscle in the forearm, the SDFT attaches to the proximal surfaces of P1 and P2 (Goody, 2000). Responsible for the extension of the interphalangeal joints is the common digital extensor tendon (CDET) (Davies and Philip, 2007). Stemming from the long digital extensor muscle proximal to the knee, the CDET descends the leg dorsally, terminating at the extensor process of P3 with projections into P1 and P2 (Goody, 2000).

While the DDFT and SDFT permit flexion of the foot's interphalangeal joints and the CDET allows their flexion, the presence of lateral and medial collateral ligaments limits the joints' adduction and abduction respectively (Davies and Philip, 2007). The collateral ligaments attach to notches on the distal and proximal edges of P1 and P2 correspondingly in the case of those of the proximal interphalangeal joint, and on the distal and proximal edges of P2 and P3 respectively for those of the distal interphalangeal joint (Davies and Philip, 2007). The position of P3 is also maintained by three pairs of chondral ligaments, attaching to the medial and lateral cartilages of P3 (Goody, 2000). The navicular bone is held in place by the navicular suspensory ligaments which anchor to the distal edge of P1, just dorsal to the collateral ligament attachments, and converge at the navicular bone, forming the distal navicular ligament which terminates at P3 (Goody, 2000).

The coria are the richly vascularised and innervated dermal regions lying between and supporting the skeletal structures and the epidermal hoof capsule (Pollitt, 2010). The coronary corium runs along the proximal edge of the hoof wall, with each hoof wall tubule growing around small, finger-like papillae projecting from the coronary corium which provide nourishment to the proliferative epidermal cells, maintaining hoof growth (Pollitt, 2004). The solar corium is similar in structure and function to the coronary corium, with papillae enabling the growth of the sole (Pollitt, 2004). The lamellae of the lamellar corium, commonly referred to as the sensitive or the dermal lamellae, form, together with the epidermal/insensitive lamellae of the inner hoof wall with

which they interlock, the suspensory apparatus of the third phalanx, suspending P3 within the hoof capsule (Pollitt, 2010). Distal to each dermal lamella is a set of papillae, the terminal papillae, which form the soft, elastic white line which binds wall to sole (Pollitt, 2004).

The macroscopic ridge-like primary lamellae, of which there are some 550 to 600 epidermal/dermal interlocking pairs in parallel descent within each foot, provide a large surface area between the epidermis and the dermis for the suspension of P3 (Pollitt, 2007). Each primary lamella bears a further 150 to 200 microscopic secondary lamellae and, collectively, the primary and secondary lamellae create a surface area for attachment of around $0.8m^2$ (Pollitt, 2007).

Between the dermal and epidermal tissues of the foot lies the basement membrane (BM), a strong, uninterrupted sheet of extracellular matrix (Pollitt, 2004). Epidermal basal cells are attached to the BM on its border with the hoof epidermis (Pollitt, 2004). On its inner, dermis-bordering side, a vast array of collagen-rich connective tissue strands projecting from the periosteum of P3 intertwine with the BM's lattice, ensuring the structural integrity of the dermal structures (Pollitt, 2004). The BM is folded into ridges along the longitudinal axes of the primary lamellae, forming the secondary lamellae, and the coronary and terminal papillae, increasing the surface area for the attachment of proliferative epidermal basal cells (Pollitt, 1994).

1.2 Bones of the Equine Foot

1.2.1 Physiology of Bone

Bone is a complex, dynamic tissue that has the ability to grow ontogenically, to repair after damage, and to adaptively respond to a variety of exogenous and endogenous stimuli (Clarke, 2008). Of particular interest to this study is the bone's osteogenic response to mechanical strain: evidence of such osteogenic remodelling could provide post-mortem elucidation of the incidence and location of imbalances in physical stress. This not only serves to support the principal grounds of this study that interlink laminitis, physical forces and hoof growth, but may also challenge some of the current concepts in the pathophysiology of laminitis, the causative implication of the lamellae being the most notable.

Composed of a mineralised organic matrix in which the cells responsible for its formation and rejuvenation are embedded, osseous tissue, through its unique physiological and biochemical properties, enables bones to perform a multitude of functions within the animal's body. The organic matrix, or osteoid (Petersen, 2007), is formed principally of type-I collagen (~95% (Bayliss et al., 2012)) which affords the bone its tensile strength, alongside trace amounts of other collagens, in addition to non-collagenous proteins whose predominant purpose is to permit the mineralisation of the matrix. The chief mineral salt found in osseous tissue is a form of hydroxyapatite [$Ca_{10}(PO_4)_6(OH)_2$] which, bound to the matrix proteins, renders the tissue resistant to compressive forces (Clarke, 2008).

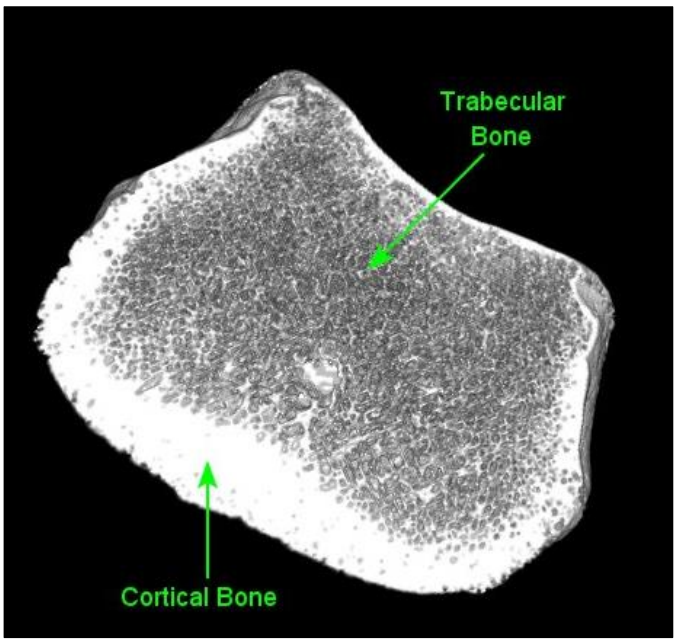


Figure 1.3: CT reconstruction of a bone. Transverse section of the second phalanx, illustrating the macrostructure of cortical and trabecular bone.

Adding to the physical strength that the biochemical makeup affords to the bone is its architectural design. On the nanoscale, the platelet-shaped hydroxyapatite crystals lie in a staggered formation within the osteoid fibrils (with a mineral to matrix ratio of around 1:2 on a volumetric basis), which allows the dissipation of tensile and shear forces as well as a degree of crack tolerance (Gao, 2006). The microscale building blocks of the bone, osteons, are borne from the complex arrangement of this nanoscale material, and are structured into either cortical or trabecular bone (Fig. 1.3). Cortical, or compact, bone forms the dense outer proportions of the bone and, in the human, accounts for 80% of the total skeletal mass (Iolascon et al., 2013, Clarke, 2008). Cortical osteons (Fig. 1.4), or Haversian systems, are tubular structures consisting of a central channel (Haversian canal), through which a nerve and blood supply are provided, surrounded by coaxial lamellae of mineralised bone matrix which incorporate a number of voids, in the form of lacunae and canaliculi, inhabited by cells (Clarke, 2008). The remaining 20% of the osseous tissue is in the form of trabeculae (from the Latin *trabs*, meaning "beam" (Stevenson and Waite, 2011))which provide structural support, in a buttress-like manner, to the surrounding cortex. Trabecular osteons, or packets, are similar in their lamellar architecture to those of the cortex, but are smaller in size and semi-lunar in shape (Clarke, 2008). This hierarchical design, a common (if not omni-existent) phenomenon in biological materials, provides bones with the physical strength they need to fulfil their roles in structural support, the protection of underlying

organs, and in providing leverage to muscles and tendons, facilitating movement (Clarke, 2008, Gao, 2006, Wegst et al., 2015).

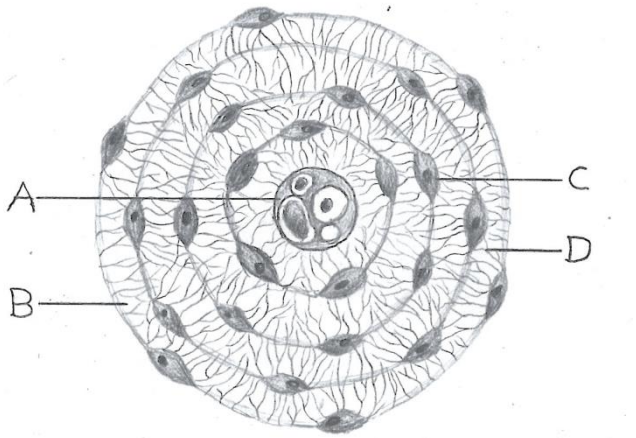


Figure 1.4: Schematic of a cortical osteon. (**A**) represents a Haversian canal incorporating a neurovascular bundle, (**B**) a lamella, (**C**) a lacuna containing an osteocyte, and (**D**) canaliculi.

The remodelling and general renewal of the bone is mediated by three cell types: osteoblasts, osteoclasts and osteocytes (Nakahama, 2010). Osteoblasts are mononucleated cells formed by the differentiation of mesenchymal stem cells, and are responsible for the synthesis of osteoid and its subsequent mineralisation (Bayliss et al., 2012). They reside principally in the endosteum – the vascularised cellular lining of the internal proportions of the bone, covering the walls of the Haversian canals, and the trabeculae and medullary cavity where it separates the bone matrix from the marrow (Pazzaglia et al., 2014) – and, alongside their incompletely-differentiated precursors and fibroblasts, the cambial layer of the periosteum (Clarke, 2008) – a vascularised and innervated structure consisting of an outer fibrous layer comprising fibroblasts, collagen and elastin, and the discrete inner cambium that coats the bone's exterior (Allen et al., 2004). Osteoclasts are multinucleated macrophagic cells derived from phagocytes in the haematopoietic bone marrow, and carry out bone resorption in localised areas of the bone surface to which they adhere upon activation (Pearson and Lieberman, 2004). Osteocytes, which inhabit the lacunae of the osteons and have multiple cytoplasmic processes which traverse the osteons' canaliculi, are the result of the terminal differentiation of osteoblasts that have become entrapped within the bone matrix that they have synthesised (Bayliss et al., 2012). They act as mechanoreceptors, communicating with the osteogenic/osteolytic cells via gap junctions at the extremities of their

cytoplasmic processes, and play a regulatory role in the bone synthesis/resorption cycle (Bayliss et al., 2012).

Concomitant to the physical need for the bone to be able to remodel for general maintenance, repair, and for increasing structural strength in response to stimuli, are the roles in pH balance and mineral homeostasis that the synthesis/resorption cycle affords (Clarke, 2008). While under normal physiological circumstances the pH of blood and extracellular fluid is maintained within narrow parameters by the removal and excretion of protons by the kidneys and lungs, a multitude of physiologically adverse conditions (e.g. kidney disease or severe exercise) can lead to acidosis (Arnett, 2003). The basicity of hydroxyapatite renders bone an emergency reservoir for base, buffering the acidity with the products of osteoclastic resorption. This mechanism is enabled by the osteoclast's stimulation at low pH, a peculiarity from a general cellular point of view, and the osteoblast's synergistic inhibition (Arnett, 2003). In a similar vein, bone acts as a reservoir for calcium and phosphorus, making them available for the maintenance of mineral homeostasis. Calcium and phosphorus are vital for a plethora of biological functions, and their homeostasis is under the endocrine regulation of the parathyroid glands, thyroid gland, and the kidney which, through the intermediary of parathyroid hormone (PTH), calcitriol (1,25-dihydroxyvitamin D, a hormone derived from vitamin D), and calcitonin respectively, affect the intestinal absorption, renal reabsorption and bone synthesis/resorption mechanisms (Petersen, 2007, Peacock, 2010). The parathyroid glands, which express Ca^{2+}-sensing receptors, secrete PTH in response to a reduction in circulating calcium ions. PTH acts in the kidney to decrease phosphate and increase calcium reabsorption, and in the bone by stimulating osteocytic and osteoclastic activity (Peacock, 2010).

Bone also acts as reservoir for growth factors and cytokines, which are released during bone resorption and take effect either locally or systemically (Delany and Canalis, 2001). Along with the effects that these growth factors and cytokines may exert on other tissue cell types, such as the endothelial cells of the vasculature (see section 1.3 below), they play important roles in bone formation and resorption, including: insulin-like growth factors, transforming growth factors, and bone morphogenic proteins as growth factors promoting osteogenesis; epidermal growth factor, granulocyte-macrophage colony-stimulating factor, macrophage-colony stimulating factor, and tumour necrosis factor as growth factors stimulating osteolytic resorption; platelet-derived growth factor and fibroblastic growth factor which have contributory effects to both bone formation and resorption; prostaglandins and leukotrienes as osteolysis-stimulating cytokines; and interleukins that may directly or indirectly

stimulate either bone formation or resorption depending on the interleukin family in question (Kini and Nandeesh, 2012).

Strong links exist between the skeletal and vascular systems and, along with a strong vascular and nerve presence in the periosteum, numerous neurovascular bundles enter the bone through nutrient foramina, descend and ascend the canals of Haversian systems, and enter medullary cavity through Volkmann's Canals (Stocum, 2012). The two systems are interdependent in that the bone relies on the vasculature for the delivery of oxygen and nutrients and that, modulated by osteoblasts, haematopoiesis takes place in the bone marrow (Taichman, 2005).

1.2.2 Anatomy of the Third Phalanx

As the primary bone in the foot, P3 was of particular interest in this study. P3 has a number of visibly distinct anatomical areas, each bordering a different tissue type. These anatomical areas include tendon and ligament attachment sites, articular surfaces, and corium-bound areas. As tendon attachment sites, the extensor process (Fig. 1.5A) and the flexor surface (Fig. 1.5B) accommodate the CDET and the DDFT respectively (Davies and Philip, 2007). Lateral and medial notches on the proximal edge of P3 act as the attachment areas for the collateral ligaments (Fig. 1.5A) (Davies and Philip, 2007). As components of the distal interphalangeal joint, the smooth areas faceting P3 proximally are the articular surfaces (Fig. 1.5B) that abut P2 and the navicular bone (Davies and Philip, 2007). The lamellar surface (Fig. 1.5A) of P3 lies below the hoof wall, to which it is attached through the intermediary of the dermal and epidermal lamellae. Similarly, the solar surface (Fig. 1.5A) attaches to the sole of the foot via the solar corium (Davies and Philip, 2007). The solar margin (Fig. 1.5A) forms the narrow, ridge-like border between the lamellar and solar surfaces, and acts as a base for the anchorage of the terminal papillae (Davies and Philip, 2007). Extending from the most dorsal to the most distal proportions of the bone, the lamellar and solar surfaces and margin underlie both the toe and quarter areas of the hoof, and the regions were categorised as such for this study.

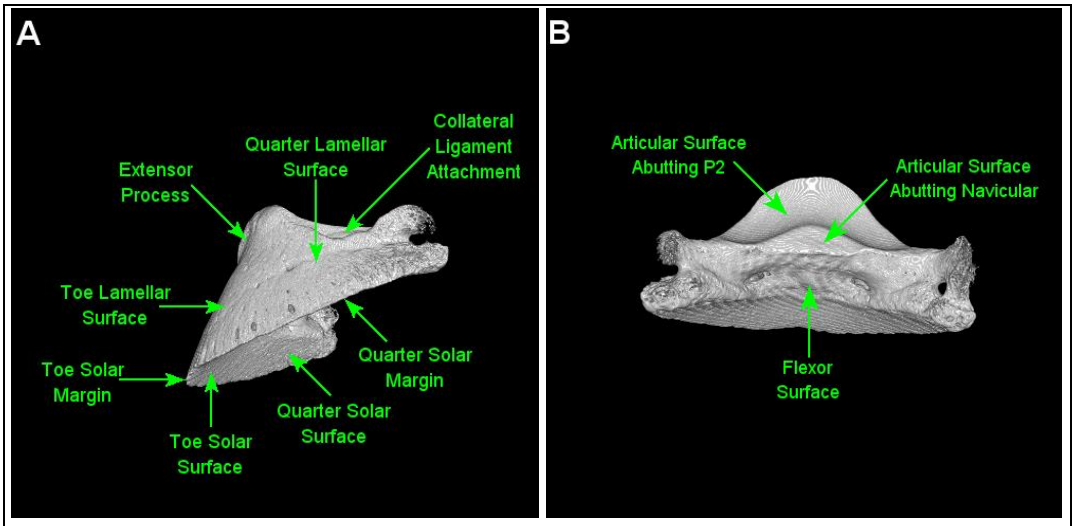


Figure 1.5: CT reconstructions of the third phalanx, with (**A**) showing the toe and quarter solar and lamellar surfaces and margins and the extensor process and collateral ligament attachments, and (**B**) the flexor surface and the articular surfaces abutting the second phalanx and the navicular bone. Images were taken as part of the study, but source information includes (Davies and Philip, 2007).

1.3 Vascularisation of the Equine Foot

1.3.1 Vascular Physiology

Developed for the transport of dissolved gases, nutrients, waste, signalling chemicals such as hormones, and immune cells to and from the many organs and tissues of the higher animal's body, blood vessels have evolved to adaptively respond to the demands of their environment (Stapor et al., 2014). As mentioned above, the skeletal and vascular systems are closely interlinked, and their coexistence is synergistic in that the aforementioned growth and development processes that take place in the bone are enabled by its vascularisation and innervation, that its marrow is the seat of haematopoiesis (Taichman, 2005), and that its mineralised matrix acts as a reservoir for growth factors, such as vascular endothelial growth factor (VEGF), that regulate angiogenesis (Kini and Nandeesh, 2012). The increased demand for oxygen, borne from a heightened metabolic rate, is true of any growing tissue, including the epidermis (Stocum, 2012). This, along with the various circulatory peculiarities, such as extreme vasoactivity, the formation of arteriovenous anastomoses, coagulatory disorders, anomalies in hydrostatic pressure, and mechanical damage of the vasculature, that have been suggested as implicated in the pathogenesis of laminitis (Heymering, 2010), render the exploration of the foot's vascularisation relevant to this study.

A key form of the above-mentioned vascular adaptation, and one of particular interest in the discussion of tissue growth, is angiogenesis, which involves the remodelling of capillary networks to form new capillaries, veins and arteries (Gilbert, 2010). Triggering angiogenesis is hypoxia, where tissue oxygenation falls below metabolic rate due to development (e.g. ontogeny), wound healing, or pathogenic processes (Murray and Wilson, 2001). Oxygen depletion is sensed by the endothelial and smooth muscle cells forming the blood vessel walls through a variety of mechanisms, and leads to the up-regulation of angiogenic genes encoding, for instance, signal proteins such as VEGF (Fraisl et al., 2009). Upon VEGF signal, tip cells, which are closely followed by stalk cells, sprout from the endothelial cells of the pre-existing blood vessels and form filopodia which, as receptor-covered cytoplasmic processes, are able to sense and respond to chemotropic cues (Phng and Gerhardt, 2009, Gilbert, 2010). Tip cells express Delta-like ligand 4 (Dll4), a transmembrane protein which binds to the Notch proteins prevalent across the membranes of stalk cells (Phng and Gerhardt, 2009). The activation of Notch by Dll4 prohibits the stalk cells' responsiveness to VEGF, preventing the overproduction of spouting vessels (Phng and Gerhardt, 2009, Gilbert, 2010). Led by the tip cells therefore, the newly-forming vessels course alongside VEGF gradients, vascularising and providing oxygen to tissues

that, for whichever the reason, are in a state of metabolic stress (Fraisl et al., 2009).

1.3.2 Vascular Anatomy of the Equine Foot

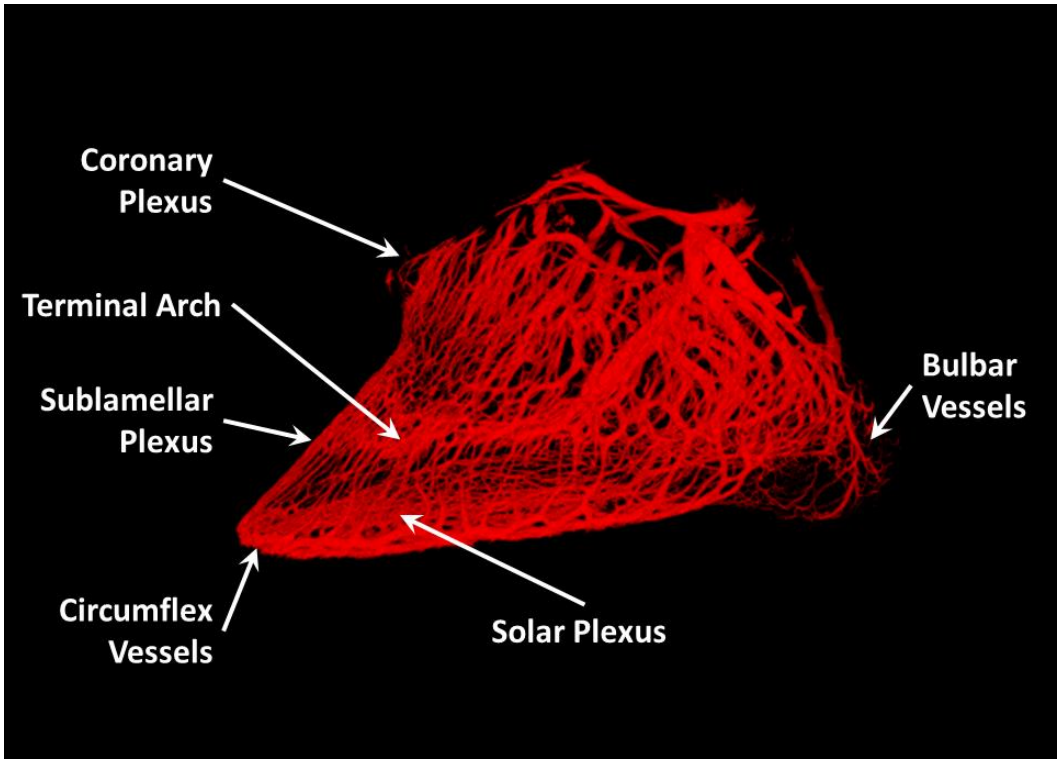


Figure 1.6: Vascularisation of the equine foot. Reconstruction of the vasculature of the equine foot from CT images, showing the coronary, sublamellar and solar plexuses, the terminal arch, the circumflex vessels of the sole, and the bulbar vessels. Images obtained from the study, but source information includes (D'Arpe and Bernardini, 2010, Baldwin and Pollitt, 2010).

The many components of the equine foot are sustained by the blood of the vast vascular network (Fig. 1.6) underlying the hoof capsule and coursing through the bones, fed through branches from the medial and lateral digital arteries and returning to general circulation via the medial and lateral digital veins (Pollitt, 2007). Descending the limb, the digital arteries send major branches towards the heels at the height of the proximal interphalangeal joint, leading to the bulbar vessels as well as feeding into the coria of the digital cushion and frog, and the caudal lamellar and coronary plexuses (Pollitt, 2010, Rucker, 2007). At mid-height of P2, the digital artery sends further branches which, meeting dorsally to form the coronary crescent (Rucker, 2007), supply blood to the coronary and dorsal sublamellar plexuses and nourishes the surrounding cartilages, the digital extensor tendon, and the distal interphalangeal joint (Pollitt, 2010). The final major branches exiting the digital arteries before their penetration of P3 and merging to form the terminal arch are the dorsal branches which, stemming at

the level of the navicular bone, course the parietal groove of P3 and feed the sublamellar plexus in the quarter and heel regions (Pollitt, 2007).

The terminal arch, formed by the conjoining of the medial and lateral digital arteries at the centre of P3, furcates to give rise to some four or five principal arteries exiting P3 through foramina on its dorsal surface, and eight to 10 through foramina around P3's solar margin, along with numerous smaller arteries (Pollitt, 2010). These supply the sublamellar plexus and, after anastomosing with arteries sprouting from the dorsal arch to form the circumflex artery, the solar plexus (Pollitt, 2010).

Venous drainage runs parallel to arterial supply, with sublamellar, solar and coronary venous plexuses alongside their arterial counterparts, and draining into the medial and lateral digital veins (Pollitt, 2007). The venous terminal arch, unlike its solitary arterial equivalent, comprises an axial and an abaxial parallel vein, interconnected with anastomoses (Mishra and Leach, 1983). On emergence from the foramina on the caudal surface of P3, an anastomosis connects the two branches of the axial parallel vein, providing drainage from vessels of the navicular bone, before the two parallel veins merge to form the medial and lateral terminal veins into which dorsal and ventral tributaries run (Mishra and Leach, 1983). At mid-height of P2, the terminal veins merge with veins draining from the three venous plexuses to form the digital veins which, at the level of the proximal interphalangeal joint, is joined by the branches returning from the bulbous vessels and caudal plexuses (Mishra and Leach, 1983, Pollitt, 2010).

1.4 Papillae, Lamellae, and Growth of the Equine Hoof

The wide range of hard keratin integumentary appendages across species, which include those that cover the body such as hair, fur, wool and feathers, those which grow on the head, known as horns, and those which cover the extremities of digits, such as nails, claws and hooves, all grow from cells surrounding dermal papillae (Chapman, 1986). Papillae are composed of connective tissues, and a central artery and vein, interconnected at the tip by an arteriovenous anastomose, and surrounded by a capillary plexus (Nasu et al., 1998).

As a commonality with the human nail, the equine hoof wall consists of three layers, or *strata*: the *stratum externum*, which forms the periople and the waxy, protective outer layer of the hoof wall (known as the *stratum tectorum* (Hill and Klimesh, 2009)); the *stratum medium*, descending from the coronet and consisting of the rigid capsular hoof wall; and the *stratum internum*, which takes the form of the dermal lamellae (Bragulla, 2003, Pollitt, 2010). The basal cells of each *stratum* are maintained by their own set of dermal papillae (Fig. 1.7).

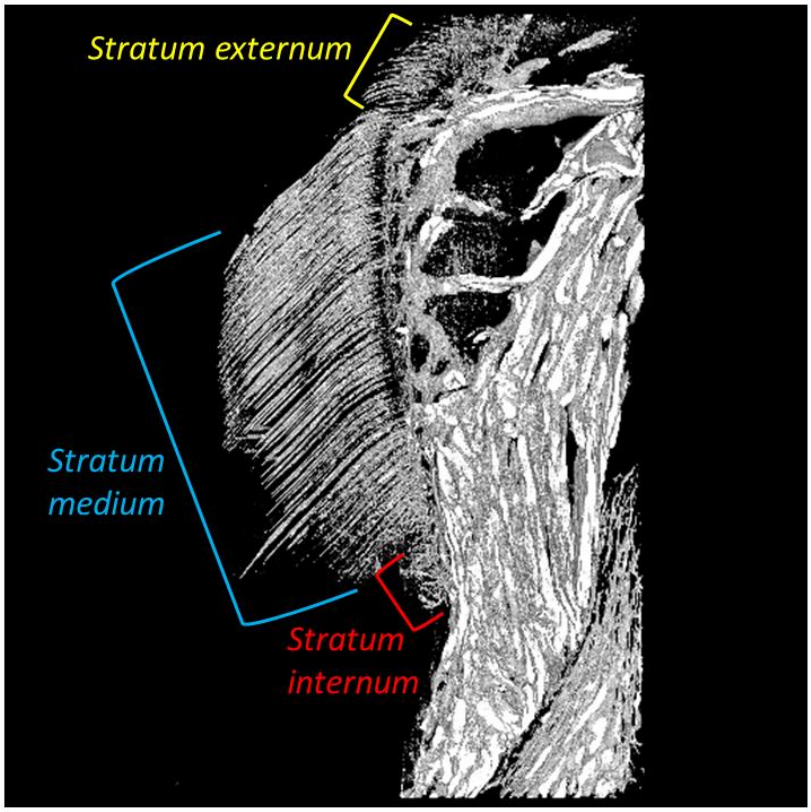


Figure 1.7: Papillae of the hoof wall strata. Rendered µ-CT image of a dorsal section of the coronary corium and dermal papillae, indicating the papillae of the *stratum externum*, *stratum medium*, and *stratum internum*. Image taken from the study but source information gained from (Bragulla, 2003, Pollitt, 2010).

Originating from basal epidermal cell layers arranged around the nurturing dermal papillae, hoof growth occurs throughout the duration of the horse's life to make good the inevitable losses through wear and tear borne of the peripatetic nature of the creature (Pollitt, 2007). In the basal layer, or *stratum basale*, keratinocyte progenitor cells, which are affixed to the basement membrane via hemidesmosomes (Pollitt, 2007), proliferate to give rise to a population of daughter keratinocytes, forming the *stratum spinosum* (Eurell, 2004). Differentiating as they migrate distally away from the dermis, maturation of the keratinocytes to form the corneocytes of the *stratum corneum* of the capsule proper involves their denuclearisation and keratinisation (Eurell, 2004). These corneocytes are continually added to the matrix of tubular and intertubular horn which forms the hoof capsule (Pollitt, 2010)

Enabling the smooth passage of the growing hoof wall over the parietal surface of P3 despite the strong adherence between the two are the particular properties of the Lamellae. While once a popular notion, the theory of lamellar flow, involving the continuous proliferation of epidermal cells surfacing the epidermal lamellae to allow the gradual descent of the hoof wall, has been discredited (Daradka and Pollitt, 2004). Instead, it is now believed that the tissue descent is permitted by the destruction and formation, through the mediation of matrix metalloproteinase proteolytic enzymes and their inhibitors, of the hemidesmosomes which affix the basal epidermal cells to the basement membrane (Daradka and Pollitt, 2004).

1.5 Lameness and Laminitis

Affecting around 20% of horses (Slater, 2014), 36.8% of the dairy population (Barker et al., 2010), and three million sheep at any one time and nine million per annum (FAWC, 2011) in the UK alone, lameness may be considered pandemic amongst ungulate species. The high incidence and lack of fully curative treatments pose a high risk to both the economy and the subject's welfare. In the dairy industry, lameness is often considered the primary welfare concern (Archer et al., 2010) as well as having estimated annual costs of around £100 per cow for the average herd (Bell, 2015) and, in the sheep farming industry, foot rot alone is thought to cost £24 million per year (Nieuwhof and Bishop, 2005). In horses, lameness is the most frequently reported ailment (Slater, 2014), with laminitis, the single most common reason for equine euthanasia (Ireland et al., 2011, Rendle, 2014), its most destructive cause.

Afflictions of the hard keratin digital integumentary appendages are not confined to the hooves of ungulates, but also affect clawed and nailed animals. While the most commonly reported claw malaises are present alongside wider spread dermatological complaints, 1.3 to 2.2% of such cases in dogs and cats exist as claw conditions alone, though these tend to be as a direct result of trauma (Miller et al., 2013). Claw deformation and abnormal curvature, changes in growth rate, lamellar separation, and sloughing of the claws (Santoro, 2012) are observable symptoms akin to those of the laminitic foot (Hunt and Wharton, 2010, Poynton, 2015). Particularly comparable to laminitis is symmetrical lupoid onychodystrophy in the dog, which involves the separation of the claw from its clawbed, the subsequent sloughing of the claw, and claw deformation upon its regrowth (Santoro, 2012). The human nail is also subject to disease causing pain and deformation, such as ingrown nail, pincer nail, and spoon-shaped nail (Rauch and Cherkaoui-Rbati, 2014).

While the affliction commonly referred to as "laminitis" has been subject to varying definitions throughout the years, today's most commonly employed, and generally best fitting, description of laminitis is the failure of the lamellar attachments between P3 and the inner hoof capsule (Pollitt, 1999). As a collection of symptoms with a plethora of known triggers and a multitude of theorised disease pathways (Heymering, 2010), rather than a definite disease of inflammatory origin as the suffix "-itis" suggests (Stevenson and Waite, 2011), a broader label, such as "lamella-associated foot lameness", would perhaps be more appropriate and less inclined to feed the many misconceptions that surround the condition. Nevertheless, for continuity with the literature, the term laminitis will be adhered to in this study hereon in.

Laminitis occurs most commonly in the two forefeet (Baxter, 2011), perhaps because they bear around 60% of the horse's weight (Rooney, 2007), though it may also strike in the two hind feet, all four feet, or just a single foot in the case of supporting limb laminitis (Baxter, 2011). The disease progression of the condition can be categorised into phases. First is the developmental phase which, being asymptomatic, can be regarded as akin to an incubation period, lasting some 24 to 60 hours (Hunt and Wharton, 2010). Following the developmental phase is the acute phase, which begins at the onset of clinically visible symptoms that may include lameness, a characteristic recumbent "laminitic stance", shifting weight between feet, an increase in hoof temperature, and an increase in the amplitude of the digital pulse (van Eps, 2010). Lasting, in general, between 24 and 72 hours, the acute phase may terminate in the resolution of the disease, or may progress to a subacute or a chronic phase (Hunt and Wharton, 2010). The subacute phase is characterised by the continuation of laminitic symptoms beyond the maximum 72 hour duration of the acute phase, but does not result in the displacement of P3 from its original location within the hoof capsule, while the chronic phase involves changes to the morphology of the lamellae along with a dislodgment of P3 (Hunt and Wharton, 2010).

1.6 The Use of X-ray Micro-Computed Tomography (μCT)

Recent technological advances are rendering the use of CT imaging as a diagnostic technique and preoperative tool increasingly common in Veterinary Medicine and, while its use in laminitis detection and management is yet to be qualified, CT for the assessment of complex foot lameness cases is in the ascent (Puchalski, 2012). These technological advances have, similarly, opened new possibilities in the field of research, which include the investigation of both hard and soft tissues, at and below the micrometre scale, in the discipline of Biology alone, providing physiological information non-destructively on the sample (Mizutani and Suzuki, 2012).

X-ray imaging is based around the principle of attenuation – the reduction of signal as the photons interact with electrons in the matter, known as the absorber, through which they are being passed (Mizutani and Suzuki, 2012). The linear attenuation coefficient (μ), defined as the proportion of incident photon intensity reduction per unit length of absorber and expressed in cm^{-1}, is dictated by photon energy (*E*) and atomic number (*Z*). Photon intensity (*I*) decreases exponentially as a function of absorber thickness (*t*) in a homogenous absorber, as shown in equation 1.1 (Kinahan et al., 2003, Rennie, 2015).

$$I = I_0 \exp(-\mu t) \tag{1.1}$$

where I_0 is the incident radiation intensity, μ=linear attenuation coefficient, *I*= photon intensity, t= absorber thickness.

Attenuation principally arises from two processes: Compton scattering and photoelectric absorption (Kinahan et al., 2003). Compton scattering involves the transfer of a proportion of the energy of the incident photon to an electron, resulting in the emission of a lower energy photon (Willmott, 2011), and photoelectric absorption is the complete transfer of the incident photon energy (Franklin et al., 2010). Compton scattering is determined principally by *Z*, with the effect of *E* being only minimal, while photoelectric absorption is strongly dependent on both (Kinahan et al., 2003). The attenuation of biological soft tissues, which display relative uniformity in their low-*Z* constituents (Mizutani and Suzuki, 2012), and bones is predominantly in the form of photoelectric absorption at low energy ranges (*E* = 30 – 50keV) and Compton scattering and at higher energy levels (*E* = 200 – 1000keV), with *E* ranging from 30 to 130keV in x-ray radiographic imaging, attenuation in CT imaging usually results from a combination of photoelectric absorption and Compton scattering (Kinahan et al., 2003). As CT detectors are not energy discriminant and solely detect *I*, greater

contrast is achieved at lower *E* levels where photoelectric absorption prevails (Kinahan et al., 2003, Mizutani and Suzuki, 2012).

The x-rays used in CT imaging may come from a laboratory x-ray generator or a synchrotron source. Synchrotron-sourced x-rays tend to be used monochromatically, with an *E* selected from a range, while laboratory-generated x-ray beams usually consist of peaks of characteristic x-rays with white beam from breaking radiation, and thus voxel (volumetric pixel) values directly represent μ in synchrotron but not in laboratory CT (Mizutani and Suzuki, 2012).

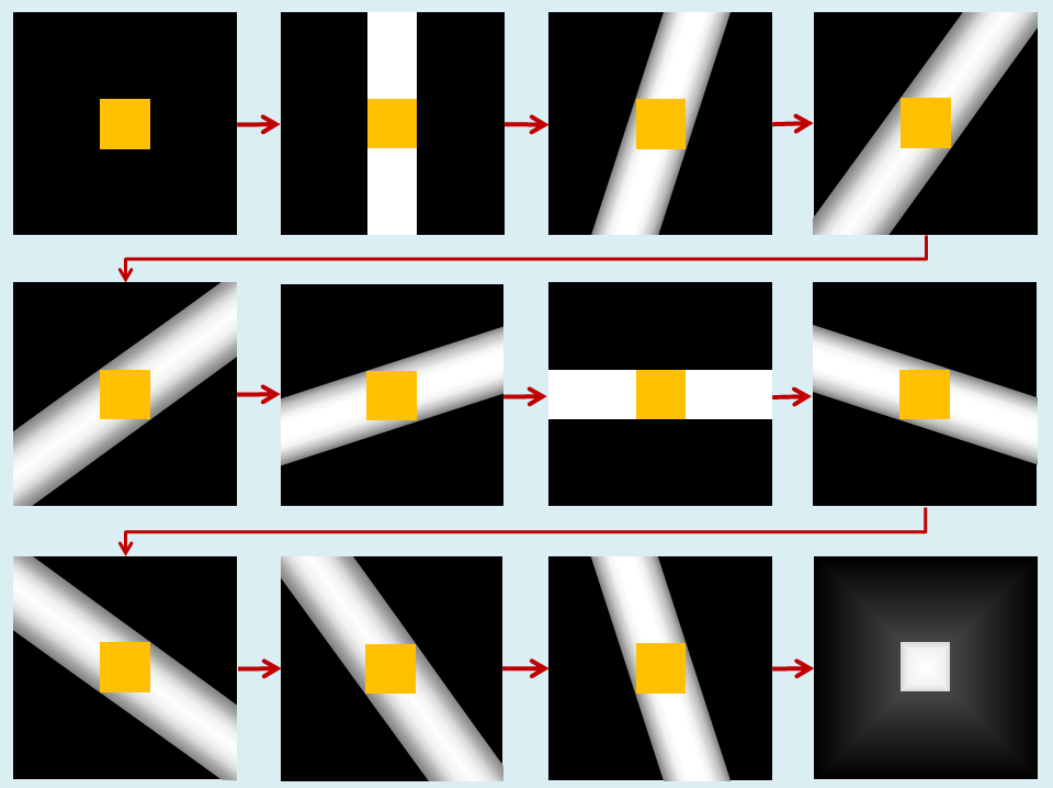


Figure 1.8: Schematic of a filtered back projection, where the addition of the transmission profile from each scanning angle gives rise to an image slice. The orange square represents the object to be scanned, and the grey-white section the transmission profile as dictated by the object's attenuating properties and the thickness to be traversed by the x-rays (note the darkening edges as the material traversed is thinner. Whiter = more attenuated). The final image in the sequence represents the reconstructed image slice which has been filtered to minimise noise from star-like artefacts borne from the superimposition of the images. Adapted from: (Willmott, 2011)

In μ-CT imaging, a sample is incrementally rotated 180^{o} around an axis perpendicular to the incident radiation beam, and the photon intensities transmitted through the absorber detected as a one-dimensional transmission

profile by the detector array are recorded as a function of rotation angle, giving rise to a sinogram (Willmott, 2011, Higgins and deRoos, 2006). Filtered back projection is the most common algorithm employed for tomographic reconstruction (Kinahan et al., 2003), giving rise to an axial image slice, or tomogram, and is best explained schematically (see Fig 1.8). Raising or lowering the sample stage, by a distance equal to the side of a component 2D pixel for the creation of isotropic voxels, allows tomograms to be generated at multiple heights throughout the sample, which can then be stacked for the reconstruction of a 3D image (Willmott, 2011).

1.7 Aims and Hypotheses

Interdisciplinarity, still a relative rarity in the sector of Veterinary Science, runs through the core of the project to which these tomographic studies belong. While all biological processes are inextricably linked to Physics and its Laws, the connection between Physics and Anatomy and laminitis is seldom acknowledged and, in the broader field of science, treating Physics and Biology as discrete entities indubitably results in vital information being missed. Combining the disciplines of Physics and Biology adds dimension, and therefore potential for the elucidation of matters which might otherwise remain obscured.

The primary hypothesis of this study and research programme as a whole is that laminitis may occur as a result of specific, and often sudden, abnormalities in hoof growth, and its resultant strain on the lamellae. The key abnormality under investigation in the various aspects of the project, which include immunohistochemical and immunofluorescent studies of the cells responsible for hoof growth and mathematical modelling of the processes involved in hoof growth, is differential growth, with a hypothesised higher growth rate in the quarter and heel regions than in the toe. As a solid, the hoof capsule's reaction to residual mechanical stresses, such as those imposed by imbalances between the growth and adhesion stresses of different regions of the foot, is likely to be long-range, and thus result in capsular deformation, including positive dorsal wall curvature. This deformation would, furthermore, give rise to a novel balance of forces on the papillae and their surrounding proliferative cells, with the potential to affect hoof growth-rate further.

A second important hypothesis underrunning the project spurns the notion that lamellar detachment is an initial, causative factor in laminitis. Instead, we propose that the observed detachment is an effect of the suggested trigger that is abnormal growth. Through the aforementioned differential growth, the capsular wall could exert a leverage effect on the lamellae, placing them under strain beyond the extent of their plasticity. Similarly, an overall growth spurt could cause the wall to move with respect to P3 faster than the hemidesmosomes are able to unbind and rebind, ending in tissue rupture.

This initial study was carried out looking at a range of equine feet in order to achieve a better understanding of the basis of hoof growth, gain insight into the anatomy of the components of the equine foot, identify correlations between hoof deformities and abnormalities in the foot's internal structures, and to work towards the development of new methodologies. The medical history and state of lameness of the animals used in this study were unknown at the point of slaughter, but the pathological state of the feet were assessed using well-known grading descriptors, such as P3 displacement and dorsal hoof wall curvature

(Floyd, 2007). A correlation between these descriptors was hypothesised, which would allow for hoof wall curvature to be utilised as a single, externally evident physical descriptor.

Laboratory μ-CT was utilised for the exploration of the bones and soft tissues of the equine foot. Cortical bone thickness and trabecular bone distortion were used as indicators of localised mechanical strain (Cornette et al., 2015). Of particular interest with regard to the project hypothesis that lamellar rupture occurs as a result of increased strain within as opposed to weakened attachments, it was hypothesised that cortical thickness of the lamellar surface and trabecular changes beneath would not indicate a diminution in the stresses exerted by the lamellae. With the challenges of achieving contrast between different soft tissue structures (Mizutani and Suzuki, 2012), the aim with regard to the soft tissues of the feet was to establish a foot preparation method that would allow their clear visualisation, demonstrating that μ-CT functions as a stand-alone research method.

The core objective of carrying out μ-CT imaging of a horse's foot at a synchrotron radiation facility was to ascertain the feasibility of undertaking future experiments requiring the high spatial and temporal resolutions, as well as the physical space for technical set-up, offered by synchrotron resources alone. The aim of this preliminary study was to obtain 3D region of interest (ROI) images of coronary dermal papillae from a whole, non-dissected horse foot at the highest possible resolution.

2 Materials and methods

2.2 Foot collection and preparation

Horse forelimbs were collected, with assistance from Dr Cyril Rauch and Ramzi Al-Agele (a PhD student on the present project), from an abattoir at Tockenham Corner, Swindon. In this study, equine histories could not be collected. Full ethical approval from the University of Nottingham was gained prior to collection. The ethical approval number attached to this study is 1215 140811.

In order to preserve the tissues and permit a good visibility of the vasculature once scanned, the limbs were perfused and fixed on-site while fresh. The aim of fixation is to maintain tissues in a life-like state, and perfusion fixation provides the optimal route for the fixative to reach the tissues upon which it can quickly act (Gage et al., 2012), while fixing the blood vessels in such a way to prevent their collapse and allow them to fill with air, providing the contrast between vessel lumen and the surrounding tissues.

Both the lateral and the medial palmar/plantar arteries were cannulated at fetlock height using 50cm dog catheters of 6 or 8Fg, depending on vessel size, attached to 50ml syringes via the means on three-way taps (Fig. 2.1). Ensuring fluid exit from both the lateral and medial veins, the foot's vascular system was flushed with 1X phosphate-buffered saline (PBS; Sigma Aldrich, UK) until the exiting fluid reached translucency, followed by 4% paraformaldehyde (PFA; Sigma Aldrich, UK) until completely clear. Tying ligature thread loosely around each vein/artery bundle in preparation, the vascular network was pressurised with the PFA and the ligature tightened and tied off during catheter removal.



Figure 2.1: Artery cannulation. Horse limb dissected to allow the cannulation of artery at the fetlock for perfusion with phosphate-buffered saline and paraformaldehyde.

On arrival at the School of Veterinary Medicine and Science, Sutton Bonington, after transportation through approved means, the limbs were refrigerated for 24 hours prior to the final steps of preparation. Preparations for CT scanning involved: cleaning of the external hoof capsule with a hoof-pick and paper towels; numbering the feet for later identification; removal of shoes, where applicable, with a hammer, hoof buffer and a shoe puller; the trimming of excess hair from any particularly heavily feathered limbs with Wahl Artiko horse clippers; and, finally, disarticulation between the first and second phalanges (P1 and P2). The prepared feet were stored at -20^{o}C until required for scanning.

2.3 CT scanning

2.3.1 Laboratory Micro-Tomography

. Prior to the scanning of the samples, the machine was calibrated and the technique optimised to ensure optimum resolution and contrast, through adjustments in sample distance from x-ray gun for the former, and photon energy (voltage) and flux (current) for the latter. Due to the complex technical knowledge required, Dr Craig Sturrock (co-director and manager of the Hounsfield Facility) and Brian Atkinson (research technician at the Hounsfield Facility) carried out all processes involving the use of the CT scanner, however sample preparation and all image and data analysis was carried out by the author.

2.3.1.1 Whole-Foot Scanning

The micro CT scanner used was a GE phoenix v|tome|xm (General Electric, Germany, 2013). Around 24 hours prior to the start of scanning, the feet were removed from the freezer and each foot packaged into a plastic food-type storage box , taking care to note the foot's individual identification number on the exterior of the box, within which polyethylene packing foam was used immobilise the foot. The packaged samples were stored in the refrigerator for approximately six hours, allowing the initial thaw-related shrinkage to be compensated for with additional packing foam, prior to being transferred to the on-site tomography suite in the School of Bioscience's Hounsfield Facility, where the thaw was completed at ambient temperature.

For whole-foot scans, a resolution of 120µm (voxel size) was achieved, a voltage of 125keV selected and, through calibration ensuring that the outputted grey values of the most (bone) and least (air) dense substances utilised the full available spectrum, a current of 320µA set. Each foot was scanned and the data stored on the facility's system prior to manual processing.

2.3.1.2 Scanning Sections for Microstructures

The scanner employed for the higher resolution scans of the cut sections was a GE phoenix Nanotom S. A foot was selected from those fully scanned based on the best visibility of the blood vessels in the resulting images. On removal from the freezer, two cuboidal sections of 15*20*60mm were cut, with the aid of a Dremel tool with grinding wheel attachment and a scalpel, from the dorsal and medial/lateral areas of the foot. Sections included the proximal area of the hoof capsule and the full epidermal/dermal lamellar region below, and the coronary corium, extending approximately 10mm above the commencement of the capsule. The sections were each placed in 50ml centrifuge tubes and secured

with tightly packed packing foam. As above, the samples were permitted to thaw overnight prior to being scanned, with a final resolution of 18µm.

2.3.2 Synchrotron Micro-Tomography

The scan took place in experimental hutch 1 on beamline I12, at Diamond Light Source, Harwell Science & Innovation Campus, Didcot, Oxfordshire. The equine foot, prepared following the method described in Section 2.1, was removed from the freezer at Nottingham Vet School the previous day and transported to Diamond Light Source, where it was stored in a cool atmosphere overnight until the start of the experiment.

This was the first time that a horse hoof had ever been scanned using this equipment, therefore the optics and detection equipment were set up and calibrated by beamline staff. The former involved adjusting the photon energy (to an eventual optimum of 90keV) and flux through regulation of the Laue monochromator, and further flux alteration with the aid of attenuators. The latter was based on camera and module choice (where module 2 was selected, giving a pixel resolution of 8µm) as well as the computerised calibration of the scintillator pixels.

As region of interest (ROI) scans were to be performed on an integral foot, small cellulose spheres were attached, with the aid of superglue, to the external proportions of the ROIs to facilitate their correct localisation. The foot was then firmly secured to a height-adjustable metal support utilising small metal clamps. Due to the high attenuating properties of metal, care was taken to ensure that these clamps did not cover any areas of the foot to be scanned, shielding them from the beam. The metal support was then bolted to sample stage, the position of which was adjusted, using a laser as a guide, to favour the optimum axis of rotation around the ROI.

After test scans and further adjustments to the various experimental components had been made, the scanning process commenced. Scans were taken of the dorsal aspect of the foot, focussing on the soft tissues, including the coronary corium, dermal papillae, and dermal lamellae. This was achieved by scanning at eight different heights along the dorsal wall. The resulting images were later ‘stitched’ together to gain an overview of the area. For each of the eight areas, 10 full scans were performed for subsequent averaging in order to aid noise reduction.

2.4 CT image processing

2.4.1 Hoof Orientation and Planar Adjustments

The initial format in which the output volumetric image data from the laboratory CT scanner were saved required the use of Volume Graphics (Heidelberg, Germany) software. Prior to resaving the data in a format utilisable with other imaging software, Volume Graphics was used to make planar adjustments to the 3D images.

Due to the nature of the boxes and packing material, it was not possible to ensure that the feet were lying perfectly straight and level within. Making use of Volume Graphics' "transform" feature, this was computationally made good by visual assessment of XY (axial), XZ (coronal) and YZ (sagittal) planar sections (Fig. 2.2), and their reorientation through rotational adjustments around the Z, Y and X axes respectively.

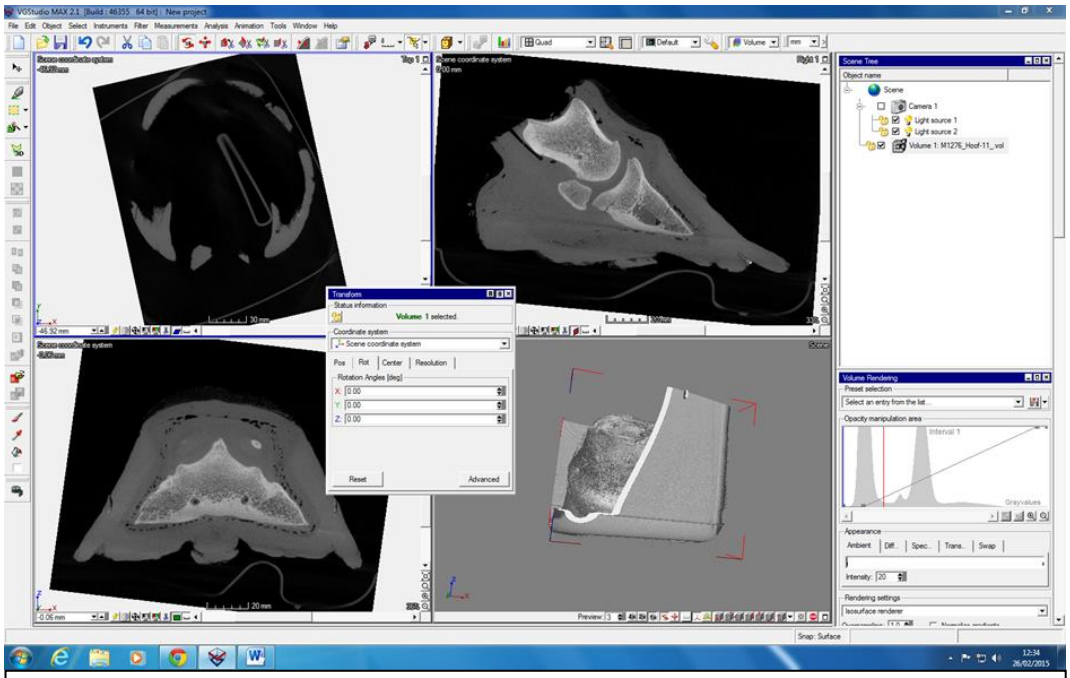


Figure 2.2: Planar adjustments with Volume Graphics, showing a section from the XY (axial) plane in the top left of the image quadrant, the YZ (sagittal) plane in the top right, and the XZ (coronal) plane in the bottom left.

The resultant data were then "sliced" and exported as TIFF image stacks.

2.4.2 Bone Segregation

The segregation of the bone from surrounding materials on the CT images was carried out using the surface determination function on Volume Graphics, by selecting an area of the hoof capsule as the background material, and an area at

the base of the extensor process of P3 as the foreground material. Setting the tolerance level to 30,000, the maximum radius to zero, the mode to static, and the command to 'stay in ROI' (taking interconnecting voxels only, and thus removing noise borne from low contrast) in the region growing function, a ROI was created from the thresholded bone. Each bone (P2, P3 and navicular) was exported, both individually and as a TIFF image sequence collection. Image sequences were imported to Fiji (Max Planck Institute of Molecular Cell Biology and Genetics, Germany (Schindelin et al., 2012)) and binarised using the in-built 'default' thresholding algorithm. The resultant binary image stacks were utilised for 3D reconstruction and analysis.

2.4.3 Vasculature Isolation

The isolation of the vasculature was carried out using the processes of thresholding and binarisation on Fiji. Unlike the bone, the contrast between the vasculature and the surrounding materials was great enough – due to the contrast afforded by the low attenuating properties of the air which filled fixed vessels – to achieve reliable results with a Fiji autothreshold function.



Figure 2.3: Isolation of vasculature. Creating binary image with appropriate threshold and multiplying by its mask permits removal of background.

The image stack was converted into binary data, using the IsoData autothreshold, and duplicated. The duplicate stack was converted to a mask by inverting the colours, and the holes corresponding to the blood vessels were blanked out by a combination of hole filling, outlier removal, and stack erosion. The first image stack was then multiplied by the second (Fig. 2.3) using the image calculator, giving rise to the isolated blood vessels. Through binary logic, if $\text{white} = 1$ and $\text{black} = 0$: $\text{black}(0) \cdot \text{black}(0) = \text{black}(0)$; $\text{white}(1) \cdot \text{black}(0) = \text{black}(0)$; and $\text{white}(1) \cdot \text{white}(1) = \text{white}(1)$.

The processes involved with the isolation of the vasculature were able to be done automatically with the creation of a macro. The macro was written using a combination of the Macro Recorder and Macro Editor plugins in Fiji.

2.4.4 Microstructures

The contrast between the dermal and epidermal tissues is, in general, relatively low. The dermal structures – lamellae and papillae – were, however, made visible due to their profuse vascularisation which, due to its paraformaldehyde

fixation, was filled with air. The minute, tightly packed vessels were small yet abundant enough to create sufficient contrastable volume to be detected by the scanner.

2.4.4.1 From Laboratory CT images

As the vasculature was the target tissue visible in the microstructures, the method of isolation was identical to that described in Section 2.3.3.

2.4.4.2 From Synchrotron CT images

The initial processes rendering the raw files gathered through synchrotron CT imaging utilisable included grey value averaging of the 10 replicate scans, phase contrasting, and formatting as 8-bit TIFF image stacks. These preparatory processes were carried out by Robert Atwood at Diamond Light Source.

The image stacks, saved on the XY (axial) plane, were opened in ImageJ with the exclusion of those at either extremity that lacked clarity. This was permitted by a good overlap between adjacent scans (Fig. 2.4).

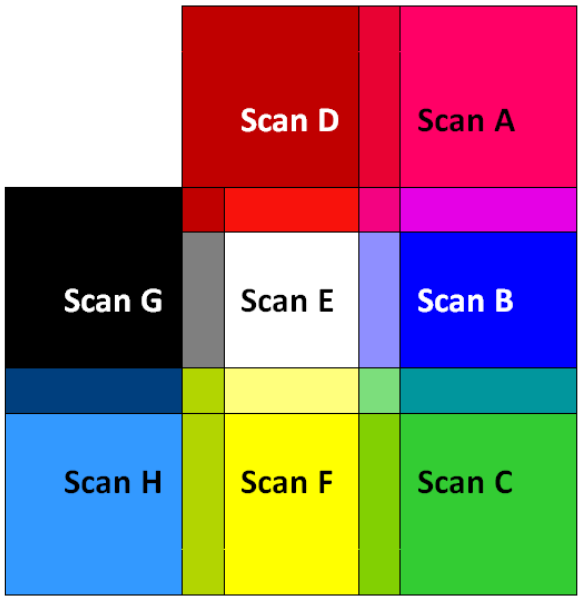


Figure 2.4: Scan stitching. Schematic of the layout of the eight stitched scans, demonstrating their overlap.

Using the rectangle selection tool, a rectangle expanding the entire x-axis in length and the central 250 pixels in width was selected, and the 'entire stack' option of the 'duplicate' function utilised to select the cuboid with the entire z-axis for its depth. The cuboid was then orthogonally resliced to give a YZ (sagittal) view. Using the Pairwise Stitching plugin (Preibisch et al., 2009), the image stacks were stitched in the following fashion with reference to Fig. 2.4: Scan A to Scan B, then Scan A+B to Scan C; and Scan D to Scan E, then Scan D+E

to Scan F. Scans G and H were superfluous, lying outside of the field of interest, and were thus not used. Shadowing towards the left edge of the stacks caused the stitching attempt of Scan A+B+C with Scan D+E+F to fail. This was rectified by applying a Gaussian blur with a sigma (radius) of 100 to each stack, then subtracting the original from its Gaussian-filtered duplicate using the image calculator. The resulting image stacks were then successfully stitched.

A slight shift in slice position rendered a few images at the stitched stack's two extremities (z-axis) incomplete. The slices in question were therefore removed, reducing the image depth (slices) to 243 voxels.

The image stack was next made binary with the use of the IsoData automatic threshold. Making use of the 3D viewer plugin to locate specific details, the image stack was cropped, outliers with a radius of one voxel were removed, and the polygon selection and paintbrush tools employed for the manual removal of noise.

2.5 Physical Descriptors

For each hoof a variety of physical measurements were obtained from the CT images including the curvature (Section 2.4.1) and angles (Section 2.4.2). This was achieved by retrieving the coordinates from a series of points placed along the dorsal hoof wall of the central sagittal section of each hoof. Each image was imported to Fiji where: it was rotated (by 90^{o} or 180^{o} only, as planar adjustments had been made previously) and/or flipped, where needed, to ensure that the distal point was orientated towards the bottom left; cropped to the distal point on the left and to the edge of the weight-bearing horn at the bottom (i.e. so that the distal point found itself in the coordinate origin), and to the top of the coronet on the right; the scale was set; 20 equidistant vertical lines were drawn using a grid overlay macro (Rasband, 2003); and points were placed where the lines intersected the dorsal wall, and the Cartesian coordinates of these points measured.

2.5.1 Dorsal Curvature

For each foot, the two-dimensional curvature, C, at each measured point of the dorsal aspect of the hoof wall surface was calculated using Microsoft Excel's polynomial curve fitting function, and a modified version of the differential calculus equation (eq. 2.1).

$$C = \frac{y''}{\left(1 + y'^{2}\right)^{3/2}} \tag{2.1}$$

where y' and y'' are the primary and secondary derivatives of y respectively.

To avoid computational problems associated with the multiplication of very large by very small numbers, x and y were rescaled and the subsequent equation amended. The new variables $\hat{x}$ and $\hat{y}$ were defined (eq. 2.2 and 2.3)

$$\hat{x} = x/[x] \tag{2.2}$$
$$\hat{y} = y/[y] \tag{2.3}$$

where [x] and [y] are the means of x and y respectively. $\hat{y}(\hat{x})$ was plotted and a polynomial curve to the order of 3 was fitted, generating a $\hat{y} = f(\hat{x})$ equation. The primary (eq. 2.4) and secondary (eq. 2.5) derivatives of $\hat{y}$ were then calculated.

$$\hat{y}' = n\hat{x}^{n-1} \tag{2.4}$$
$$\hat{y}'' = (n-1)n\hat{x}^{n-2} \tag{2.5}$$

where each formula is applied to each term within the polynomial equation and where n denotes the power. Following the chain rule, curvature at each point was calculated by the amended equation 2.6.

$$C = \frac{[y] \cdot \frac{\hat{y}''}{[x]^2}}{\left(1 + \left([y] \cdot \frac{\hat{y}'}{[x]}\right)^2\right)^{3/2}} \tag{2.6}$$

Due to the particular limitations of the collection methods, the data points were not spaced fully equidistantly along the *x*-axis. To take this into account, the integral $\int C\, d\hat{x}$ was calculated and used in the final calculation of average curvature (eq. 2.7). This was done in an approximate fashion, supposing on a hypothetical $C(x)$ curve and treating the sections cornered by two equivalent pairs of x and C values as trapezia and calculating the sum of their areas.

$$\int C\, d\hat{x} = \sum_{i=1}^{20} \frac{(C_i + C_{i+1})(\hat{x}_{i+1} - \hat{x}_i)}{2} \tag{2.7}$$

Average curvature, $\langle C \rangle$, was then calculated (2.8).

$$\langle C \rangle = \frac{\int C\, d\hat{x}}{\hat{x}_L - \hat{x}_R} = \frac{\int C\, dx}{x_L - x_R} \tag{2.8}$$

where $\hat{x}_L$ is the smallest $\hat{x}$ value and $\hat{x}_R$ is the largest.

2.5.2 Dorsal Angle

With the aim of deducing the cosine of angle α (Fig. 2.5) as a physical descriptor of the hoof's pathophysiological state, the tangent of the angle of the hoof at the distal point of the dorsal wall, θx_L, was first calculated (eq. 2.9).

$$\tan(\theta x_L) = \frac{y_2 - y_1}{x_2 - x_1} \tag{2.9}$$

where y_1 and y_2, and x_1 and x_2 are the first (smallest) and second y and x coordinates respectively.

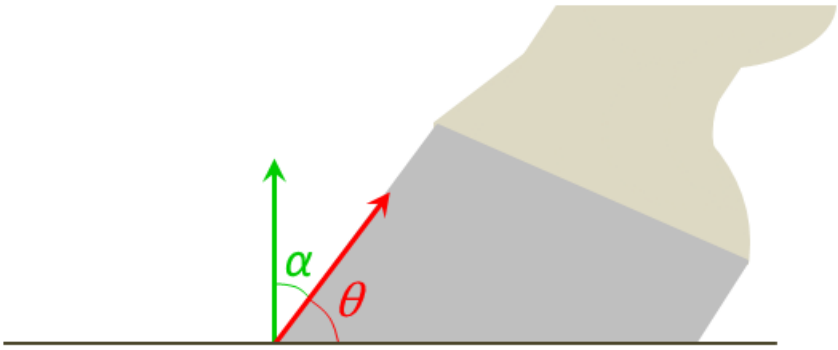


Figure 2.5: Hoof dorsal angles, with θ being the angle between the dorsal surface and the ground, and α being the angle between the dorsal surface and the axis perpendicular to the ground.

The cosine of angle α was then calculated with equation 2.10.

$$\cos\alpha = \frac{1}{\sqrt{1 + \frac{1}{((\tan(\theta x_L))^2}}} \tag{2.10}$$

2.5.3 Curvature and Angle Relationship

The strength of the relationship between curvature and angle was examined taking the centre of curvature into account. To this end, the curved dorsal wall was treated as an arc (Fig. 2.6A and B) and, using the coordinates of the two extremities of the arc, the coordinates of the centre of curvature were calculated. This was carried out on 14 concave hooves with positively curved profiles, and nine hooves with negatively curved profiles.

The first stage in the process of determining the centre of curvature was to calculate the radius, R, of the arc's corresponding segment (eq. 2.11).

$$R = \frac{1}{\langle C \rangle} \tag{2.11}$$

In the aim of calculating the x-axis coordinate value, x_0, of the centre of curvature, equation 2.12 was generated for hooves with positive curvature, and equation 2.13 for those with negative curvature. The workings out that led to this equation can be found in the appendix.

$$\sqrt{R^2 - (x_B - x_0)^2} - \sqrt{R^2 - (x_A - x_0)^2} - (y_A - y_B) = 0 \tag{2.12}$$

$$-\sqrt{R^2 - (x_B - x_0)^2} + \sqrt{R^2 - (x_A - x_0)^2} - (y_A - y_B) = 0 \tag{2.13}$$

where x_A and y_A are the coordinate pair of the point on the arc corresponding to the distal tip of the hoof, and x_B and y_B are the coordinate pair of the point on the arc corresponding to the proximal point of the hoof.

As x_0 remained unknown, a series of hypothetical values, ascending in increments of 10, was generated through trial and error – though generally ranging from a few negative hundred to a few positive hundred. For each hypothetical x_0 value, equation 2.12 or 2.13 was employed depending on curvature. A curve was then produced, plotting the hypothetical x_0 values as a function of the results of the equation. Seeking to pinpoint the value of x_0 when the equation equalled zero, the graph was used to determine this value from the x coordinate value at the curve's intersection with the x axis (Fig. 2.6C and D).

The difference between x_A and x_0 was used to normalise the calculation of the relationship of curvature to $\cos\alpha$ (normalisation process shown in. 2.14) so as to take other variables, such as hoof height, into account.

$$\frac{(x_0 - x_A) \cdot \langle C \rangle}{\cos\alpha} \tag{2.14}$$

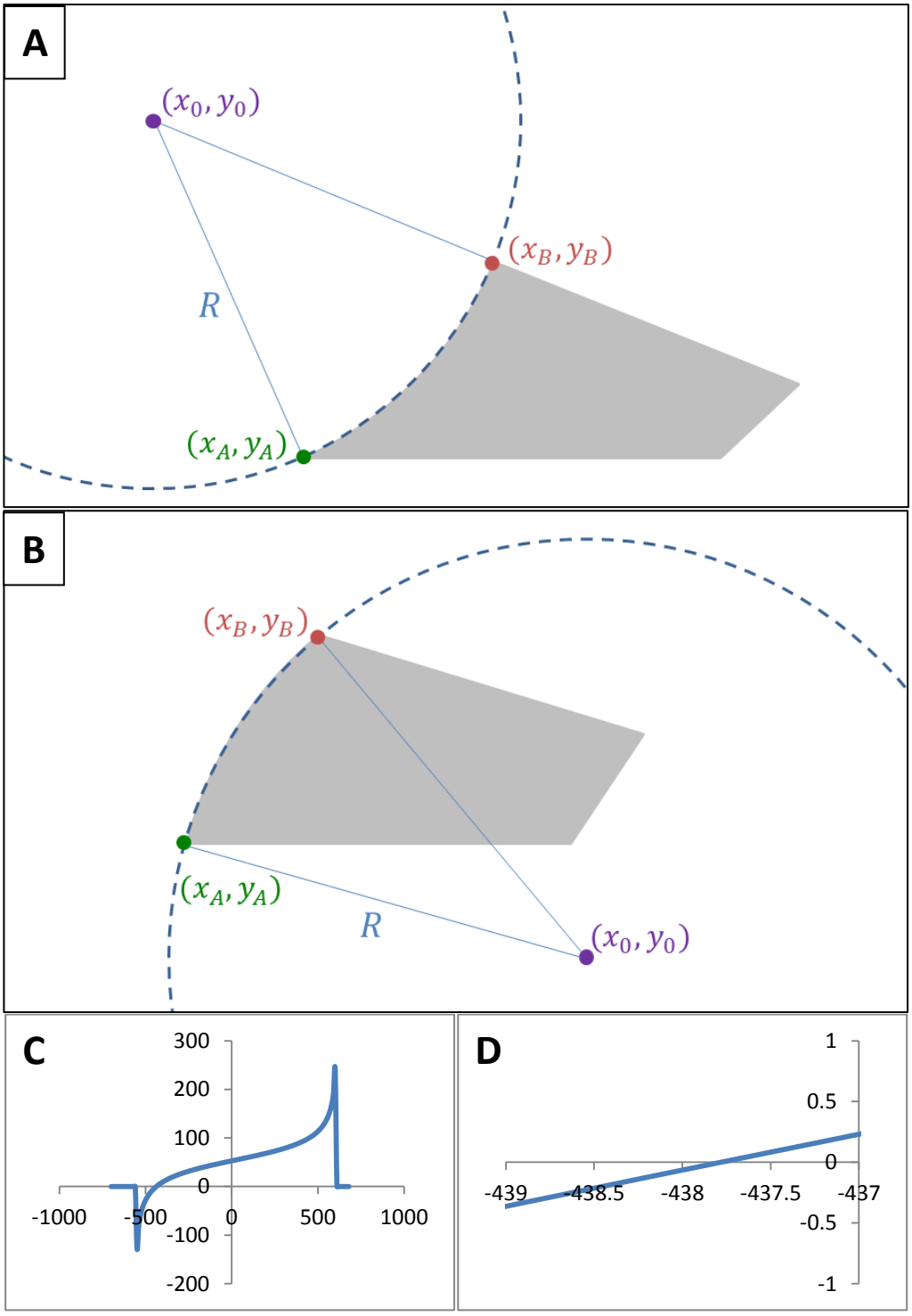


Figure 2.6: The centre of curvature of the dorsal hoof wall. (**A**) illustrates a positively curved hoof, and (**B**) a negatively curved hoof. On both images, R denotes the radius of the segment, x_A and y_A the coordinates of the distal point of the toe, x_B and y_B the coordinates of the proximal point of the hoof, and x_0 and y_0 the coordinates of the centre of curvature. (**C**) shows the variable x_0 values as a function of the results of equation 2.12/2.13, and (**D**) shows this same curve zoomed in, on which the value of x where $y = 0$ is the true value of x_0

2.5.4 Displacement of the Third Phalanx

The displacement of P3 was assessed in terms of its rotation and of its sinking from its normal axis and position. Both of these factors were calculated on 26 equine feet.

Rotation was measured as the angle at the intersection of the lines parallel to the dorsal aspects of the hoof wall and P3 (Fig. 2.7). This was carried out by fitting linear trendlines to the coordinates taken from the dorsal aspects of the hoof wall and P3 (see section 2.5.2).

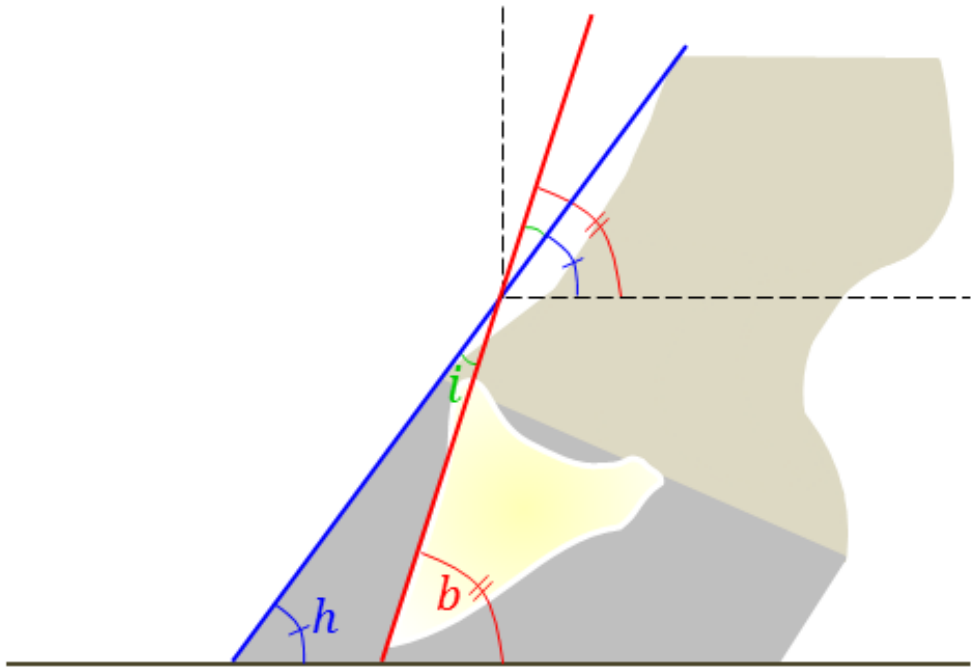


Figure 2.7: Angle of rotation. This schematic representation of a rotated third phalanx in a laminitic foot shows the angle of the dorsal hoof wall, h, the angle of the dorsal aspect of the third phalangeal bone, b, and the intersect of the extensions of the two, i, as well as their corresponding angles in the inset box.

Taking the prefactors of x of the trendlines' equations as the tangents of the angles h and b, described below, equation 2.15 was borne.

$$\tan(i) = \tan(b) - \tan(h) \tag{2.15}$$

where h is the angle between the dorsal aspect of the hoof wall and the ground, b is the angle between the dorsal aspect of P3 and the ground, and i is the angle of the intercept of the dorsal aspects of the hoof wall and P3.

The angle i was then calculated in degrees with equation 2.16.

$$i = \frac{\tan(i)}{\pi} \cdot 180 \tag{2.16}$$

Sinking of P3 was determined by measuring the vertical depth of the summit of the extensor process from the coronet. This was taken by direct measurement, using the rectangle selection tool on Fiji, of the vertical between the ground and the coronet and the apex of the extensor process (Fig. 2.8) on the scaled central sagittal image slice for each foot. The difference between the two was then calculated (eq. 2.17).

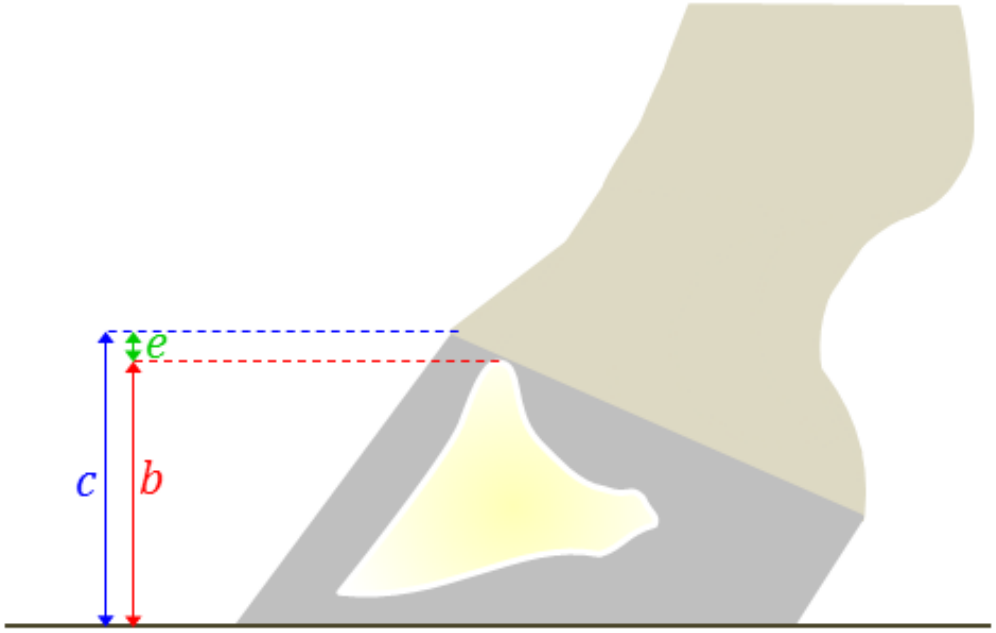


Figure 2.8: Extensor Process Depth. This diagram shows the measurements taken for the calculation of depth of the extensor process of the third phalanx. These are: the vertical distance from the dorsal coronet to the ground, c; the vertical distance from the summit of the extensor process of the third phalangeal bone to the ground, b; and the vertical distance between the two, e.

$$e = c - b \tag{2.17}$$

where c is the vertical distance between the coronet and the ground; b is the vertical distance between the top of the third phalangeal bone's extensor process; and e is vertical distance between the coronet and the apex of the extensor process.

To take variations in overall foot size into account, the extensor process depth was scaled using equation 2.18.

$$\hat{e} = \frac{e}{c} \tag{2.18}$$

where $\hat{e}$ is the scaled, relative extensor process depth.

2.6 Bone Analysis

As the principal bone of the foot – and that which is bound to the hoof capsule through the intermediary of the lamellae – the third phalanx (P3) was the subject of investigation. As indicators of its pathophysiological state, the curvature of its dorsal surface (2.5.1), the relative thickness of its cortical bone (2.5.2), and the degree of anisotropy of its trabecular bone (2.5.3) were measured.

2.6.1 Bone Curvature

In much the same manner to the measurements made for the physical descriptors in Section 2.5, the central sagittal sections of 27 hooves were imported to Fiji, where each image was flipped/rotated where necessary, the scale was set, the image cropped down to the tip of P3 on the bottom left and to the base of the extensor process on the right, the grid overlay macro employed, and the points where line intersected bone measured. On importation of the thus generated coordinates to Excel, average curvature was calculated following the method in Section 2.4.1.

2.6.2 Cortical Bone Thickness

The binary bone image sequences of the third phalanges of 20 equine feet were imported into Fiji, and the scale was set. Using the polygon selection tool and the ROI manager function, the cortical regions of the bone were "dissected" into anatomical ROIs. These included the upper and lower toe and quarter walls, the toe and quarter solar margins, the toe and quarter solar surface, the articular surfaces abutting the second phalanx and the navicular bone, the collateral ligament attachments, the flexor surface, and the extensor process. The toe and quarter regions were taken as the inner and outer thirds of the bone, from a dorsal aspect, respectively, and the upper and lower sections as the proximal and distal halves.

The thickness function of the BoneJ plugin (Doube et al., 2010) was used to calculate the average 3D thickness of each ROI. So as to account for any differences in general foot size and scan setup (which could have an effect on grey value contrasts and thus thresholding), the comparison between the cortical bone thicknesses of different feet was carried out, with the aid of Excel, using ROI thickness ratios.

2.6.3 Trabecular Bone Distortion

For 25 equine feet, the image sequence of the whole greyscale foot was imported in Fiji, and the scale set to pixels. Focussing on the central sagittal section, the image stack was rotated so as to align the dorsal surface of P3 vertically. Using the rectangular selection tool, the trabecular bone was selected

from below the extensor process down to the inner apex of P3 (Fig. 2.9). This was measured then drawn on as an overlay. The height of the rectangle was divided by 10 and, still using the rectangular selection tool, these divisions were added to the overlay. In the second from the distal-most section, the rectangular selection tool again being used, a square extending the height of the section covering the trabecular region of the bone at the exclusion of the cortex was traced. Using the duplicate function, setting the slice selection to render the depth equal to the square's height and width, a cube was selected, keeping the central sagittal section of the hoof as the centre section of the cube. The default autothreshold was used to render the cube binary.



Figure 2.9: Trabecular bone selection. Selection of a cube of trabecular bone from the distal point of the third phalanx.

To the binary cube of trabecular bone, BoneJ plugin's Anisotropy function was applied, giving rise to mean intercept length (MIL) and degree of anisotropy

(DA). The plugin functions by virtually inserting a large number of longitudinally equal vectors, with a random point of origin, into the sample. The boundary between the white of the bone and the black of the background periodically intercepts these vectors, which is counted as a boundary hit. The vector length and number of boundary hits are then utilised by the programme to calculate the MIL (eq. 2.19) and DA (eq. 2.20).

$$MIL = \frac{\vec{L}}{n_{BH}} \tag{2.19}$$

where $\vec{L}$ is the vector length and n_{BH} is the number of boundary hits.

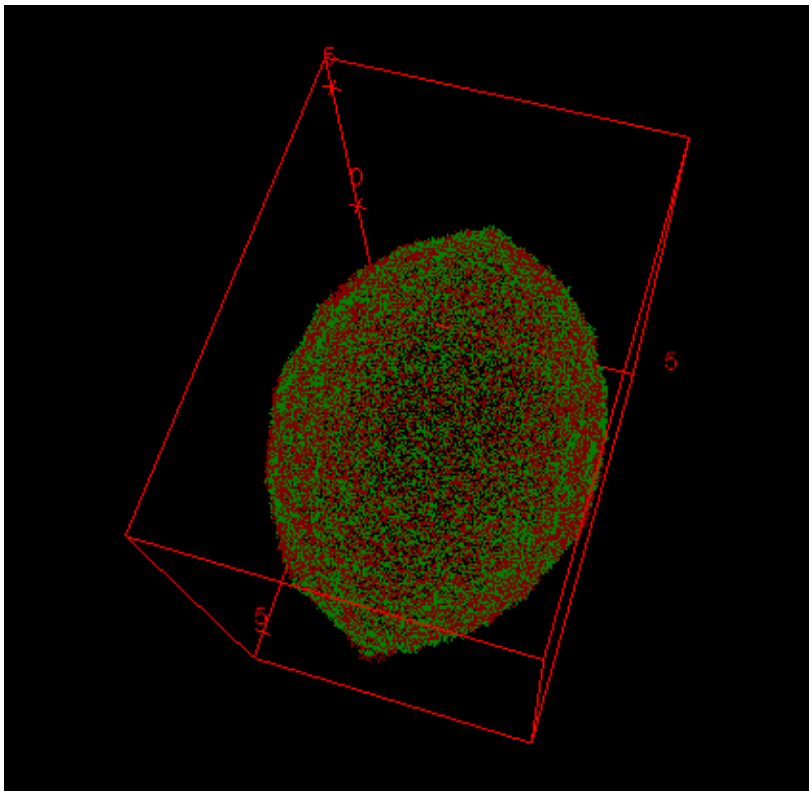


Figure 2.10: Mean intercept length vector cloud. This 3D graphic result from the BoneJ plugin's anisotropy function permits the illustration of the principal axes of anisotropy.

As an automated function of the plugin, multiplying each vector by its MIL allows the creation of a point cloud (Fig. 2.10) which illustrates, through the visualisation of the axes of its ellipsoidal shape, both the degree and the predominant direction of anisotropy. Eigenvalues, which represent the lengths of the ellipsoid's axes, and eigenvectors, which represent their orientation, also

result from the application of the plugin. Two of the three eigenvalues are then used in the programme's calculation of the DA (Eq. 2.20).

$$DA = 1 - D_1/D_3 \tag{2.20}$$

where D_1 is the lowest eigenvalue, with the shortest distance between boundary hits, and D_3 is the highest.

2.7 Vasculature Analysis

To investigate changes in the vasculature of horse feet displaying laminitic-like characteristics, the lumen diameter of the blood vessels in the sublamellar plexus of the toe was compared to that of the blood vessels in the toe's solar plexus of 15 equine feet. The binary images, as described in section 2.3.3, were three-dimensionally cropped to isolate the toe region using the rectangle selection tool on the central sagittal image. Using the polygon selection tool and the ROI manager, the sublamellar and solar plexuses were isolated. The BoneJ plugin's thickness function was employed to both image stacks, and the resulting thickness value of the sublamellar plexus divided by that of the solar plexus to find the ratio.

2.8 Microstructure Analysis

From the final, binary image stack processed from the synchrotron-sourced μ-CT images, as described in section 2.3.4.2, the dermal papillae of the *stratum externum*, *stratum medium*, and *stratum internum* were isolated using the polygon selection tool. The BoneJ plugin's thickness function (Doube et al., 2010) was used to calculate the mean diameter (D) of the papillae of each *stratum*, along with their standard deviation. 10 papillae from each *stratum* were then selected at random and, with the help of the segmented line tool, their lengths (h) measured. From this, the mean length and its standard deviation were calculated using Microsoft Excel. Finally, treating the papilla as cylindrical, the papillae's surface areas (A) were approximated using the standard formula for the area of a cylinder, modified to account for the fact that the proximal extremities of the papillae are internal to the dermis and do not border the epidermis (eq. 2.21).

$$A = 2\pi\frac{D}{2}h + \pi\left(\frac{D}{2}\right)^2 \tag{2.21}$$

2.9 Immunohistochemistry

As a concomitant study within the umbrella of the larger project, immunohistochemistry was carried out by PhD student Ramzi Al-Agele. While it does not directly pertain to the µ-CT investigations discussed here, a pooling of the immunohistochemistry and the µ-CT data, which were obtained from the same equine feet, was necessary and will thus be briefly touched upon.

From the feet collected as described in section 2.1, cuboidal sections were cut from the coronary areas of the toe and the medial and lateral quarters and heels of seven feet with flat toe wall profiles ($\langle C \rangle < 0.001 mm^{-1}$ and $\langle C \rangle > -0.001 mm^{-1}$) and five displaying positive curvature ($\langle C \rangle > 0.001 mm^{-1}$), ensuring the integrity and inclusion of the coronary corium and the epidermal and dermal tissues extending around two centimetres down the hoof wall, and stored in tubes of 4% PFA overnight. The tissue blocks were then embedded in paraffin wax and sliced longitudinally to a thickness of 8µM before being affixed to microscope slides and de-waxed. Each sample was next treated with an antibody targeting cellular proliferation markers P63 (Anti p63 antibody, rabbit polyclonal [N2C1] Gene Text, USA), and stained with Leica polymer detection kits (Leica, Germany) to differentiate between antigen-positive and -negative cells. Concentrating on the epidermis' *stratum basale* around the papillae, the number of positive and negative cells was counted and the proliferative index (PI) calculated. The full protocol provided by Ramzi Al-Agele is shown in Appendix III.

2.10 Anatomical Image Rendering

Utilising a variety of thresholding algorithms depending on the tissue-type in question (see Section 2.3 on CT image processing for information on the thresholding of specific structures), binary image stacks were produced. In these images stacks, the structures of interest were represented in white and had a grey-level value of 255, whilst their surroundings were coloured black and had a grey-level value of zero. The thus volumetrically rendered images were then viewable using the 3D viewer plugin.

Certain images required the conversion from binary 8-bit greyscale to RGB colour. This included, for instance, the superimposition of the vasculature, in red, and the bone. For this, two identical initial greyscale stacks to include the entire vasculature were opened. One was thresholded for the isolation of the bone, and the other for the vasculature, and the output binary images were converted to RGB. The bone was left white (the red, green and blue channels each set at 255), but the vasculature was coloured red (the red channel set to 255 and the green and blue channels set to zero. The two image stacks were then added using the image calculator.

2.11 Statistical Analysis

Where appropriate, linear regression analyses were carried out using GraphPad Prism (GraphPad, California). The threshold for statistical significance was set at 5% ($P<0.05$).

3 Results

3.2 Physical Descriptors

3.2.1 Dorsal Wall Curvature and Angle

As two externally observable characteristics of the chronically laminitic hoof, dorsal wall curvature and angle (Hunt and Wharton, 2010) were compared by calculating the ratio of one to the other, normalising the curvature by account taking of the centre of curvature. The mean ratios for positively (concave) and negatively curved (convex) hooves are presented in Fig 3.1, with error bars showing the standard deviation (SD).

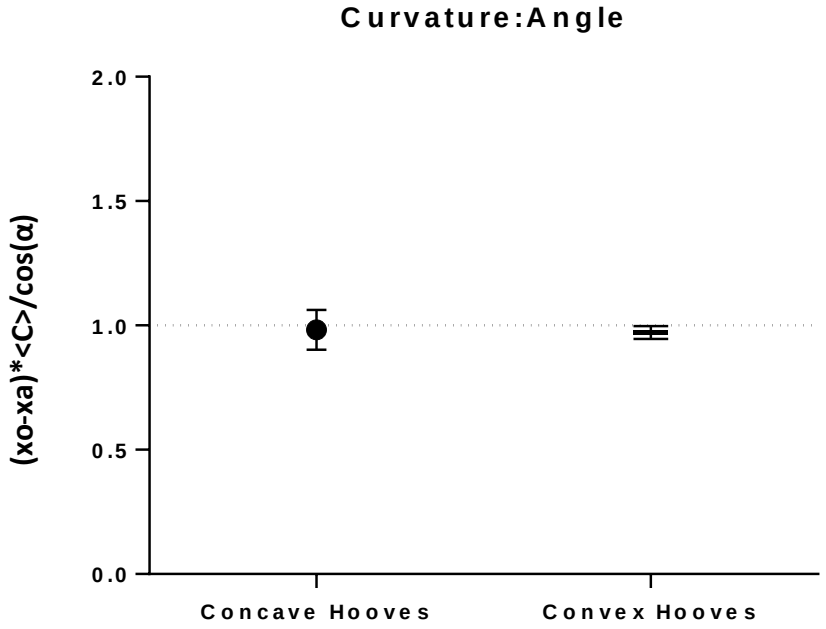


Figure 3.1: Relationship between curvature and angle. Mean value of $\frac{(x_0 - x_A)\cdot\langle C\rangle}{\cos\alpha}$ for positively curved (concave) and negatively curved (convex) hooves with error bars showing standard deviation. Concave hooves n=14, and convex hooves *n*=9.

The ratio of the normalised mean curvature to the angle was 0.982 (SD=0.079) in the case of positively curved hooves, and 0.972224 (SD=0.026) in the case of negatively curved hooves. Both of these values are close to one, indicating a good correlation between dorsal wall curvature and angle. The derived coefficient of variation (CV) of each serves to further back this up, being inferior to one in both instances: CV of concave hooves = 0.08, and CV of convex hooves = 0.026.

3.2.2 Displacement of the Third Phalanx

The displacement of P3 was investigated in terms of rotation and sinking, using measurements of angle between the dorsal surfaces of P3 and the hoof wall and the depth of the summit of the extensor process from the coronet in relation to the hoof's height respectively. The angle of rotation and relative extensor depth are presented as functions of hoof wall curvature in Figure 3.2A, and in relation to each other in Figure 3.2B, and the normalisation of the relative extensor process depth in Figure 3.2C. Their respective linear regression analyses are displayed in Table 3.1.

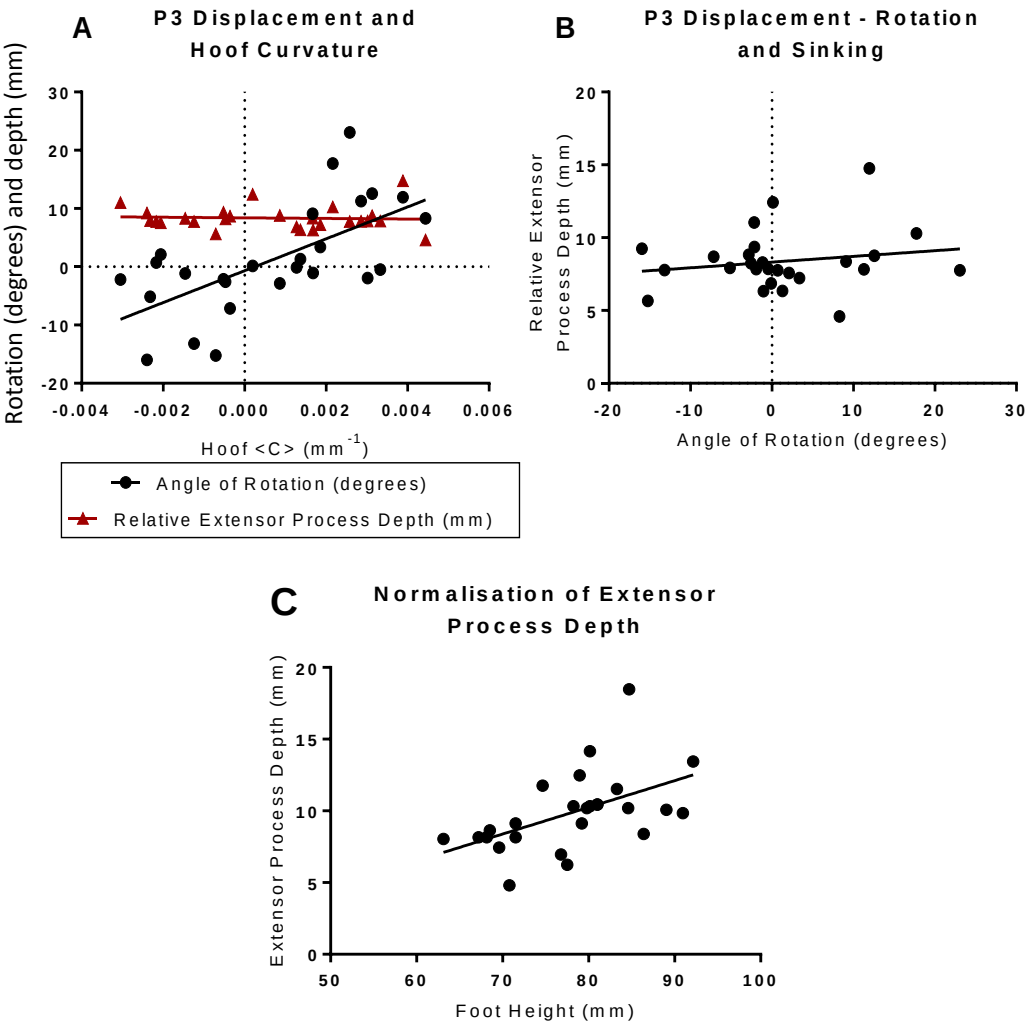


Figure 3.2: Displacement of the third phalanx. (**A**) shows the displacement of the third phalanx in terms of angle of rotation and relative extensor depth as functions of average hoof capsule curvature. (**B**) shows the relative extensor process depth as a function of the angle of rotation. (**C**) shows the pre-normalised extensor process depth as a function of foot height. The linear regression model for each plot can be found in Table 3.1. *n*=26

	Goodness of Fit (R^2)	Deviation From Zero (P)
A - Angle of Rotation f Hoof Curvature	0.413	0.0004
A - Relative Extensor Process Depth f Hoof Curvature	0.003	0.789
B - Relative Extensor Process Depth f Angle of Rotation	0.031	0.387
C - Pre-Normalised Extensor Process Depth f Foot Height	0.265	0.007

Table 3.1: Linear regression models for displacement of the third phalanx. For each plot of the graphs in Fig. 3.2, this table provides the R^2, for goodness of fit, and *P*-values, for deviation from zero, of the plots' trendlines.

A strong positive correlation (R^2 = 0.413 and P = 0.0004 (Table 3.1)) between dorsal hoof wall curvature and P3 angle of rotation was found (Fig. 3.2A). However, no significant correlation was apparent between relative extensor process depth and hoof wall curvature (R^2 = 0.003 and P = 0.789), nor relative extensor process depth and angle of rotation (R^2 = 0.031 and P = 0.387). The extensor process depth pre normalisation was observed to correlate (R^2 = 0.265) with the foot's overall height (coronet to ground), undergoing a significant increase concomitantly (P = 0.007).

3.3 Bone

3.3.1 Bone Rendered CT Images

To provide visible anatomical information on the bones of the equine foot, the binary CT images, thresholded for the segregation of the bones, were entered into the Fiji plugin, Volume Viewer. The thus volumetrically rendered images permitted the visualisation of the bones in 3D.

The three bones of the foot were able to be rendered and reconstructed together or individually. Together (Fig. 3.3), the bones' positions with respect to one another were evident, while the reconstruction of the individual bones allowed the surfaces of P2 (Fig. 3.4), the navicular bone (Fig 3.5) and P3 (Fig 3.6) to be viewed in fine detail. Moving 3D rotations of the bones were also recorded (in appendix II, see Movie 2 for the three bones together, Movie 3 for P2, Movie 4 for the navicular bone, and Movie 5 for P3).

Sections of particular anatomical interest were also generated. These included a section of trabecular bone from P3 with a resolution of 120µm (voxel size = $120\mu m^3$) from laboratory µ-CT (Fig 3.7), and a section of bone from P3 with a resolution of 8µm from synchrotron µ-CT (Fig 3.8) demonstrating porosity in both the trabecular and cortical structures.

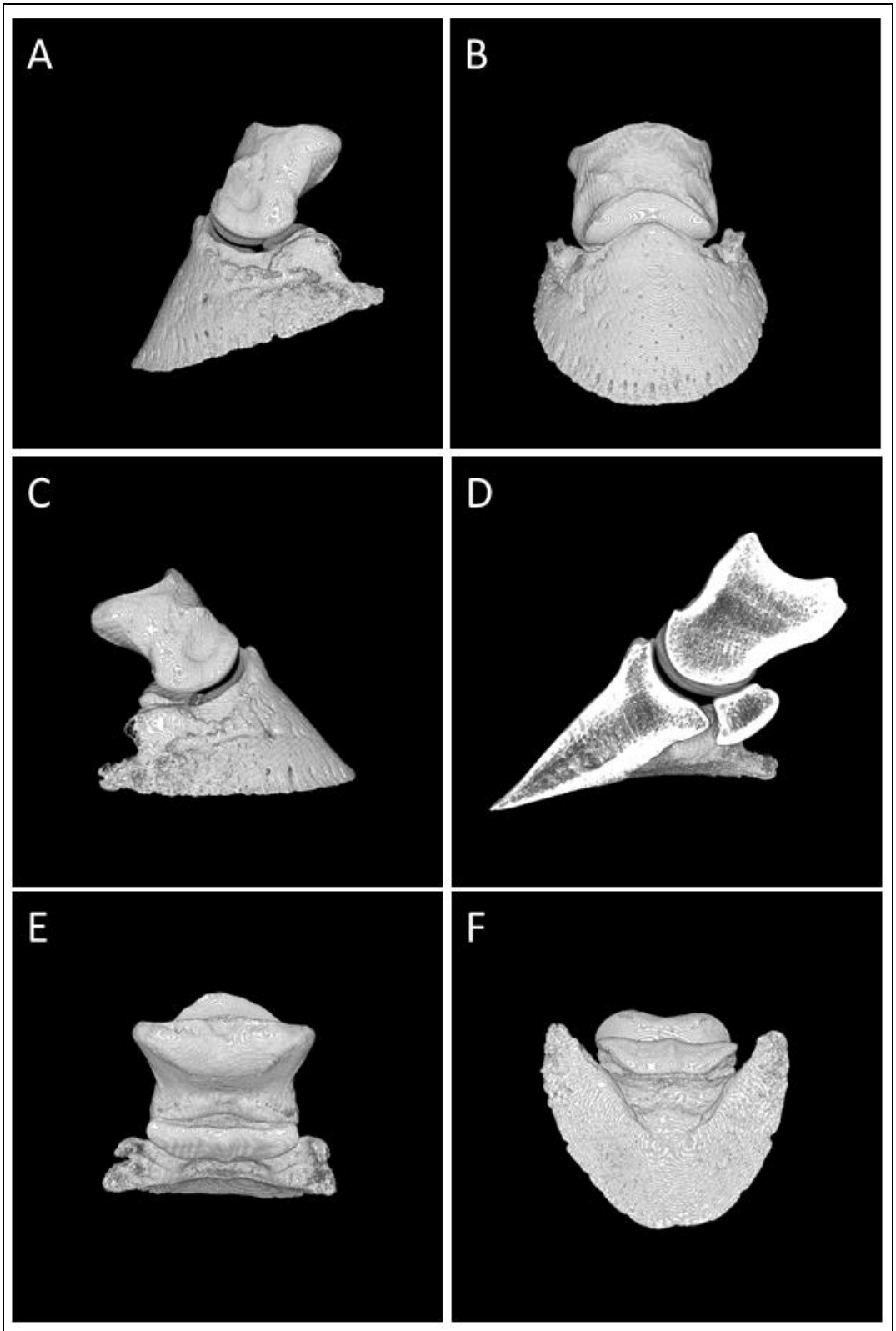


Figure 3.3: Bones of the equine foot. Reconstruction of CT images of the three bones of the equine foot, viewed (**A**) a laterally/medially, (**B**) cranially, (**C**) laterally/medially, (**D**) on the central sagittal plane, (**E**) caudally, and (**F**) ventrally. Resolution = 120µm (voxel size = 120µm^3).

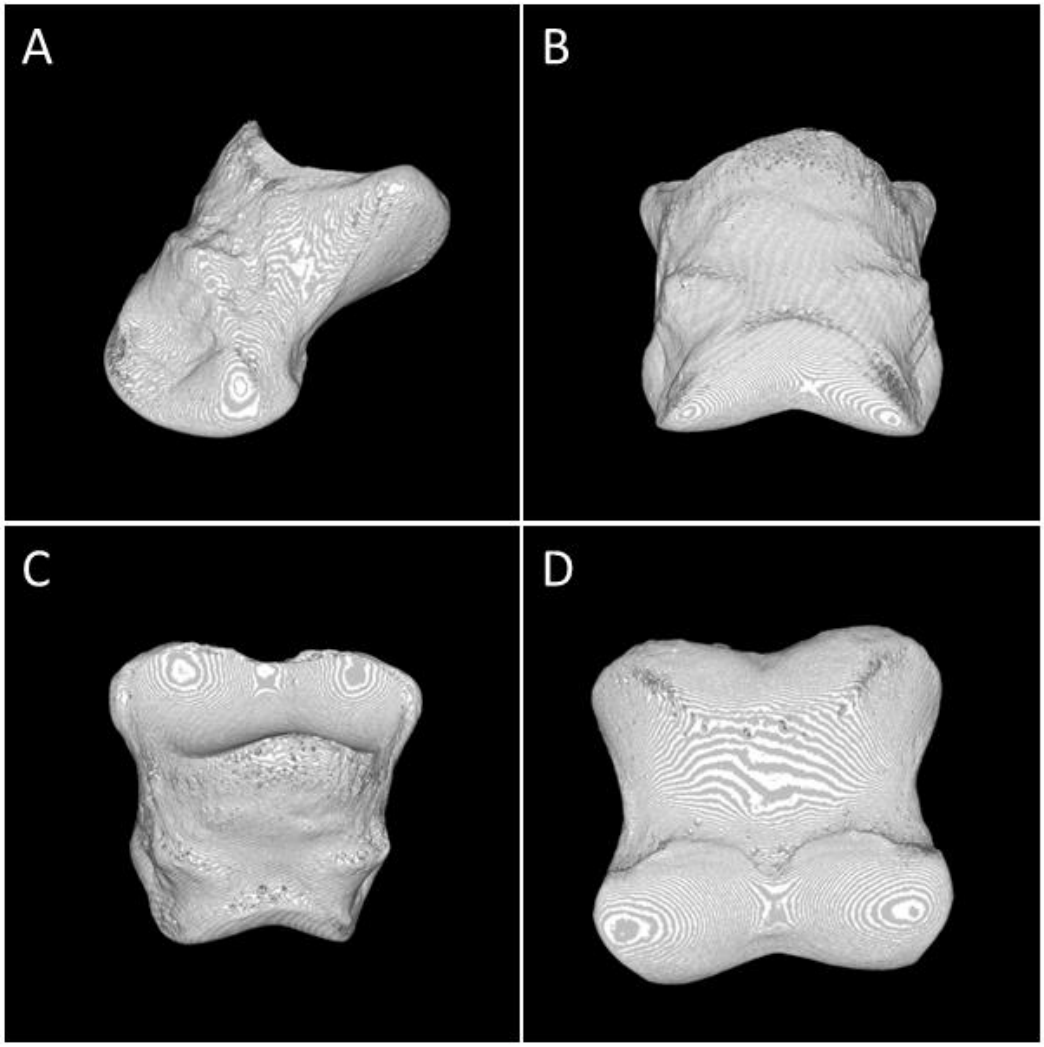


Figure 3.4: Second phalanx of the equine foot reconstructed from CT images, viewed (**A**) laterally/medially, (**B**) cranially, (**C**) dorso-cranially, and (**D**) caudally. Resolution = 120µm (voxel size = 120µm^3).

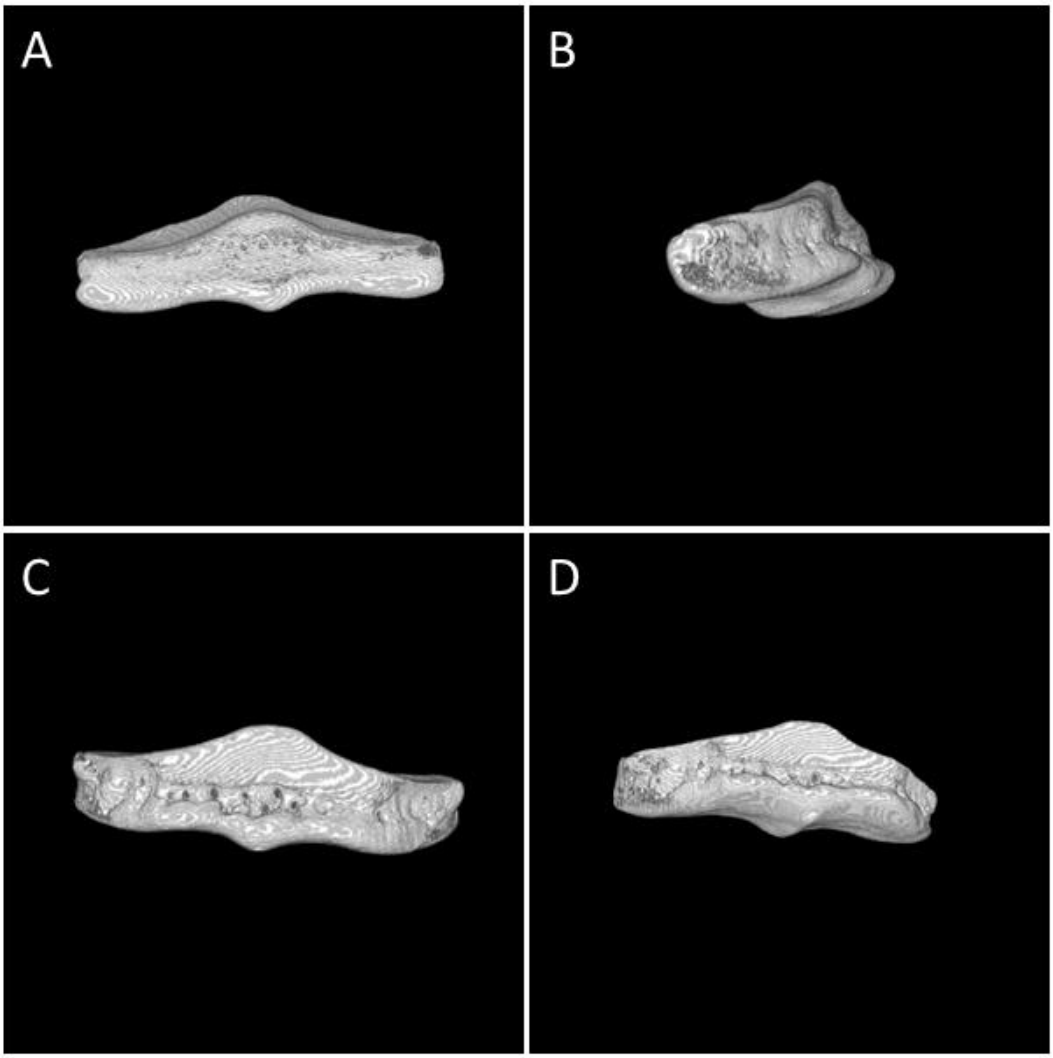


Figure 3.5: Navicular bone of the equine foot reconstructed from CT images, viewed (A) caudally, (B) laterally/medially, (C) cranially, and (D) distocaudally. Resolution = 120µm (voxel size = 120µm^3).

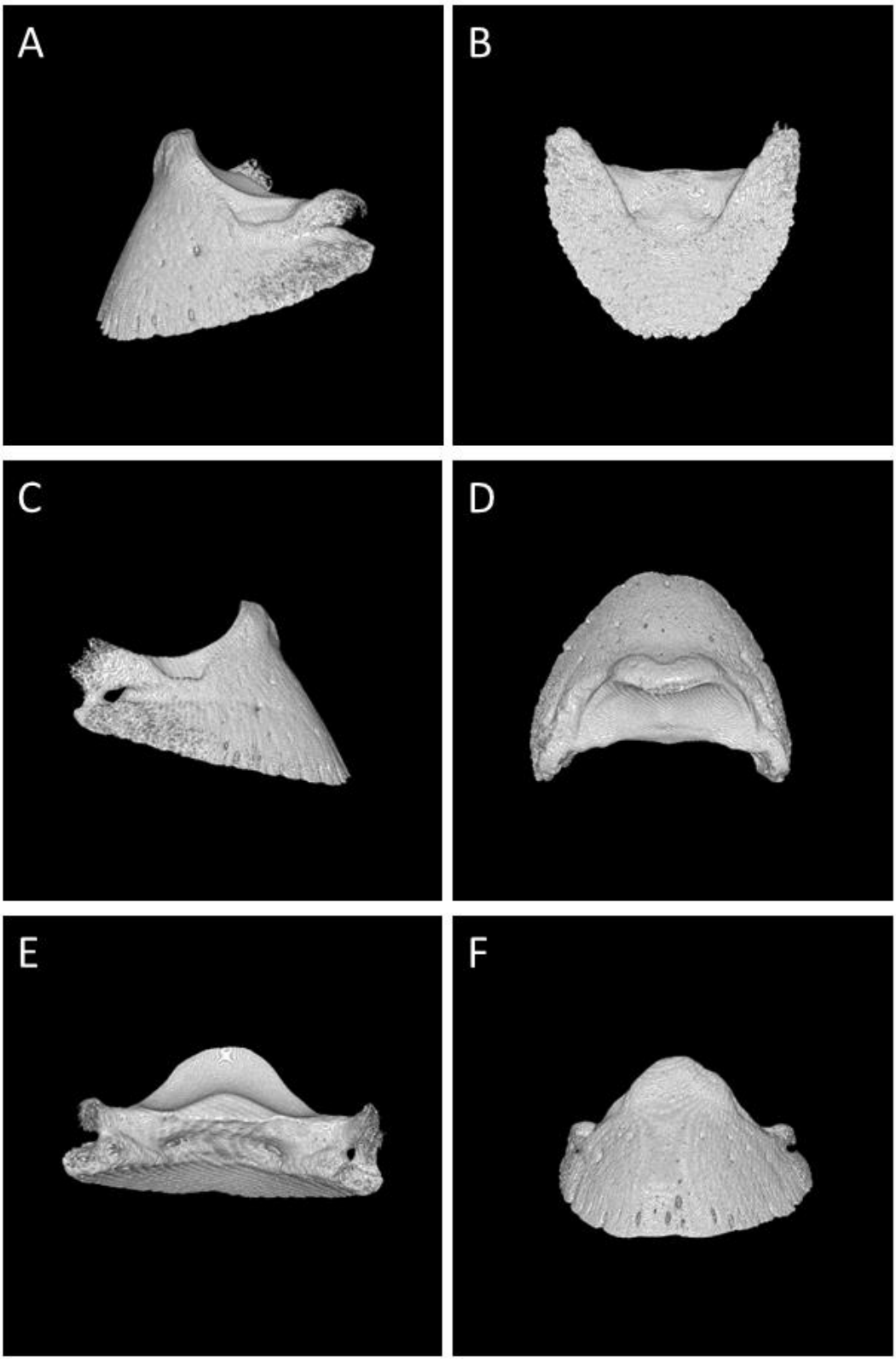


Figure 3.6: Third phalanx of the equine foot reconstructed from CT images, viewed (**A**) laterally/medially, (**B**) ventrally, (**C**) laterally/medially, (**D**) dorsally, (**E**) caudally, and (**F**) cranially. Resolution = 120µm (voxel size = 120µm3).

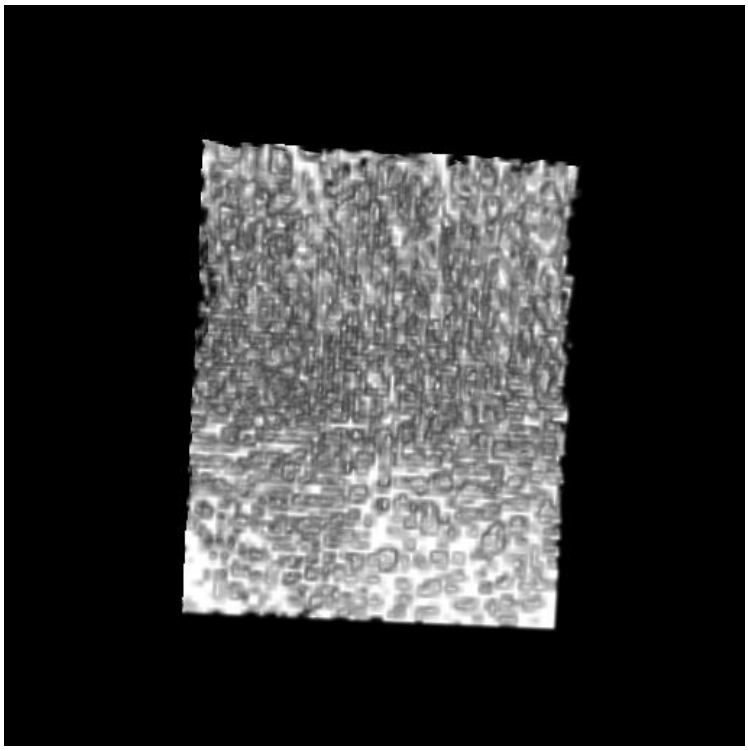


Figure 3.7: Section of trabecular bone from the third phalanx of an equine foot by laboratory µ-CT. Resolution = 120µm (voxel size = 120µm^3).

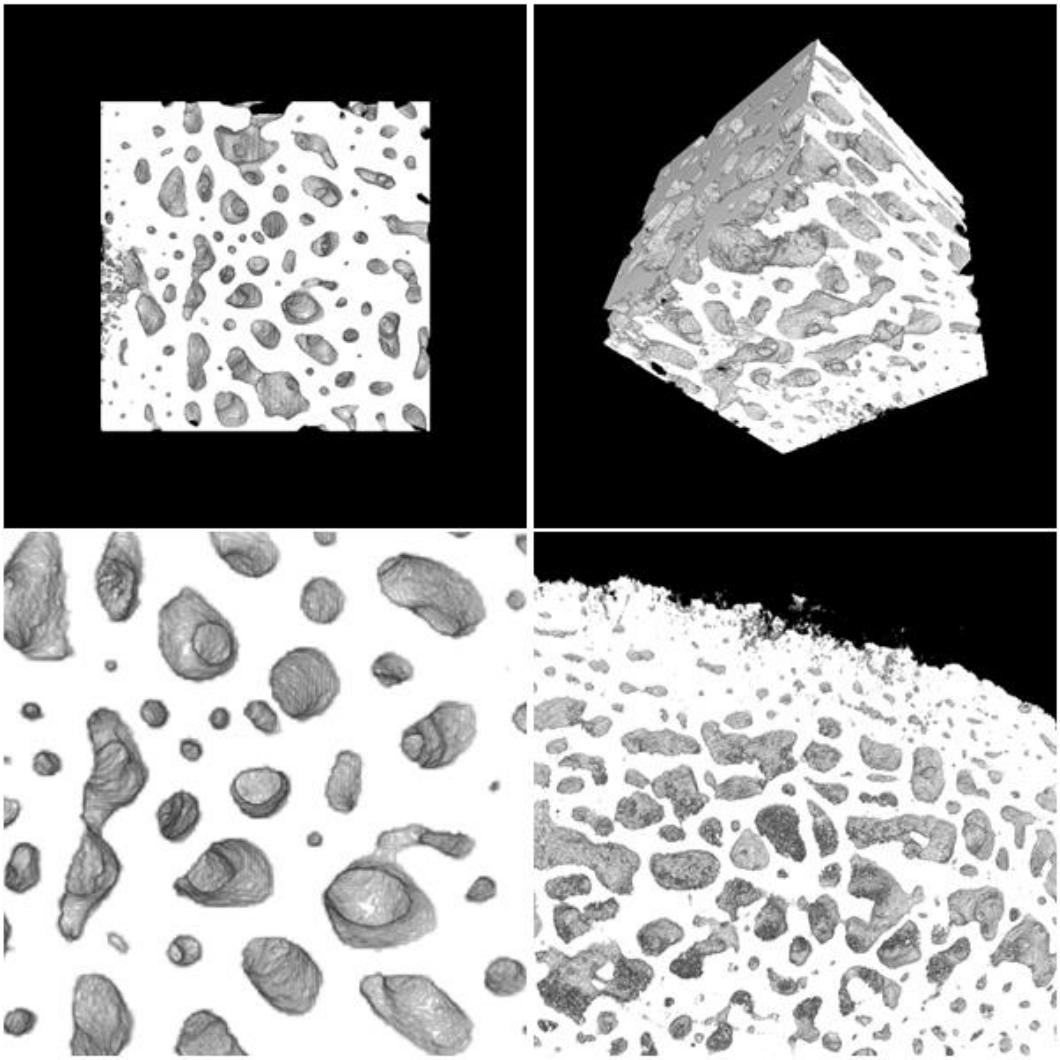


Figure 3.8: Bone section of the third phalanx of the equine foot by synchrotron µ-CT, at the interface of cortical and trabecular bone, showing the presence of finer pores in the cortical bone. Resolution = 8µm (voxel size = 8µm^3).

3.3.2 Bone Curvature

The curvature (eq. 2.8) of the dorsal aspects of P3 and of the hoof wall presented a strong (R^2 = 0.6213) non-linear positive correlation (Fig. 3.9). On the whole, positively curved hoof walls encapsulated positively curved phalanges, and negatively curved hoof walls encapsulated negatively curved phalanges. There were interestingly, however, also a number of negatively curved phalanges within positively curved feet.

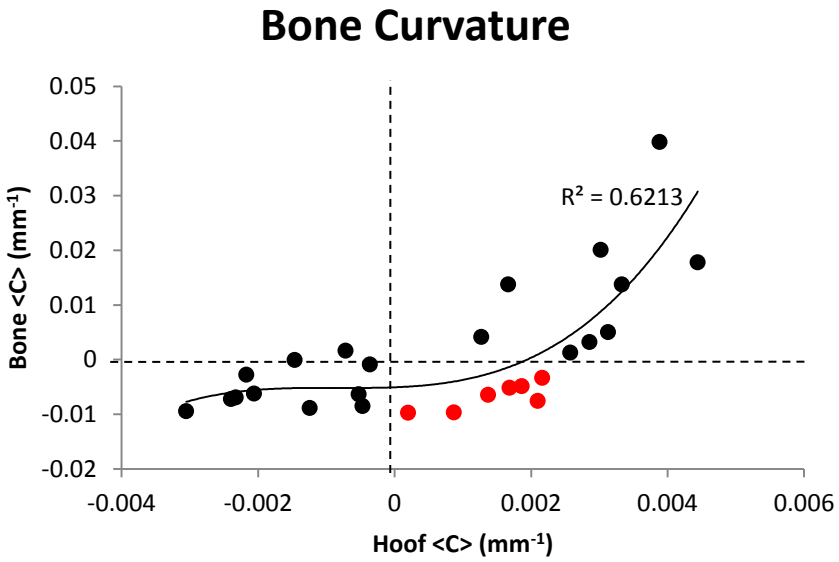
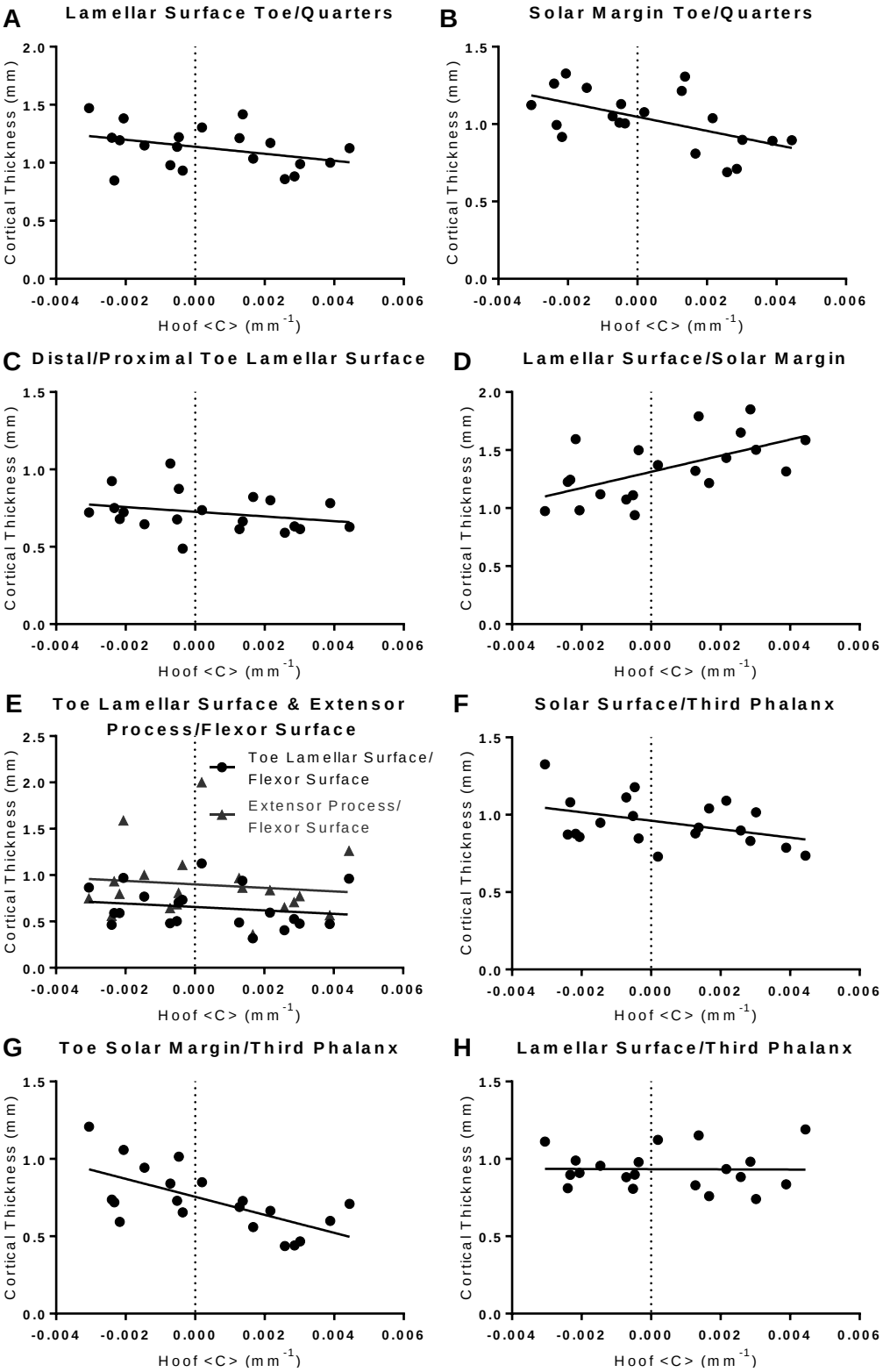


Figure 3.9: Bone curvature increases as a cubic function of hoof wall curvature. The red points indicate feet with negatively curved hoof walls overlying positively curved bones. *n*=27

Among the feet with negatively curved hoof capsules, very little variation in bone curvature existed. The aforementioned augmentation in bone curvature in correlation with increasing hoof capsule curvature was, however, evident in feet with positively curved hoof capsules. Similarly, with hoof capsule curvature temporarily aside, the magnitude of variation in the curvature of positively curved bones was around triple that of negatively curved bones.

3.3.3 Cortical Bone Thickness

The relative cortical bone thickness between ROIs was measured and related to dorsal hoof wall curvature. Relevant results are presented in graphical form in Figure 3.10, and their corresponding analyses (linear regression) in Table 3.2. The ROIs were selected as those highlighting the presence/absence of differences dorsally to ventrally (Fig. 3.10A and B), distally to proximally (Fig. 3.10C and D), at tendon attachment sites (Fig. 3.10E and F), and at lamellar attachment sites (Fig. 3.10A, C, D and E).



<u>Figure 3.10</u>: Relative cortical thickness as a function of hoof wall curvature. Region of interest ratios: (**A**) toe to quarter lamellar surface, (**B**) toe to quarter solar margin, (**C**) distal to proximal toe lamellar surface, (**D**) lamellar surface to solar margin, (**E**) toe lamellar surface and extensor process to flexor surface, (**F**) solar surface to third phalanx, (**G**) toe solar margin to third phalanx, and (**H**) lamellar surface to third phalanx. A linear regression model for each graph is provided in Table 3.2. *n*=20

	Goodness of Fit (R^2)	Deviation From Zero (P)
A - Lamellar Surface Toe/Quarters	0.141	0.103
B - Solar Margin Toe/Quarters	0.314	0.01
C - Distal/Proximal Toe Lamellar Surface	0.0734	0.248
D - Lamellar Surface/Solar Margin	0.347	0.006
E - Toe Lamellar Surface/ Flexor Surface	0.036	0.425
E - Extensor Process/ Flexor Surface	0.013	0.628
F - Solar Surface/ Third Phalanx	0.166	0.075
G - Toe Solar Margin/ Third Phalanx	0.418	0.002
H - Lamellar Surface/ Third Phalanx	0.0001	0.964

Table 3.2: Linear regression models for relative cortical thickness as a function of hoof wall curvature. For each plot featured in Fig. 3.10, this table provides the R^2 and P-values, for goodness of fit and deviation from zero respectively, of the plots' trendlines.

The results shown in Fig. 3.10 can also be visualised by the thickness maps, an integrated function of the BoneJ plugin (Doube et al., 2010), available in Fig. 3.11 and in Movie 6, appendix II.

Figure 3.10A plots the cortical thickness ratio between the lamellar surfaces of the toe and of the quarter as a function of hoof curvature. While the cortical thickness at the toe may have appeared to decrease slightly in relation to the thickness at the quarters as curvature augmented, the trend was relatively poor (R^2 = 0.141) with insignificant deviation from zero (P = 0.103).

As demonstrated by Figure 3.10B, cortical thickness at the solar margin of toe decreased in relation to that of quarters as hoof curvature augmented. This decrease was statistically significant (P = 0.01), with a relatively strong correlation (R^2 = 0.314) for the type of data analysed.

Figure 3.10C examines differences in the cortical thickness of the distal and proximal regions of the lamellar surface. No significant difference was found in the ratio of lamellar surface cortical thickness distally to proximally in relation to hoof curvature (R^2 = 0.073 and P = 0.248).

The strong correlation (R^2 = 0.347) between hoof wall curvature and the ratio of lamellar surface to solar margin thickness is shown in Figure 3.10D. Lamellar surface thickness was found to increase significantly (P = 0.006) in relation to thickness at the solar margin in line with increasing curvature.

Figure 3.10E presents two clouds of points, illustrating the poor correlation (R^2 = 0.036 and 0.013 respectively) found in the ratio of lamellar surface thickness at the toe to flexor surface thickness, and the ratio in the cortical thickness of the extensor process to that of the flexor surface as functions of hoof curvature. Very little change (P = 0.425 and 0.628 respectively) was found in either of these ratios with increasing curvature, with the thickness of both the toe lamellar surface and the extensor process appearing to remain relatively constant with respect to the flexor surface.

The ratio of solar surface to complete P3 thickness is presented in Fig. 3.10F. Solar surface thickness appeared to decrease in relation the thickness of P3 as a whole as hoof wall curvature augmented, though the goodness of fit (R^2 = 0.166) and deviation from zero (P = 0.075) were not statistically strong enough to support this.

In comparison to P3 as a whole, the solar margin (Fig 3.10G) was the ROI that underwent the greatest degree of change in correlation with hoof wall curvature (P = 0.002 and R^2 = 0.418). The solar margin significantly decreased in thickness in respect to the rest of the bone as hoof wall curvature augmented.

The lamellar surface was also compared as a ratio to the entirety of P3 (Fig. 3.10H). With a distinct lack of correlation (R^2 = 0.0001), the lamellar surface was found to neither increase nor decrease (P = 0.964) with respect to the whole bone as a function of hoof wall curvature.

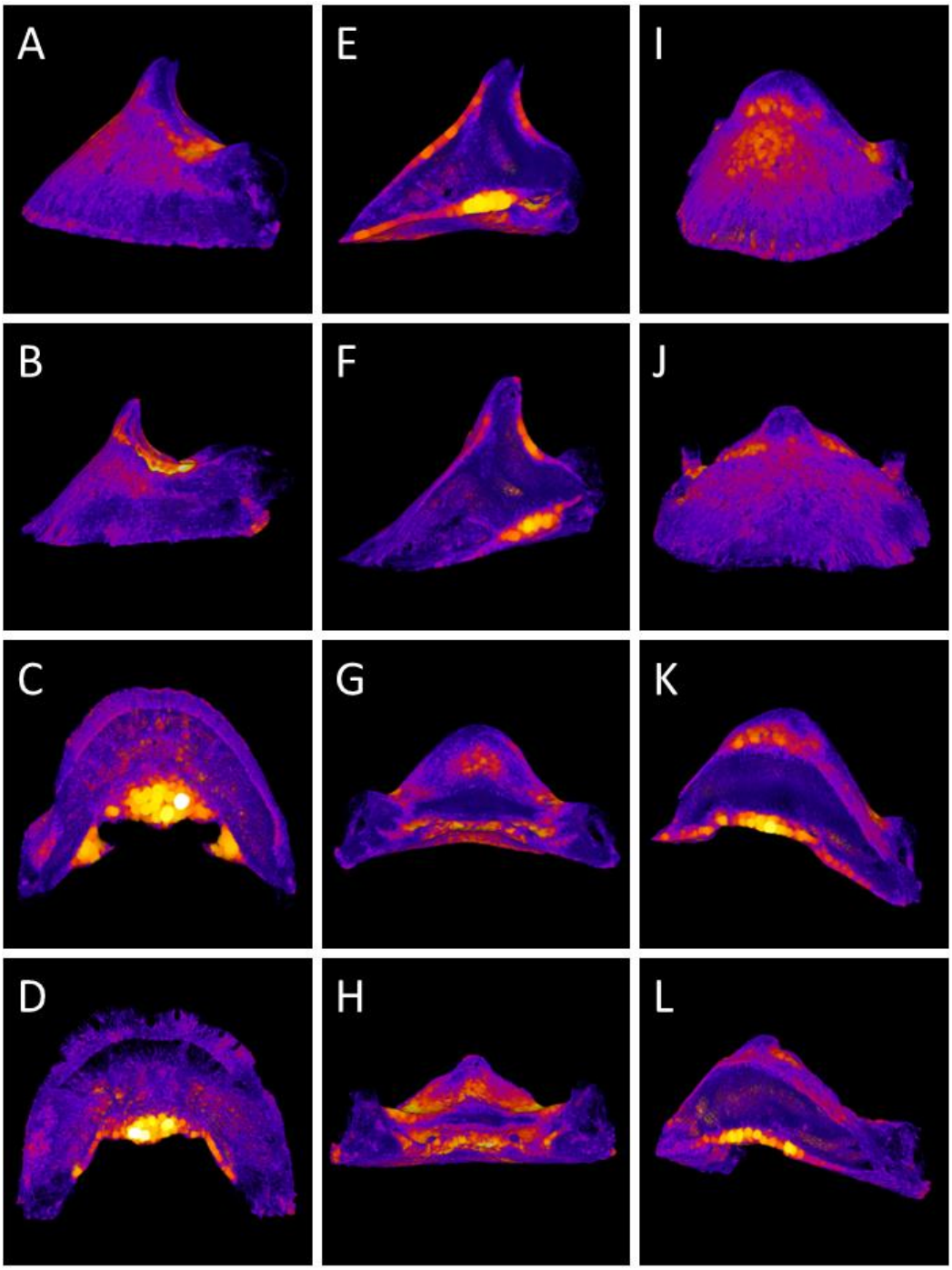


Figure 3.11: Thickness maps of third phalanges. 3D reconstruction of the graphic results of the thickness function of the BoneJ plugin applied to the third phalanx of a foot with a negatively curved hoof and a foot with a positively curved hoof. The bone thickness is mapped by the tone of the colour, where increasing brightness indicates thicker bone. Comparing negative to positive curvature respectively: (A) and (B) shows the medial/lateral view of the third phalanx; (C) and (D) axial sections passing through the flexor surface; (E) and (F) the central sagittal sections; (G) and (H) the caudal view; (I) and (J) the cranial view; and (K) and (L) coronal sections passing through the flexor surface and up though the base of the extensor process.

3.3.4 Trabecular Bone Distortion

Trabecular bone distortion was quantified in terms of anisotropy, derived from the mean intercept lengths of the eigenvectors, and of the mean intercept lengths themselves, as a function of hoof wall curvature. The resulting data are presented in Fig. 3.12A and B respectively, and their corresponding linear regression analyses in Table 3.3.

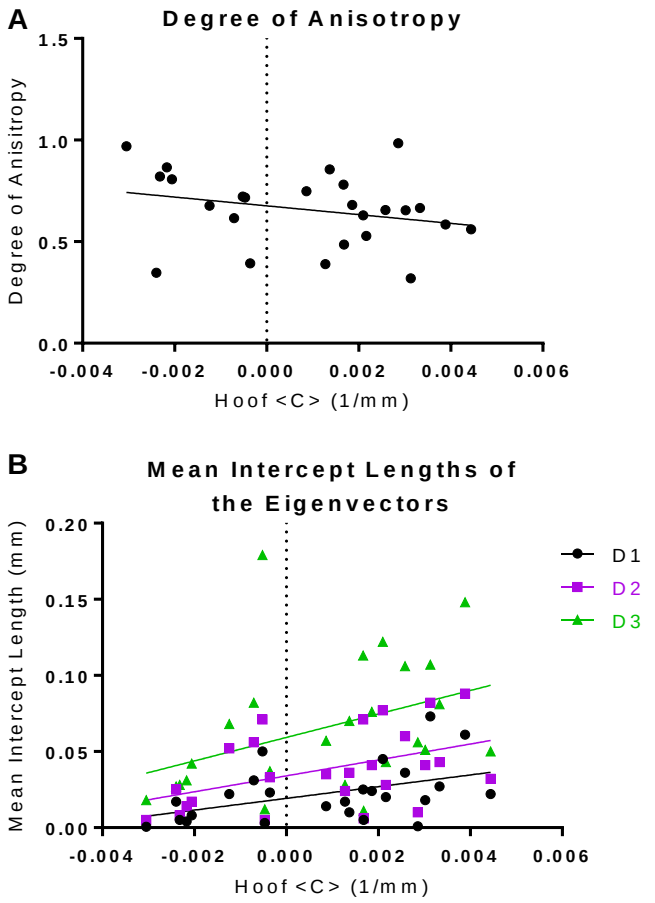


Figure 3.12: Trabecular bone distortion as a function of hoof wall curvature. Trabecular bone distortion in terms of: (**A**) the degree of anisotropy, where 0 = full isotropy and 1 = maximum anisotropy; and (**B**) the mean intercept lengths of the eigenvectors. A linear regression model for each plot can be found in Table 3.3. *n*=25

	Goodness of Fit (R^2)	Deviation From Zero (P)
A – Degree of Anisotropy	0.069	0.204
B – Mean Intercept Lengths of Eigenvector D1	0.206	0.023
B – Mean Intercept Lengths of Eigenvector D2	0.204	0.023
B – Mean Intercept Lengths of Eigenvector D3	0.153	0.053

Table 3.3: Linear regression models for trabecular bone distortion as a function of hoof wall curvature. For each plot featured in Fig. 3.12, this table provides the goodness of fit (R^2) and deviation from zero (P) of the plots' trendlines.

As demonstrated by the point cloud and low-gradient trendline of Fig. 3.12A, the trabecular bone's degree of anisotropy does not vary greatly as a function of the hoof's curvature. The linear regression model presented in Table 3.3 backs up this lack of significant correlation with and variation as a function of hoof curvature (R^2 = 0.069 and P = 0.204).

Graph B of Fig. 3.12 shows the MILs of the eigenvectors D1, D2 and D3, the three principal vector directions in which the number of interruptions of the vectors by trabeculae descends from D1 to D3. For each eigenvector, the MIL can be seen to increase as a function of hoof curvature and, as shown in Table 3.3, this is statistically significant (P = 0.023 and 0.023) in the cases of D1 and D2, in which the correlations are also good (R^2 = 0.206 and 0.204). This strength of trend is not, however, as prominent in the case of D3 (P = 0.053 and R^2 = 0.153).

3.4 Vasculature

3.4.1 Vasculature Rendered CT Images

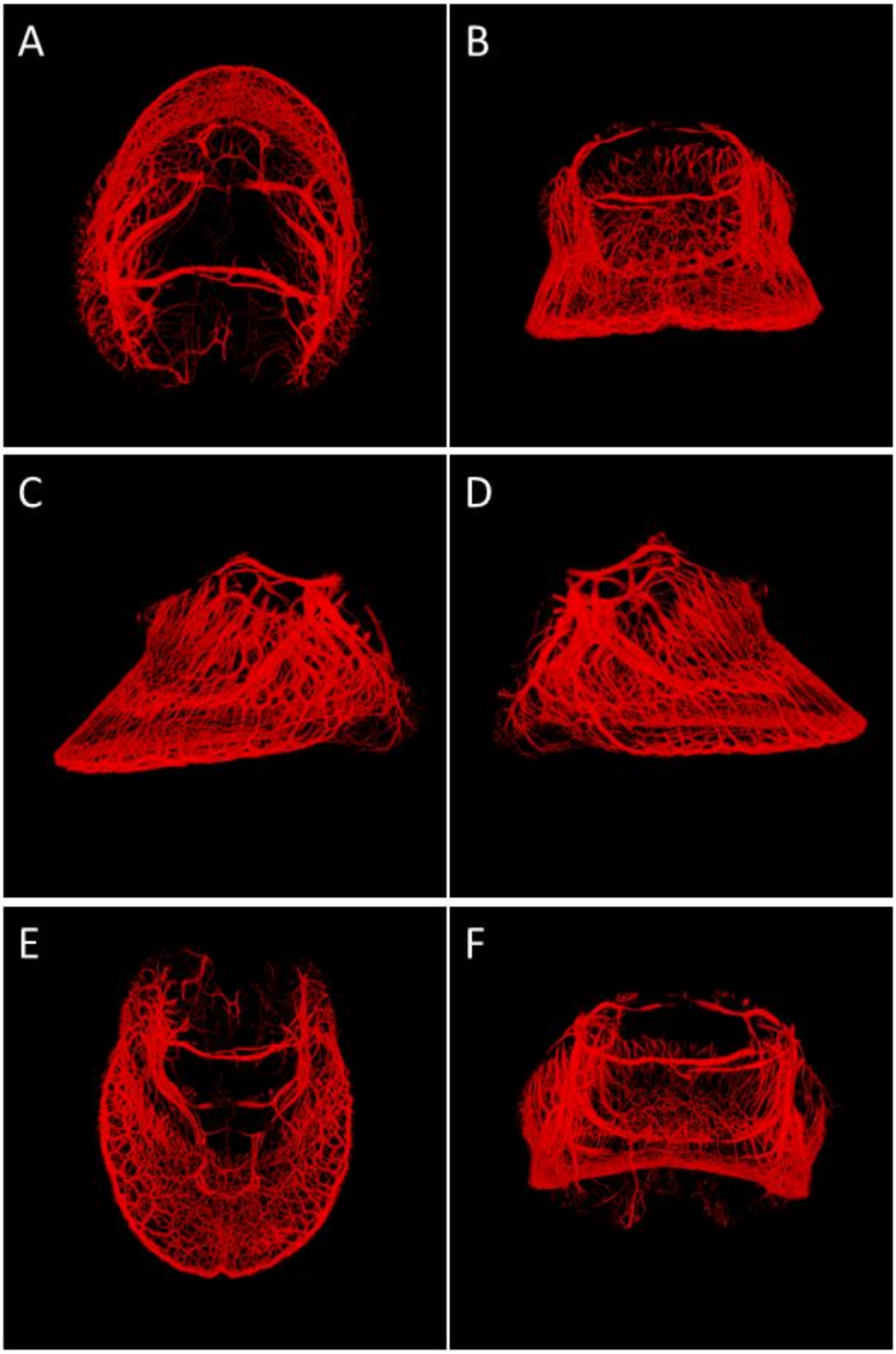


Figure 3.13: Vasculature of the equine foot, viewed (**A**) dorsally, (**B**) cranially, (**C**) laterally/medially, (**D**) laterally/medially, (**E**) ventrally, and (**F**) caudally. Resolution = 120µm (voxel size = 120µm^3).

In this study, the vasculature of the equine foot was flushed and fixed with PFA. As the PFA was absorbed into the surrounding tissues, the empty vascular lumen filled with air. This air acted as the perfect contrast medium, allowing the vasculature not only to be distinguished from the surrounding soft tissues, but also from the bone whereas, in other studies, the perfusion of a high-*Z* contrast agent resulted in images where vasculature and bone were indistinguishable (Pollitt, 2010).

The vasculature was able to be three-dimensionally reconstructed alone (Fig. 3.13 and Movie 7, appendix II), showing the full extent of the vasculature of the equine foot, and alongside the bones (Fig. 3.14, Fig. 3.15, Fig. 3.16, and Movie 8, appendix II), giving perspective to the anatomical location of important vessels. For instance, the medial/lateral digital arteries and veins, along with their branches towards the abundant heel vessels, coronary crescent and the sublamellar plexus, are evident proximal to mid-P2 (Fig. 3.14A and 3.16A). The caudal perforation of P3 by the dorsal branches, for slotting into the parietal grooves, and terminal vessels, to form the terminal arch, are also visible (Fig. 3.14B, C and D, Fig. 3.15, an Fig.16B, C, E and F), as is the anastomosis connecting the two branches of the axial parallel vein on the caudal surface of P3 (Fig.15A and D). The entire parietal surface of P3 is covered by the plexuses. The circumflex vessels are particularly apparent when viewed ventrally (Fig. 3.15).

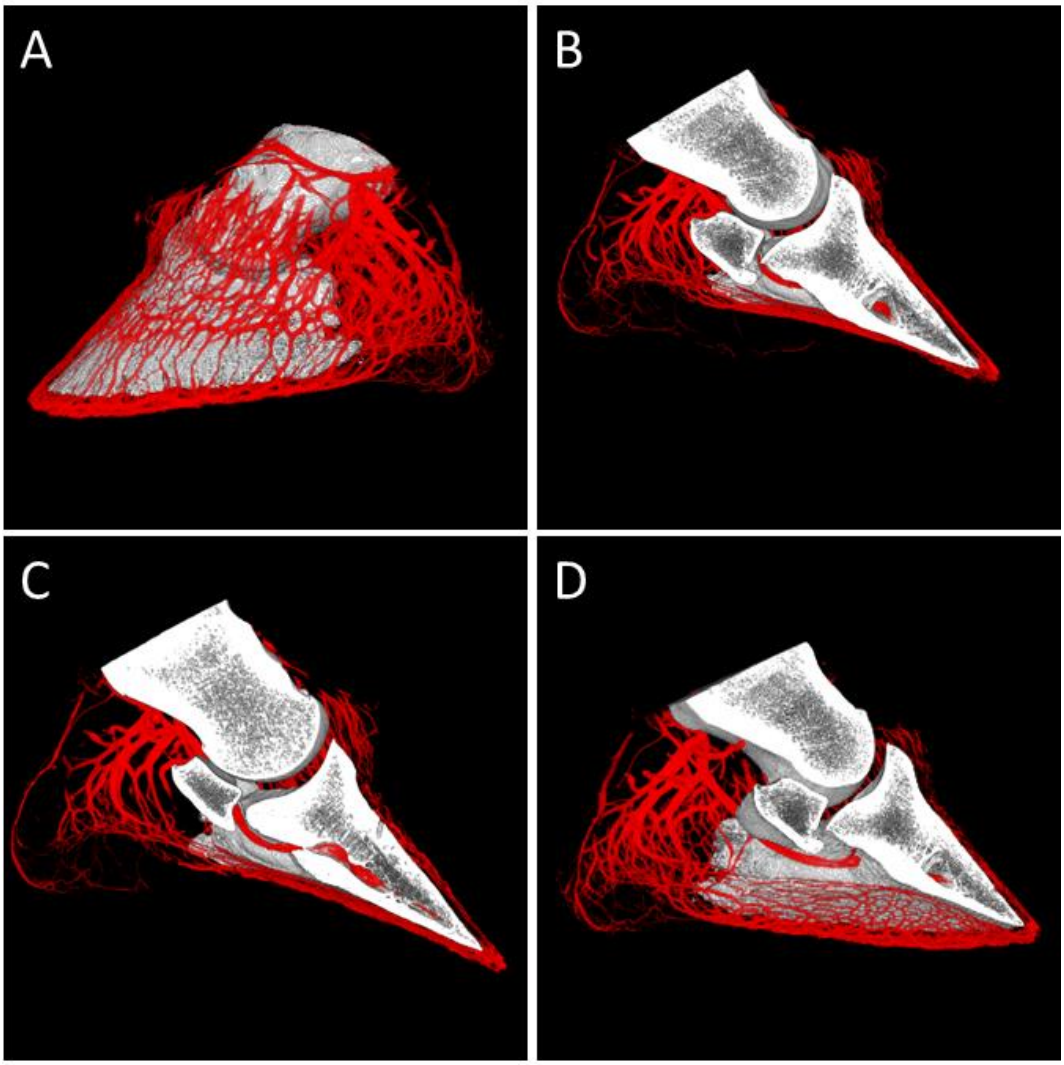


Figure 3.14: Lateral/medial views of bones and vasculature, viewed (**A**) as a whole, (**B**) cut mid-sagittally, (**C**) sagittally cut to reveal terminal branches, and (**D**) cut mid-sagittally. Resolution = 120µm (voxel size = 120µm^3).

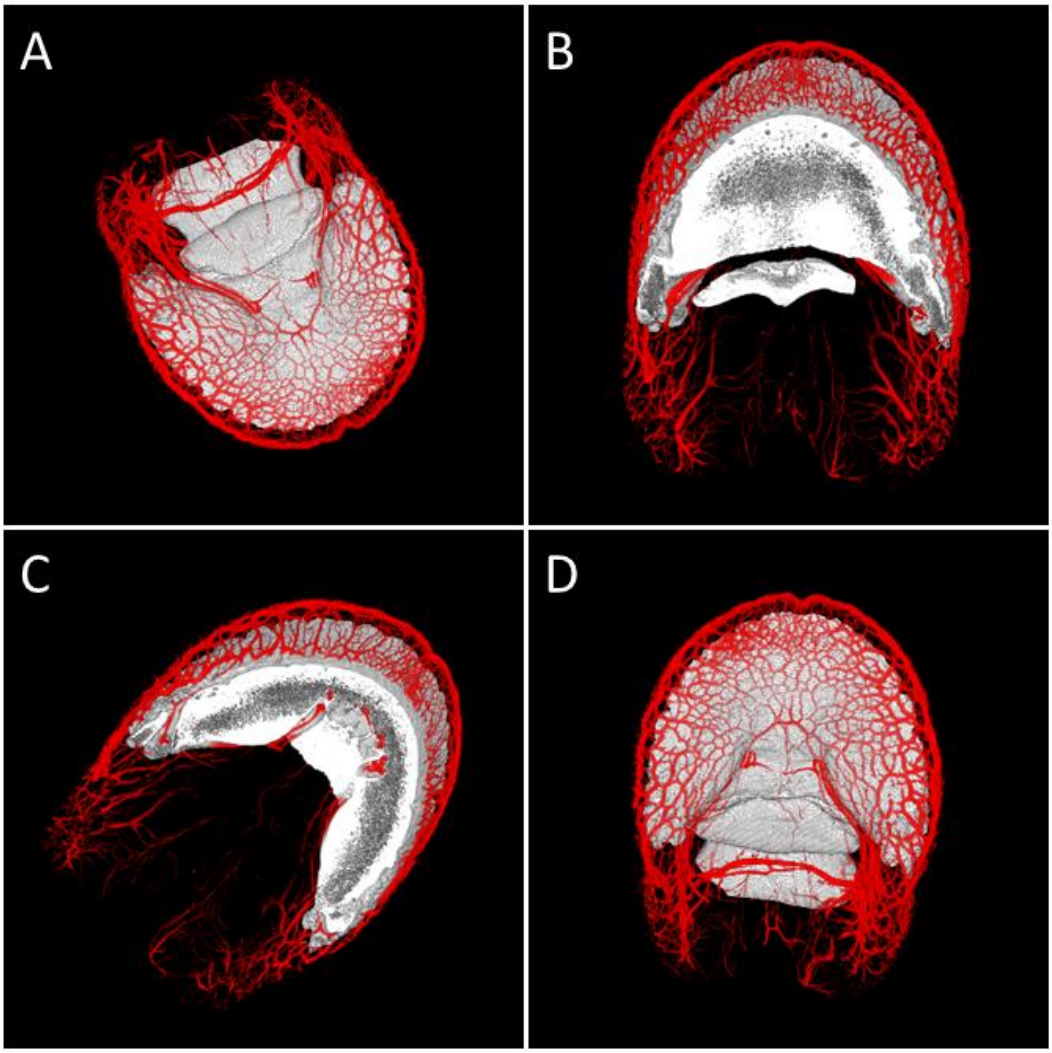


Figure 3.15: Dorsal and ventral views of bones and vasculature, viewed (**A**) ventrally as a whole, (**B**) dorsally as a mid-navicular axial cut, (**C**) dorsally as a mid-navicular axial cut, and (**D**) ventrally as a whole. Resolution = 120µm (voxel size = 120µm^3).

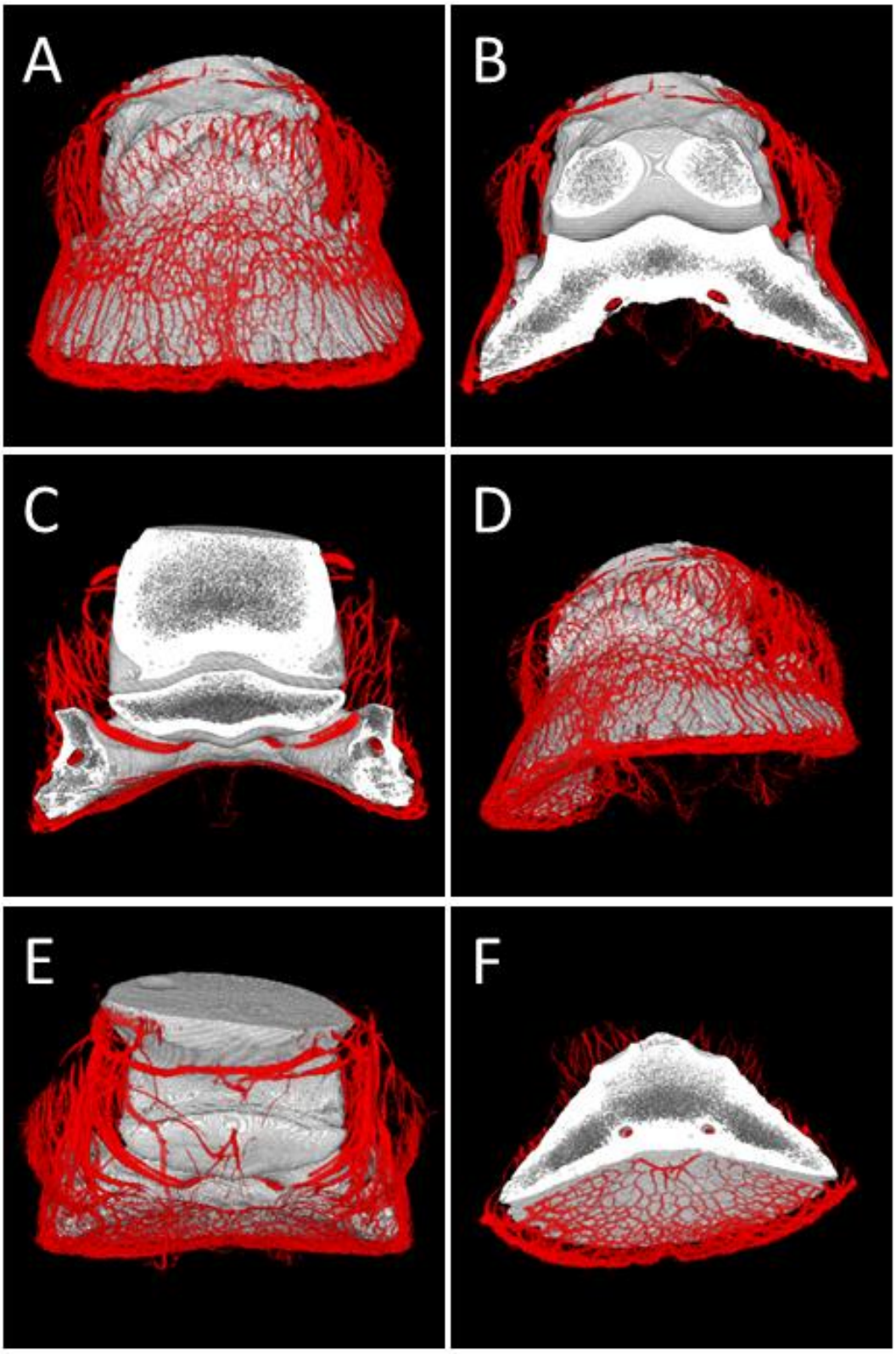


Figure 3.16: Cranial and caudal views of bones and vasculature, viewed (**A**) cranially as a whole, (**B**) cranially as a mid-P3 coronal cut, (**C**) caudally as a mid-navicular coronal cut, (**D**) cranolaterally/cranomedially as a whole, (**E**) caudally as a whole, and (**F**) ventrocaudally as a coronal cut just cranial of P2 to include only P3. Resolution = 120µm (voxel size = 120µm^3).

3.4.2 Software Development

Macro 3.2 shows the script developed, written in ijm format, for the isolation of the vasculature with Fiji/ImageJ. File names, document pathways, and image numbers can be changed as appropriate.

```
run("Image Sequence...", "open=[G:\\CT-SCAN IMAGES 2014\\M0867 - 2\\2_aligned\\YZ\\2-a-YZ_0000.tif] number=855 starting=450 sort");
run("Rotate... ", "angle=180 grid=1 interpolation=Bilinear stack");
run("Properties...", "channels=1 slices=855 frames=1 unit=1 pixel_width=1 pixel_height=1 voxel_depth=1"); // re scale in pixel dim
n=nSlices;
setSlice(n/2);
setOption("BlackBackground", true);
run("Convert to Mask", "method=IJ_IsoData background=Dark black");
run("Duplicate...", "title=Hoof_2-1 duplicate range=1-855");
run("Fill Holes", "stack");
run("Remove Outliers...", "radius=10 threshold=50 which=Bright stack");
run("Remove Outliers...", "radius=2 threshold=50 which=Dark stack");
run("Erode", "stack");
run("Erode", "stack");
run("Erode", "stack");
run("Erode", "stack");
selectWindow("YZ");
run("Invert", "stack");
run("Remove Outliers...", "radius=2 threshold=50 which=Dark stack");
imageCalculator("Multiply create stack", "YZ","Hoof_2-1");
run("Remove Outliers...", "radius=0.5 threshold=50 which=Bright stack");
run("Image Sequence... ", "format=TIFF name=H2_YZ_V save=[G:\\CT-SCAN IMAGES 2014\\M0867 - 2\\Blood_Vessels\\Full\\H2_YZ_V0000.tif]");
run("Close");
run("Close");
run("Close");
```

Macro 3.2: Vasculature isolation. For Fiji/ImageJ for the creation of binary image stacks of the blood vessels from tomograms.

3.4.3 Vasculature Diameter

Changes in the foot's vasculature were assessed in terms of vessel lumen diameter ratio in the lamellar and solar plexuses of the toe region. The numerical results are represented in Fig. 3.17A, along with graphical reconstructions in the toe region (B and C) and foot as a whole (D and E).

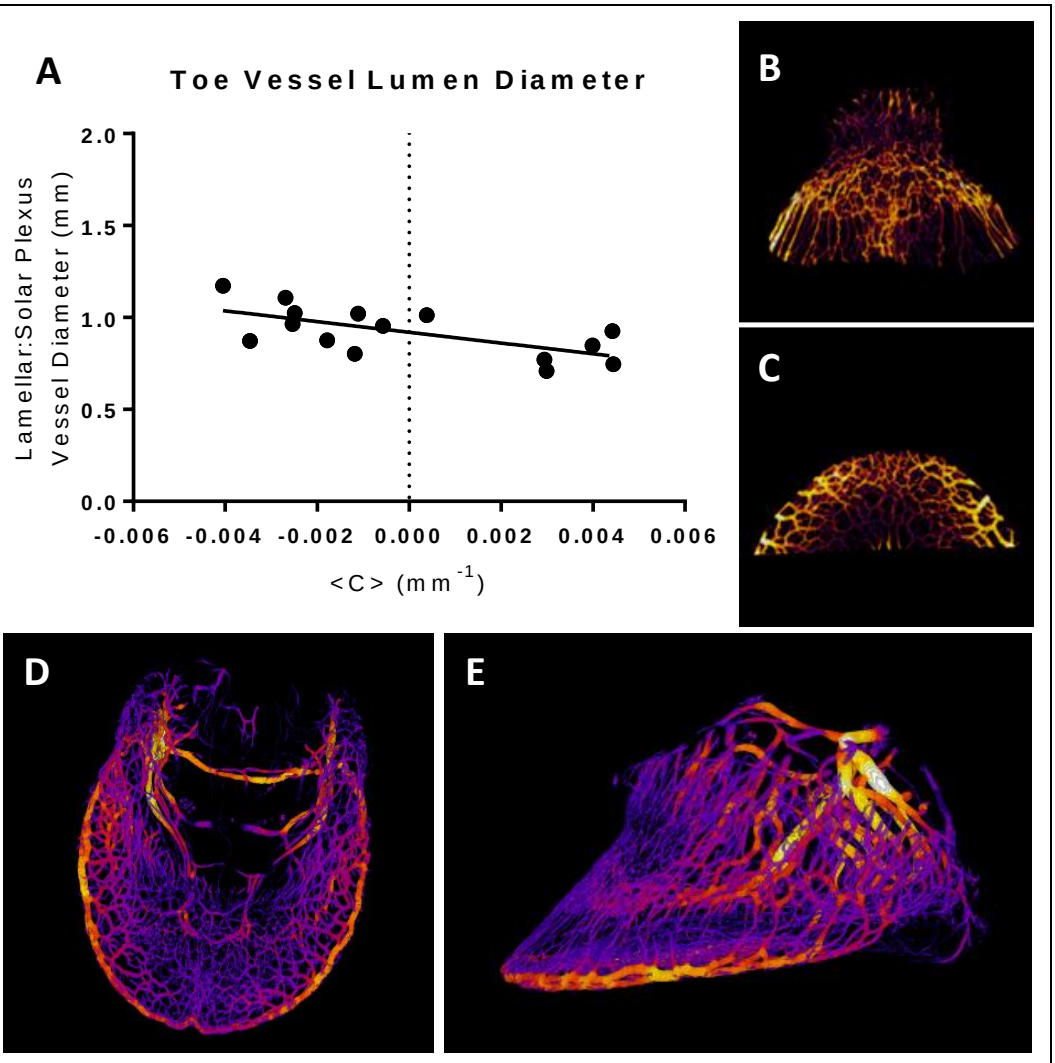


Figure 3.17: Blood vessel lumen diameter, with (**A**) representing the ratio of sublamellar to solar plexus vessel diameter in the toe as a function of hoof wall curvature, and the remaining images showing 3D representations of blood vessels rendered from CT images to which the BoneJ plugin's thickness function has been applied. These include the blood vessels of (**B**) the sublamellar plexus of the toe, (**C**) the solar plexus of the toe, (**D**) the entire foot from a palmar/plantar perspective, and (**E**) the entire foot from a lateral perspective. *n*=15

A strong correlation (R^2 = 0.43) was found between blood vessel lumen diameter in the toe and hoof wall curvature. The mean lumen diameter of the blood vessels in the sublamellar plexus were found to significantly decrease (P < 0.0001) in relation to the diameter of those in the solar plexus of the toe as a function of augmenting hoof wall curvature.

3.5 Lamellae, Papillae and Keratogenesis

3.5.1 Microstructure Rendered CT Images

The laboratory µ-CT scans of the sections cut from the proximal edge of the hoof wall (see section 2.3.1.2) revealed microstructures of the equine foot that were able to be rendered into 3D images, providing an unprecedented close-up view of their undamaged topography. The dermal lamellae (Fig. 3.18 and Movie 9, appendix II) were visible as parallel rows of primary lamellae, covered in parallel secondary lamella rows. Protruding from the dense vascular network of the coronary corium were the dermal papillae (Fig. 3.18 and Movie 10, appendix II), curving downward proximally before descending straight, in parallel to the hoof wall.

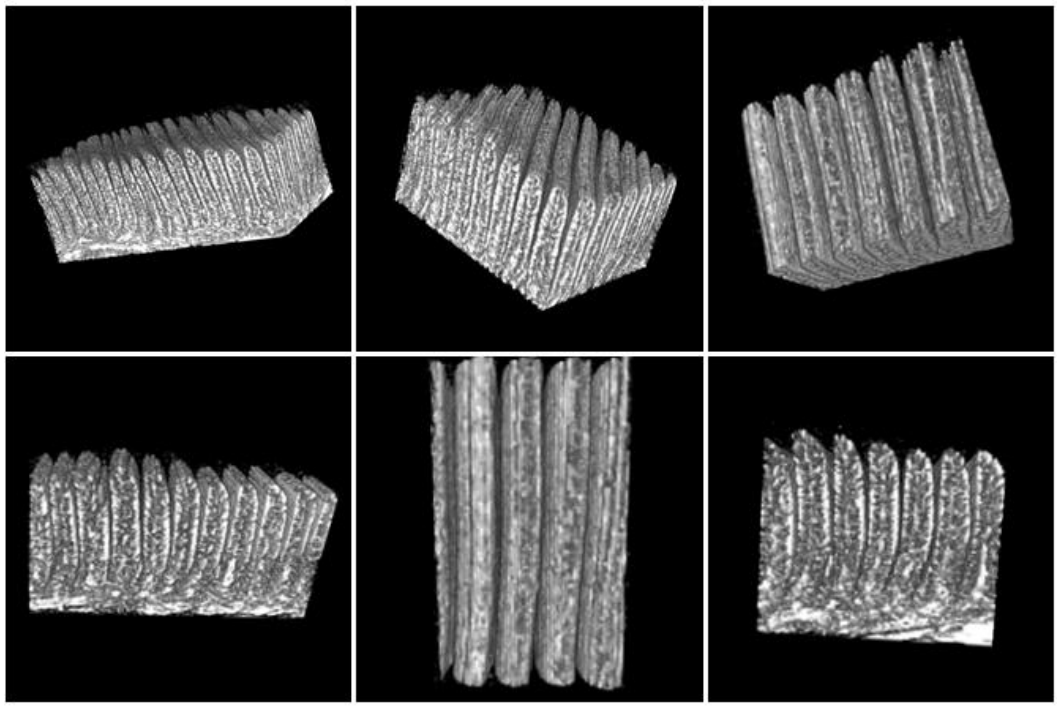


Figure 3.18: Dermal lamellae of the equine foot from laboratory µ-CT. Resolution = 18µm (voxel size = 18µm^3).

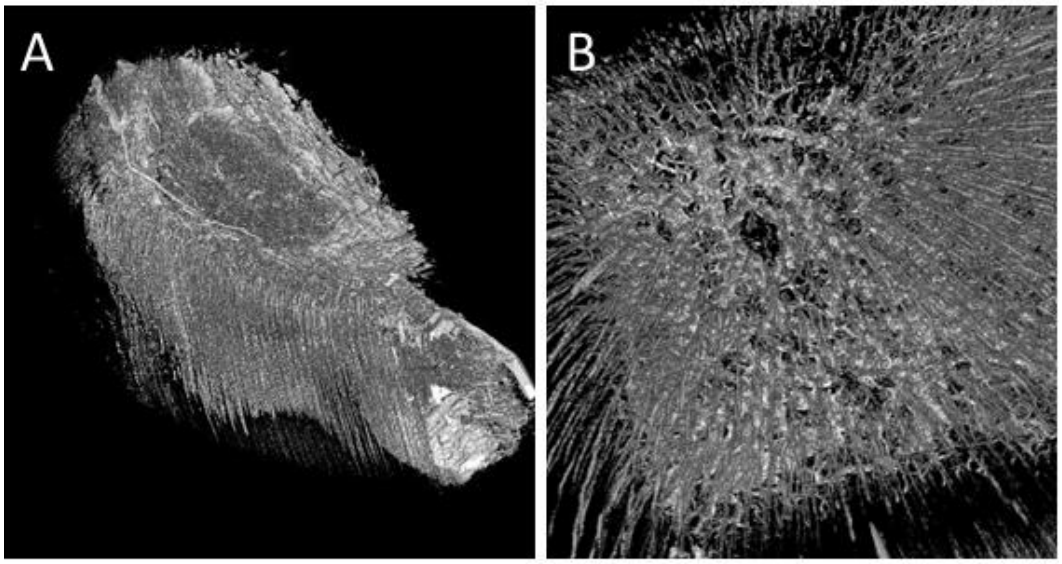


Figure 3.19: Dermal papillae of the equine foot from laboratory µ-CT, viewed (**A**) laterally/medially and (**B**) at their distal extremity. Resolution = 18µm (voxel size = 18µm^3).

The ROI scans of the coronet region of an intact equine foot using synchrotron µ-CT (see section 2.3.2) enabled a high resolution (8µm), clear view of the dermal papillae (Fig. 3.20 and Movie 11, appendix II). The papillae of the hoof wall's s*tratum externum*, *stratum medium* and *stratum internum* were easily distinguishable.

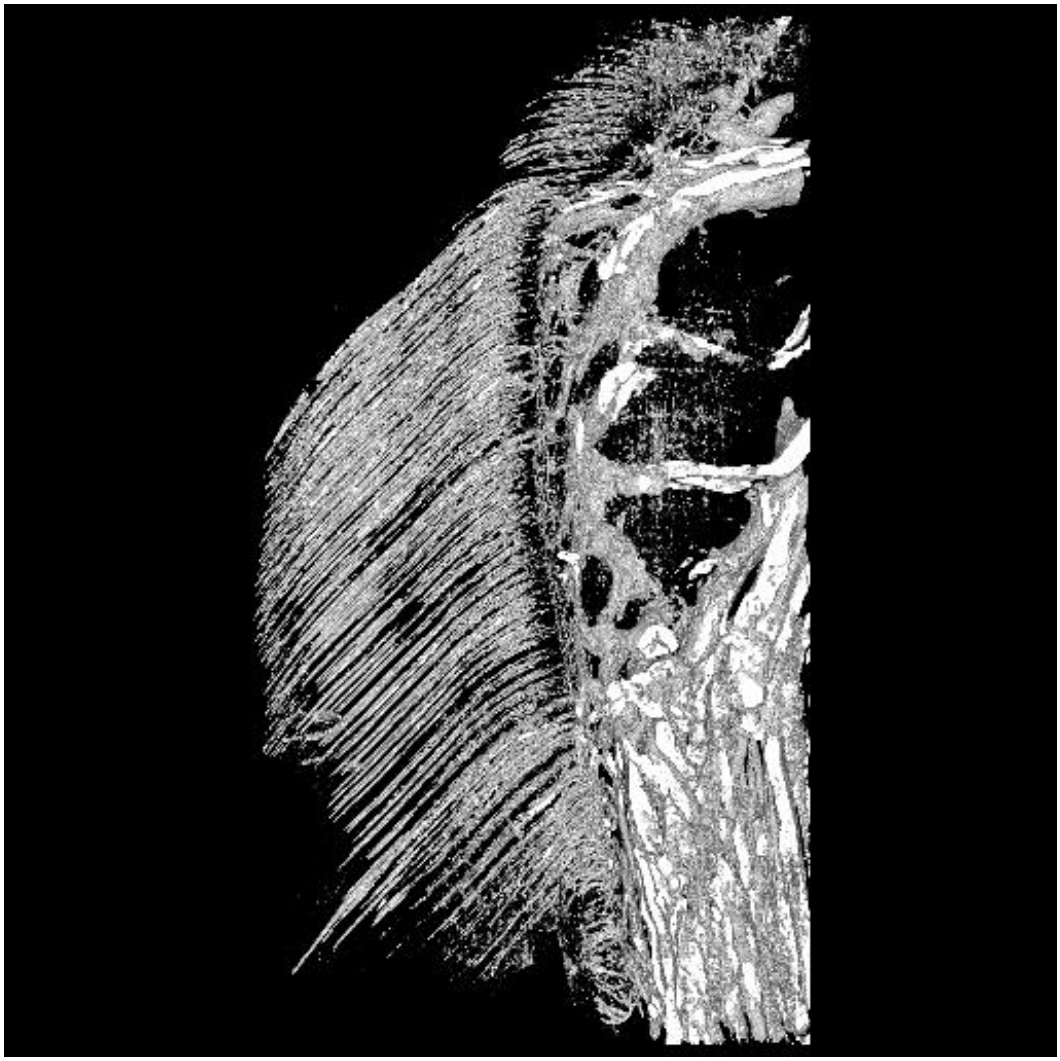


Figure 3.20: Dermal papillae of the equine foot from synchrotron μ-CT. Resolution = 8μm (voxel size = 8μm^3).

3.5.2 Papilla Morphology

The mean diameter and length of the coronary dermal papillae of the *strata externum*, *medium* and *internum* from the synchrotron μ-CT images of the dorsal equine foot were measured. These, along with their standard deviations are presented in Fig. 3.21.

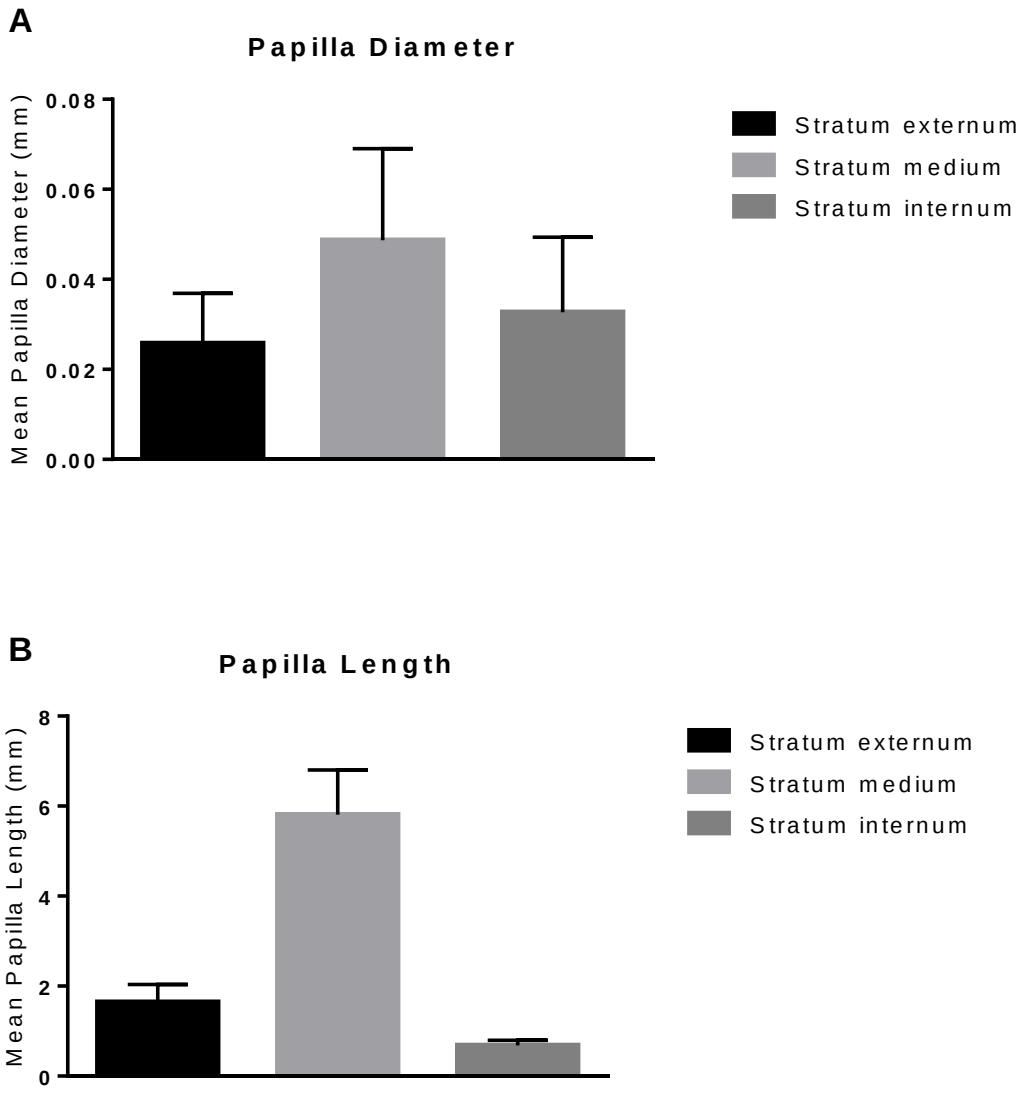


Figure 3.21: Papilla morphology, showing (**A**) mean papilla diameter, and (**B**) mean papilla length of the *strata externum*, *medium* and *internum* of the dermal papillae. Error bars show standard deviation of the mean. N=10 papillae measured per stratum, statistical correlations were not carried out as this preliminary data is from one hoof.

The *stratum externum* had, on average, the narrowest papillae with a mean of 0.02576mm (SD = 0.011), but middling in length with a mean of 1.642mm (SD = 0.392). In terms of surface area, this equated to around 0.133mm^2, middling in size.

The papillae of the *stratum medium* were the greatest in terms of both diameter and length, with means of 0.049mm (SD = 0.02) and 5.807mm (SD = 0.994) respectively. This gives them the largest average surface area of 0.891mm^2.

Of middle-sized width were the papillae of the *stratum internum*, with a mean of 0.033mm (SD = 0.017). These papillae were, however, significantly the shortest, with a mean length of 0.682mm (SD = 0.117), giving them a relatively smaller 0.071mm^2 surface area.

Little variability was present in the diameters and lengths of the papillae of the same region from each of the three regions, with a CV below one in each instance.

3.5.3 Coronary Epidermal Cell Proliferation

As a related study carried out by Ramzi Al-Agele, immunohistochemistry was used to assess proliferation index differences between the toe and the quarter/heel coronary epidermis. The ratio of these PIs (mean quarter and heel to toe) was compared to the dorsal curvature measurements obtained from the CT images of the present study.

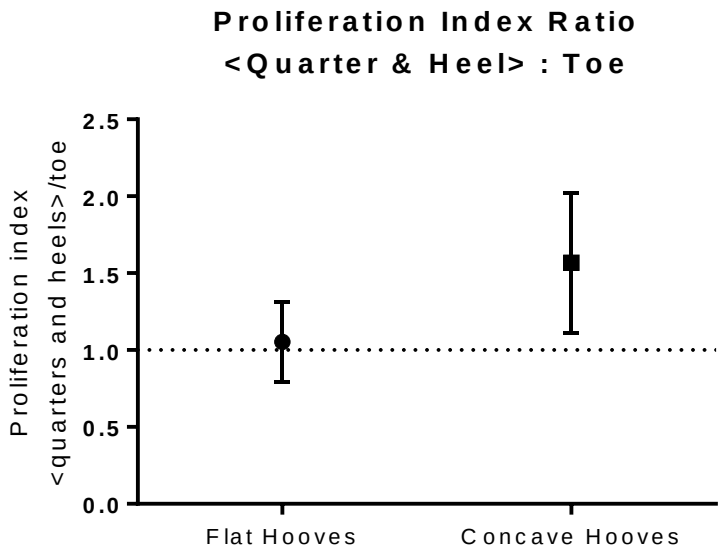


Figure 3.22: Proliferation index of quarter/heel mean in relation to the toe in hooves with flat and concave wall profiles. Calculated as % of P63 positive cells in the *stratum basale* of the quarters and heels as a mean divided by the toe. Error bars show standard deviations. Flat *n*=7 and concave *n*=5

As indicated by the mean ratios presented in Fig. 3.22, the PI of the quarters and heels was observed to be higher in relation to that of the toe in feet with concave (mean curvature > 0.001) dorsal hoof wall profiles than in those with flat profiles (mean curvature < 0.001 and > -0.001). With a ratio close to one (1.054), the mean PI in the quarter and heel regions was very similar to that in the toe region in feet with a neutral (flat) curvature while, with a ratio of 1.567, proliferation appeared higher in the quarter/heel regions than in the toe in feet with a positive curvature. A CV mean of 0.247 (SD = 0.261) in flat-profiled

hooves and of 0.289 (SD = 0.453) in concave hooves, being below one, serves to back up these observations.

4 Discussion

4.2 Characterisation of Pathomorphology

The chronically laminitic foot has a number of characteristic pathomorphological features. Those affecting the hoof capsule, and which are therefore outwardly detectable, include a widening of the white line in the toe region, the appearance of growth rings which diverge at the heels, a dorsal concavity (positive curvature) of the hoof wall, and a decreased angle between the ground and the distal-dorsal aspect of the hoof wall (Eustace, 2010). Radiographic investigation unveils a certain degree of displacement of P3, either in terms of rotation or of sinking, with respect to the hoof capsule and to the axes of the two other phalanges. The angle between the dorsal surface of the hoof wall and the parietal surface of P3, and that between the palmar surface of P3 and the ground, the distance between the coronet and the summit of the extensor process, the thickness of the capsule and lamellar zones at the base of the extensor process and the tip of the solar margin, and the thickness of the sole at the tip of the solar margin of P3 are features commonly used in the quantification of P3 displacement (Taylor et al., 2014, Floyd, 2007).

Easily quantifiable from the mid-sagittal sections of the CT images, dorsal wall curvature and angle, P3 rotation indicated by the angle between the dorsal surfaces of the hoof wall and of P3, and P3 sinking measured by the depth of the summit of the extensor process from the coronet, were taken as physical determinant of the pathological state of the feet in this study. Hoof curvature was chosen as the primary physical descriptor due to its accurate measurability and lack of subjectivity in comparison to the two radiographic features, and its independence from natural conformational variability as compared to capsule angle. So as to justify the use of curvature as the sole physical descriptor with which to compare all of the obtained data, its correlation to the three remaining descriptive features was checked.

The correlation between curvature and angle was investigated by assessing the ratio of the former to the latter. Rather than the standardly measured angle between the hoof wall and the horizontal ground, this study focussed on the adjacent angle between the hoof wall and the vertical (90^{o} to the ground), as this measurement provides a better indication of force transmission, useful in aspects of the project that are not covered here. Natural variation in hoof conformation and size was accounted for by normalising the curvature through multiplication with its centre of curvature. With mean ratios nearing one, and low coefficients of variation in both instances, a good correlation between hoof curvature and angle was evident.

Plotting the angle of rotation of P3 as a function of hoof curvature revealed a strong positive correlation between the two. That P3 rotation occurs as a result of laminitis is established knowledge and is omnipresent within the literature (Eustace, 2010, Floyd, 2007, Redden et al., 2007, Hunt and Wharton, 2010). A positive curvature to the dorsal aspect of the hoof wall is also colloquially renowned in defining a laminitic foot, and its correlation to P3 rotation could therefore have been predicted, at least on a qualitative level. The quantitative nature of the data, however, and the strength of the linear correlation observed, serves as affirmation that positive curvature is indeed a defining physical feature of the laminitic hoof.

The depth of the summit of the extensor process from the coronet, normalised by its use as divisor to hoof height to take account of foot size variability, bore no apparent correlation to either hoof wall curvature or the angle of rotation of P3. This lack of correlation is not altogether surprising given the nature of Fatal Sinker Syndrome (FSS): cases do not consistently present the usual pathomorphological changes to the hoof capsule described above; where growth rings appear, they tend to remain parallel to the coronet rather than divergent; the high morbidity, as indicated in the name, and poor prognosis of the syndrome may result in euthanasia prior to the onset of the chronically laminitic features (Floyd, 2007). It should also be noted that sinking is a less common outcome of laminitis than rotation, with one illustrative study describing a 26% occurrence of sinking as opposed to an 80% incidence of rotation in horses euthanized due to laminitis (Hunt and Wharton, 2010). Together, these factors rendered the likelihood of an FSS afflicted animal being present amongst those randomly sampled low. Furthermore, the normal range for extensor process depth seems highly subjective with, for instance, one study stating an acceptable maximum of 9.7mm (Cripps and Eustace, 1999), another 14mm (Floyd, 2007), and a third 15mm (Redden et al., 2007). These figures seem not, however, to have undergone any normalisation to account for hoof size variability. As the results in the present study indicate a strong positive correlation between extensor process depth and hoof height, a normalised measurement of extensor process depth would seem far more qualitative than one in its untouched state. Of the 26 feet sampled, only one surpassed an extensor process depth of 15mm in its pre-normalised state but, because of its particularly large foot, its normalised extensor depth happened to be the lowest. After consideration of all of the aforementioned factors, the decision was made to work on the assumption that no “sinkers” were present amongst the feet sampled.

With its strong correlation to hoof wall angle and to the angle of rotation of P3, along with its easy and accurate measurability, dorsal hoof wall curvature was

chosen as the most suitable candidate for the physical descriptor of the pathologic status, in terms of chronic laminitis, of the horse feet under scrutiny in this study. Furthermore, this method can be employed in an approximated fashion “in the field” using standard photography with a well-aligned camera and a calibration bar taped to the lateral hoof wall.

4.3 Bone Remodelling

As a physiologically active tissue, bone's high adaptability to its environment can provide insight into the pathophysiological status of its surroundings (Clarke, 2008). While the osseous remodelling processes may be induced through a number of mechanisms, the current study focussed on the exploitation of the bone's adaptive capabilities in terms of gross shape, cortical thickness, and trabecular anisotropy for the investigation of biomechanical force imbalances.

From the observation in section 3.2.1 that the dorsal surfaces of the bone and of the hoof capsule have a tendency to assume a similar shape, inference could be made that distortion in one might apply sufficient strain to the other to cause its equivalent deformation (Cornette et al., 2015). The visible lack of variation in the bone curvature of negatively curved bones as a whole, regardless of hoof capsule curvature, along with the negatively curved bone shape of feet with straighter hoof capsule profiles, could suggest that convexity of the dorsal surface of P3 may be the norm. The group presenting positively curved hoof capsules but negatively curved bone surfaces would seem to back this up further, as it is largely responsible for giving the curve in Figure 3.9 its particular shape, giving graphical evidence of relative continuity of bone curvature until a hoof wall curvature of around $0.001mm^{-1}$ is met, above which the bone curvature values undergo rapid ascent. Should it be that positive curvature is indeed the normal state for the dorsal surface of P3 and, importantly, that it remains in this such form in feet with a small degree of opposing hoof capsule curvature until a certain threshold is met, it would not be unreasonable to suggest that changes in bone curvature could occur as a consequence of changes in hoof capsule curvature.

In a state of normal physiological and biomechanical equilibrium, any occurring bone remodelling should be balanced, with equal rates of osteogenesis and osteolysis, and unchanging bone thickness. Augmented magnitudes of biomechanical stress can lead to osteoblastic osteogenesis, often accompanied by osteoclast suppression, resulting in bone thickening. Conversely, sub-normal biomechanical stress magnitudes can lead to bone resorption through osteoclastic osteolysis, and an associated decrease in thickness (Pearson and Lieberman, 2004). Thus, while the correlation between the shapes of the dorsal surfaces of the hoof capsule and of P3 may indicate the existence of inextricable biomechanical forces between the two (Cornette et al., 2015), the observed changes in cortical bone thickness as a function of hoof capsule curvature may serve to further back this up, as well as providing insight into the locality of mechanical strain (Fig. 3.11) (Pearson and Lieberman, 2004). Comparison between the cortical thickness of the lamellar surface in the toe and quarter regions indicated a consistency around the entire surface, irrespective of

curvature (Fig. 3.11A, B, C, D, I and J). With the high rate of rotation but low rate of sinking of P3 as a function of hoof wall curvature, as discussed in section 4.2, it might have been reasonable to expect a thickening in the quarter regions of the lamellar surface in relation to the toe regions in accordance with augmenting curvature, as a result of weakening lamellar bonds in the toe, permitting it to drop. From the lack of any significant correlation, however, could arise the interpretation that the forces applied by the lamellae are consistent around the foot, even when the hoof capsule deviates from the bone.

The toe and quarter regions were found to differ at the level of the solar margin, with a relative increase in cortical thickness in the quarters (Fig 3.11C and D). With its proximity to the weight-baring regions of hoof, this thickening in the quarter region could indicate a relative caudal increase in the share of the foot's load, consistent with the low-healed, slipper-shaped foot and the common "rocked back" stance of an animal afflicted by laminitis.

Distally to proximally, the lamellar surface of the toe was compared, as were the lamellar surface and the solar margin (Fig. 3.11A, B, E, F, I and J). The lack of correlation found in the ratio of distal to proximal lamellar surface of the toe and hoof wall curvature could, in concurrence with the findings of the comparison between the toe and quarter areas of the lamellar surface discussed above, be attributable to a general equilibrium of forces over the entirety of the lamellar surface regardless of the foot's overall pathophysiological state. The conversely strong relationship of the lamellar surface to solar margin ratio with the hoof wall curvature is particularly interesting. If the rotation and/or sinking of P3 were truly the result of the failure of the lamellar suspensory apparatus, one might expect the tensile strain imposed by the lamellae to the parietal surface of the bone to be diminished, and the compressive strain on the solar margin of the "foundered" phalanx against the ground to be augmented. This ought, in time, to lead to a thinning in the lamellar surface and a thickening in the solar margin. However, the antithetical observation that the cortical thickness of the lamellar surface increases in relation to that of the solar margin as hoof wall curvature augments, could indicate that the brunt of the force imbalances may be being borne, not by the solar margin, but by the lamellar surface, perhaps putting the dogma that laminitis is purely the result of failing lamellar bonds under scrutiny.

Another long-standing belief is that the rotation of P3 in an episode of laminitis results from the pull of the DDFT overcoming the hold of the weakened lamellae. If the strain imposed by the DDFT were superior to that inflicted by the lamellae, one may expect to observe a thickening in the flexor surface in relation to the lamellar surface of the toe. In this study, however, this was not observed,

and the cortical thickness ratio of the toe lamellar surface to the flexor surface did not significantly vary in conjunction with hoof wall curvature (Fig 3.11C, D, E, F, G, H, K and L). The flexor surface thickness was also compared to the cortical thickness at the extensor process, and their quotient showed a similar lack of correlation with hoof curvature. Again, one might have expected to see a correlative difference in thickness between the two regions, borne from the differential pulls of the DDFT and the CDET through inference from the DDFT theory, were the pull of the DDFT a major contributing factor.

Finally, the solar surface (Fig 3.11E, F, G, H,K and L), solar margin and lamellar surface were analysed as ratios of P3 as a whole, due to the solar surface's potential reaction with the ground, the observable changes in the solar margin on the CT images and the importance of the lamellar zone in laminitis. Though the solar surface appeared to become thinner as hoof wall curvature increased, such correlation was not backed up by statistical evidence. The cortical thickness of the solar margin was found to significantly decrease in comparison to the rest of the bone as hoof wall curvature augmented. The thickness of the lamellar surface, however, did not bear any apparent relationship to hoof curvature. The lack of change in the thickness of the solar surface may imply that the region is not submitted to larger degrees of stress through laminitic changes to the foot. The decrease in solar margin thickness came not as a surprise, with reports of visible thinning and fractures to the area in chronically laminitic horses, along with a recent study, which utilised μ-CT and histopathology in parallel, reporting an overall osteoclastic thinning of the bone in the laminitic foot (Engiles et al., 2015). While the linear regression trendline's goodness of fit for the lamellar surface ratio was poor, it was of some interest in view of its almost horizontal nature, which could suggest a consistency in thickness irrespective of lamellar pathological state, perhaps suggesting, as above, that the lamellae of the suspensory apparatus do not completely fail in their role.

In addition to the thickening and thinning of bone, and to its deformation on a gross scale, osseous remodelling may take its effect on the trabecular bone. In this study, the trabecular bone's degree of anisotropy was not observed to significantly correlate with hoof wall curvature. The MIL of two of the three eigenvectors were, however, found to significantly increase in conjunction with augmenting hoof curvature and, although not strictly statistically significant (P = 0.0529), the remaining eigenvector did present a similar trend. These observations signify a decrease in trabecular number, with a corresponding enlargement in inter-trabecular pore space, seemingly due to a non-directional elongation of the trabecular rods and/or plates as a function of hoof wall curvature increase.

As part of a study of trabecular bone ontogeny in the proximal head of the human femur, trabecular number and thickness, and bone volume fraction were investigated in trabecular bone CT images from the foetus and youths up to nine years of age, finding an increase in trabecular bone thickness and bone volume fraction, but a decrease in trabecular number at around a year old, coinciding with the onset of unaided walking and, as a consequence load bearing was concluded to be causal of the changes observed (Ryan and Krovitz, 2006). While trabecular thickness and volume fraction could not be accurately measured in the present study, the decrease in trabecular number given by the MIL may suggest that the distal tip beneath the dorsal lamellar surface of P3 is submitted to higher amplitudes of stress in the feet of chronically laminitic horses than in those of their healthy counterparts.

The lack of anisotropy makes it difficult to pinpoint any exact sources of strain, though this information may be deducible from localised variations in cortical thickness. The regions bordering the area from which the trabecular bone was analysed, and with perhaps a greater likelihood of flanking environments from which stresses may take their highest toll therefore, are the lamellar surface, the solar margin, and the solar surface. The solar margin underwent thinning as hoof wall curvature increased, presumably indicative of a diminution of physical strain in that region. While perhaps not significantly, the solar surface also appeared to decrease in thickness as a function of increasing hoof curvature indicating, at least, that an increase in strain in that locality is perhaps unlikely. The lamellar surface thickness remained relatively constant despite varying hoof curvature, and significantly increased in comparison to the solar margin.

As trabecular bone has inferior resilience to tensile as opposed to compressive stresses (Lambers et al., 2014), and as the lamellar surface was the bordering cortical region which did not appear to undergo thinning indicative of stress reduction, it would appear logical that the observed increase in trabecular pore size as a positive function of hoof wall curvature could result from heightened tensile stresses from the lamellar region within the foot. Should this be so, a relatively isotropic increase, such as that observed, would not necessarily be surprising, as the lamellae encircle a large are of P3. Although lamellar surface thickness did not increase as a ratio of P3 as a whole with augmenting hoof wall curvature, it is important to remember that trabecular bone is 10 times more metabolically active than cortical bone (Kini and Nandeesh, 2012), thus a more pronounced change in the former is perhaps to be expected. A trabecular bone reaction indicative of increased tensile strain supports the hypothesis that laminitis could result from the levering of the hoof wall away from the bone, placing the lamellae under tensile stress.

4.4 Vascular Remodelling

Vascular disturbances have long been associated to the pathogenesis of laminitis (Heymering, 2010), and digital venography is a commonly employed technique providing vital information for treatment options and for monitoring their progress (Rucker, 2010). CT images provide higher levels of quantitative information than venograms, enabling the visualisation of discrete areas rather than an overall impression of perfusion rate based on attenuation of contrast agents in numerous vessels simultaneously.

In this study, a comparison in the lumen diameter of the blood vessels of the toe showed that those of the sublamellar plexus significantly decreased in relation to those in the solar plexus as a function of augmenting hoof wall curvature. While it could be suggested that this might be due to the compressive effects of the inward-curving hoof wall, it should be remembered that the dorsal axis of P3 was found to deviate away from the equivalent axis of the hoof wall (rotation), and thus compression due to a lack of space is unlikely.

The post-mortem nature of the samples renders speculation on vasoactivity impossible. The concept of blood vessel stenosis has not apparently been related to equine laminitis, with no mentions found in the literature. Bovine chronic laminitis has, however, been associated with arteriosclerosis, a thickening and hardening of vascular walls (Boosman et al., 1989), which perhaps deserve investigation in relation to equine laminitis. The apparently narrowed lumen of the sublamellar plexus could equally result from a less adequate perfusion and flushing of blood from the vessels resulting from the compromise of other vessels in the circuit.

In reality, the reason for the relative decrease in lumen diameter of the vasculature of the toe sublamellar plexus as opposed to the solar plexus remains unclear without further investigation (see section 4.6.1), which was not possible as the coronet region of many of the feet were compromised due to the tissue extraction for immunohistochemistry. The results should, therefore, be regarded as useful in the exploration of the technique.

Criticism of the fixation methods could arise, as it could be argued that manually pressurising the vessels is subjective and could cause lead to a degree of variability in visible vessel diameter. However, the primary focus on the vasculature in this study was on its gross anatomy, rather than its ultrastructure. Furthermore, by using the ratios of the lumen diameters in the two aforementioned plexuses pertaining to the same foot, rather than making observations on the direct measurements, variabilities arising from the method described were accounted for.

4.5 Papilla Morphology and Keratogenesis

There are few mentions of papilla morphology and size in the literature, with only a brief reference by Pollitt of the holes in the proximal edge of the hoof wall in which the papillae lie, where he describes a depth of 4-5mm (Pollitt, 2004). Given that hoof growth originates from around these papillae (Chapman, 1986), however, that they are highly vascularised structures (Nasu et al., 1998), and that tissue growth in general is dependent on heightened vascularisation (Stocum, 2012), it would seem logical that a correlation between the size of the papillae and the proliferative capacity of the surrounding epidermal tissue could exist.

In this study, synchrotron μ-CT was used to three-dimensionally visualise the papillae of the coronary corium of the toe of a normal equine foot. The papillae of the *strata externum*, *medium* and *internum* were clearly visible at a resolution of 8μm.

In terms of diameter, the papillae of the *stratum externum* were the narrowest, with a mean of 0.026mm, those of the *stratum internum* were middling, with a mean diameter of 0.03272mm, and those of the *stratum medium* the broadest, with a mean of 0.049mm. Observation of the structures – the periople and stratum tectorum, the epidermal lamellae, and the hoof wall – that stem from the papillae of the *stratum externum*, *stratum internum* and *stratum medium* respectively, may provide elucidation on the differences in papilla width in the three strata. For instance, it could be suggested that the *stratum externum* bore the narrowest papillae because the periople whose growth they support is itself narrow.

The shortest papillae were those of the *stratum internum*, with a mean length of 0.682mm, those of middle-length were found in the *stratum externum*, with a mean of 1.642mm, and the longest papillae were those of the *stratum medium*, which had a mean of 5.807mm. In concurrence with papilla length, papilla surface area was at its smallest in the *stratum internum* and at it largest in the *stratum medium*, with mean surface areas of 0.071mm^2 in the *stratum internum*, 0.133mm^2 in *stratum externum*, and 0.891mm^2 in the *stratum medium.* Again, looking at the structures growing around the papillae of each *stratum* should be indicative of the reason for their particular morphology. The hoof wall, for instance, is the thickest and densest of the three regions, and it seems logical that it may require an enhanced surface area for increased proliferative cell support.

While it is important to remember that repetition on a number of equine feet would be necessary for reliable results, the findings discussed here provide some indication of the likely dimensions of equine coronary dermal papillae.

Furthermore, the results reveal the possibility of using a technique that has never previously been utilised for these purposes.

The results of the immunohistochemistry work by Ramzi Al-Agele coupled with the curvature data from this study were indicative of differential growth in positively curved hooves. The ratio of the percentage of P63 positive cells in feet with flat hoof walls was close to one (1.054), indicating a consistency of proliferation around the entire coronet. An increase in cellular proliferation in the quarters/heels in relation to in the toe (ratio of 1.567) was revealed, however, in feet with positively curved hooves. While further experiments would be required to determine causality, this supports the primary project hypothesis that differential growth may lead to capsular deformation due to the solid capsule's reaction to residual mechanical stress.

4.6 Future Research

A principal aim of this study was to investigate the application of μ-CT in the field of laminitis research. The technique revealed many merits, and novel ideas of how it could be applied to the broader project developed as the study progressed. These ideas for future research make use of both laboratory and synchrotron μ-CT sources.

4.6.1 Laboratory M-CT

4.6.1.1 Full Vasculature Analyses

As numerous vascular theories have been proposed in the explanation of the pathogenesis of laminitis (Heymering, 2010), there is warrant for further investigation into variances in the vasculature of the feet of normal horses and those which display characteristics of a chronically laminitic foot. This would involve the calculation of lumen diameter, as carried out in this study, and examination of network layouts in different regions of the foot's vasculature.

The same method of foot collection, preparation and scanning as described above would need to be employed. ROI selections would be made with particular attention to the sublamellar and coronary plexuses cranially and caudally. Calculating the ratio of the means cranially to dorsally for each plexus, differential lumen diameter could be assessed as a function of hoof wall curvature.

Using the Fiji Skeleton plugin (Arganda-Carreras et al., 2010), the binary vasculature image stack, divided into ROIs as above, would be skeletonised, reducing each vessel down to its central voxels. The resulting skeleton would be analysed, giving information on the numbers, locations, and number of branches forming each junction. The number of junctions and branches in a volume could be calculated and, comparing cranial to caudal, related to hoof wall curvature.

4.6.1.2 Microvasculature Analyses

With differential growth as a cause of laminitis being the principle hypothesis of the project, methods permitting the assessment of keratinocyte proliferation in the cranial and caudal coronet regions are of particular interest. As tissue growth is reliant on the delivery of oxygen and nutrients, its occurrence is in association with angiogenesis (Gilbert, 2010, Fraisl et al., 2009). As a means of detecting differential growth therefore, angiogenic differences cranially and caudally could be investigated through examination of the microvasculature of the coronary corium, rendering μ-CT a stand-alone method without further need for histological studies. This investigation would be done using the skeletonisation method described in the section above, and calculating vascular density cranially and caudally.

4.6.2 Synchrotron M-CT

4.6.2.1 Differential Papilla Dimensions

With hoof growth originating from cell proliferation around the dermal papillae (Chapman, 1986), it would not be an unreasonable notion that larger papillae, and therefore a larger surface of interaction with their vasculature, could enable higher rates of proliferation, and therefore growth. In a variety of hooves, the dimensions of the papillae could be measured as described in section 2.8, and differences between those in the toe and heel regions examined as a function of hoof wall curvature.

4.6.2.2 Dynamic Imaging

Dynamic imaging, using contrast-enhanced CT and Magnetic Resonance Imaging (MRI), for the exploration of cerebral and tumour microvasculature is an ever-expanding area of interest (O'Connor et al., 2011). As it stands, such dynamic imaging techniques have not been employed in research into equine foot conditions. However, as a highly vascularised structure which can undergo extreme pathogenic changes, the utilisation of such techniques could revolutionise our understanding of the complex pathologies of the equine foot.

Exploitation of the unique characteristics of a synchrotron radiation source's μ-CT facilities could render dynamic experimentation to fully elucidate the pathogenic mechanisms involved in the development of laminitis and hoof deformity in a whole foot model possible. This would involve the visualisation of cellular changes, notably proliferation, of the epidermal progenitor cells surrounding the coronary dermal papillae of a horse limb artificially maintained metabolically alive, whilst being submitted to a variety of physical and chemical stressors. Synchrotron-based μ-CT offers high spatial resolution which, when wishing to view microscopic components of large, intact specimens, can very rapidly become a limiting factor. The voxel resolution of 8μm achieved in this study provided clear images of the papillae, and the whole-foot nature of the sample demonstrated the feasibility of carrying out experiments of the sort being discussed in terms of visibility of the desired structures. High temporal resolution is another feature of synchrotron-based μ-CT, with elevated photon intensity permitting far greater imaging frequencies than would be achievable through any other x-ray sources. It is this feature that would render dynamic imaging of constantly evolving structures possible. A final requirement for such an experiment is physical space for the set-up of the machinery that would be responsible for keeping the tissues alive, and that which would provide the physical stimuli. The lack of space in a laboratory μ-CT apparatus would render such a set-up impossible, as opposed to the large, flexible layout of a beamline.

To maintain life on a cellular level, the tissue would need to be perfused with a constantly refreshing supply of blood, from immediately post-slaughter through to the completion of the experiment. This would require the preparation of an artificial respiratory and circulatory system, with an oxygenating chamber, water bath and peristaltic pump, to respectively oxygenate, maintain at 38^{o}C, and circulate the blood. Given the rarity of the creation of antibodies targeting allogeneic red blood cells in the horse, and that the mean red blood cell's half-life is of 4.7 hours in the presence of such alloantibodies (Tomlinson et al., 2015), the utilisation of blood from another horse should not be a particular cause for concern, although other blood-related theories also exist which would require careful consideration should such an experiment be undertaken. So as to ensure the freshness of the blood, it could be collected in situ from the university-approved abattoir on the day of the limb collection. The circulatory machine could then be set up with the blood in preparation. The addition of heparin to the blood would prevent its coagulation, though caution would need to be exercised due to heparin's effects on insulin sensitivity, which is particularly relevant due to the nature of the discussed experiment.

Immediately after slaughter, the horse's limb, disarticulated at the knee, would be attached to the circulatory system via cannulation of the lateral and the medial palmar/plantar arteries and veins, and secured in an upright 'standing' position. This circulatory system and mount would need to be designed in such a way as to allow transportation to the synchrotron radiation facility, and its subsequent attachment to the rotating sample stage upon arrival and for the duration of the experiment.

Perfusing the circulating blood with a colloid of Bi_2S_3 nanoparticles (Ai et al., 2011) conjugated with antibodies targeting stem cell membrane marker CD44 (Broeckx et al., 2014), ROI scans of the epidermal borders of the coronary papillae would be performed both dorsally and in the lateral and medial quarters. The CD44 antibodies will cause the Bi_2S_3 to conglomerate around proliferative cells, including the epidermal progenitor cells responsible for hoof growth, and the large attenuation coefficient of Bi_2S_3 conferred by bismuth's high atomic mass will render regions of high proliferation brighter on the CT images than areas in which proliferation is lower. Comparing areas of brightness within the epidermal junction dorsally to laterally/medially will offer insight into the existence of differential growth.

Numerous chemical triggers of laminitis, such as insulin, cortisol, black walnut extract and so on, have been identified, but the pathogenic pathway remains elusive, and any speculative cause evidentially lacking. The underpinning hypothesis of the project to which these tomographic studies belong is that

laminitis may occur as a result of the strain imposed on the lamellae by significant hoof-growth anomalies; notably a higher growth rate in the quarter and heel regions than in the toe. It would not be absurd to suggest that the aforementioned chemical triggers could cause, either directly or indirectly, a change in the proliferation rate of the epidermal progenitor cells. The dynamic tomographic experiment described would provide a means of assessing proliferation in response to a chemical trigger over time, through repeated perfusions of varying concentrations of the chemical and of Bi_2S_3 colloid in concurrence with regular scans (e.g. every 30 minutes) over a 24h period.

Alongside the scans and measurements indicative of cellular proliferation, further scans could provide information on the pathogenic status of the lamellar zone. This would involve quantifying any displacement of P3 with respect to the hoof wall by employing a second series ROI scans of the most distal portion of the lamellar zone, at the point of P3, either directly before or after each scan of the coronet zones.

Overloading of the limb is another observed cause of laminitis, such as is seen in supporting limb laminitis. While it could be considered that this is purely due to a physical overload of the lamellae beyond the scope of their elasticity, or that such an overload could result in the compromise of the vasculature, the notion that physical stimuli can lead to cellular proliferation could also be invoked. Therefore, again using a perfusion of Bi_2S_3 colloid in the blood stream, scans of the coronary papillae could be performed on a foot submitted to varying amounts of vertical compressive stress to assess its effect on cell proliferation.

In addition to providing insight into the pathogenic pathway of the disease in an unprecedented real-time, "*semi-vivo*" model, the discussed experiment would provide information on the doses involved in the instigation of pathogenic changes in response to chemical triggers, as opposed to the supra-physiological doses ordinarily employed, and on the effect of physical loading. Furthermore, an experiment using artificially-sustained tissues sourced as bi-products from animals being slaughtered for other purposes renders intensive testing on live tissues without causing suffering to live animals possible.

5 Conclusions

With the aims of furthering understanding of the factors involved in hoof growth, uncovering details on the anatomical characteristics of the equine foot, linking deformities of the hoof capsule to abnormalities in the internal structures of the foot, and developing new methodologies, the utilisation of μ-CT in this study was successful. Scanning of equine feet bore data on the determination of the foot's pathological status, the condition of the bone and vasculature, as well as allowing the extraction of detailed anatomical images and revealing the potential for further investigation. The synchrotron data showed that detailed images of the dermal papillae and their surroundings were possible. This, coupled with the properties of synchrotron radiation, opens the possibilities for future research, with the potential for dynamic hoof imaging.

The high contrast of the vasculature on the CT images suggested that the flushing, pressurising and fixing methods employed are of value for such studies. The observed differences in the mean lumen diameter of the sublamellar and solar plexuses as a function of hoof wall curvature indicated the merit of future research into the vasculature of the foot. The laboratory CT and synchrotron imaging, and software developed, could be utilised to investigate areas previously imaged using histological and gross anatomical techniques such as measuring vasculature and angiogenesis, bone morphology, assessing cell proliferation and identifying soft tissue structure and morphology.

In the definition of the foot's pathological status, measurements of hoof angle and of the rotation of P3 correlated with dorsal hoof wall curvature, suggesting that this could be a good descriptor of chronic laminitis. Dorsal hoof wall curvature was therefore used as the sole physical descriptor with which all other measurements in this study were compared. Interestingly, despite theories on the sinking of P3 being potentially linked to laminitis, at the curvatures observed in the studies, there was no correlation between P3 sinking and any of the other factors measured. It should be noted that horses with so called 'fatal sinker's syndrome' (depressed P3) would, for legal reasons, be most likely to be humanely destroyed on-site rather taken to an abattoir, and therefore these cases might not be observed.

Bone morphology was found to vary in correlation with hoof wall curvature. One observation was a similar curvature of P3 to that of the hoof wall in feet with a hoof wall curvature in excess of $0.001mm^{-1}$, whereas the bone remained more consistently straight with hoof wall curvatures below this amount. It is possible that the hoof curvature does not initially have an effect on the P3 bone but that, in excess of the stated threshold, it starts to exert its forces through the

intermediary of the lamellae. In turn, it is possible that interactions between the capsule and P3 place further stresses on the lamellae. In addition to the P3 curvature results, variations in cortical bone thickness were observed in correlation with increasing hoof curvature. These results could indicate a lack of involvement of the flexor tendon in the rotation of P3. Cortical bone thickness at the solar margin decreased as hoof curvature increased, despite more ground force potentially being applied due to rotation, and the lamellae surface, which stayed consistent in thickness, increased in thickness in proportion to the solar margin with augmenting curvature. Therefore, although rotation may have taken place, the lamellae may have stopped the tip of P3 from sinking completely. This evidence potentially disputes the notion of lamellar degradation as a causal factor of laminitis. Another key bone morphology finding of this study showed an increase in trabecular pore space under the lamellar surface of P3, that could suggest heightened tensile strain from the lamellae with increasing hoof curvature, again suggesting that lamellar damage may be an effect, rather than a cause, of laminitis.

This study has provided insights into the applications of μ-CT and Physical Biology in the field of Veterinary Science. This research highlights the importance of bone and soft tissue structure, conformation and integrity in the equine foot, and their effects upon each other. The structural morphology findings suggest that further studies are required to investigate bone, soft tissue and vasculature in the equine limb. Investigations into hoof deformation, growth, conformation and development, and also disorders such as laminitis, would benefit from the techniques developed and described in this research.

Publications

An investigation of causes and outcomes of hoof growth rate and their relation to equine hoof conformation, Ramzi Al-Agele, **Emily Paul,** Catrin Rutland, and Cyril Rauch, European Association of Veterinary Anatomists, Poland, 2015.

Physics of nail conditions: why will horses always do better at the "pointe" technique than ballet dancers? by Ramzi Al-Agele, **Emily Paul,** Tom Ryan, Craig Sturrock , John Burford, Michael Drakopoulos, Robert Atwood, Nghia Vo, Paula Williams, Catrin Rutland, and Cyril Rauch, submitted to *Phys. Biol.*

References

AI, K., LIU, Y., LIU, J., YUAN, Q., HE, Y. & LU, L. 2011. Large-Scale Synthesis of Bi2S3 Nanodots as a Contrast Agent for In Vivo X-ray Computed Tomography Imaging. *Advanced Materials,* 23**,** 4886-4891.

ALLEN, M. R., HOCK, J. M. & BURR, D. B. 2004. Periosteum: biology, regulation, and response to osteoporosis therapies. *Bone,* 35**,** 1003-12.

ANONYMOUS 2004. Advice on Prevention and Management of Laminitis. Kenilworth: The British Horse Society.

ARCHER, S., BELL, N. & HUXLEY, J. 2010. Lameness hi UK dairy cows: a review of the current status. *In Practice,* 32**,** 492-504.

ARGANDA-CARRERAS, I., FERNANDEZ-GONZALEZ, R., MUNOZ-BARRUTIA, A. & ORTIZ-DE-SOLORZANO, C. 2010. 3D reconstruction of histological sections: Application to mammary gland tissue. *Microsc Res Tech,* 73**,** 1019-29.

ARNETT, T. 2003. Regulation of bone cell function by acid-base balance. *Proc Nutr Soc,* 62**,** 511-20.

BALDWIN, G. I. & POLLITT, C. C. 2010. Progression of venographic changes after experimentally induced laminitis. *Vet Clin North Am Equine Pract,* 26**,** 135-40.

BARKER, Z. E., LEACH, K. A., WHAY, H. R., BELL, N. J. & MAIN, D. C. 2010. Assessment of lameness prevalence and associated risk factors in dairy herds in England and Wales. *J Dairy Sci,* 93**,** 932-41.

BAXTER, G. M. (ed.) 2011. *Manuel of Equine Lameness,* Chichester: John Wiley and Sons.

BAYLISS, L., MAHONEY, D. J. & MONK, P. 2012. Normal bone physiology, remodelling and its hormonal regulation. *Surgery (Oxford),* 30**,** 47-53.

BELL, N. 2015. *Lameness Control in Dairy Herds, Part 1 - Practical Foot Trimming (Dutch 5 Step Method)* [Online]. National Animal Disease Information Service. Available: http://www.nadis.org.uk/bulletins/lameness-control-in-dairy-herds/part-1-practical-foot-trimming-(dutch-5-step-method).aspx [Accessed 10. 11. 2015].

BODEN, E. (ed.) 2007. *Black's Student Veterinary Dictionary,* London: A & C Black Publishers Ltd.

BOOSMAN, R., NEMETH, F., GRUYS, E. & KLARENBEEK, A. 1989. Arteriographical and pathological changes in chronic laminitis in dairy cattle. *Vet Q,* 11**,** 144-55.

BRAGULLA, H. 2003. Fetal development of the segment-specific papillary body in the equine hoof. *J Morphol,* 258**,** 207-24.

BROECKX, S. Y., MAES, S., MARTINELLO, T., AERTS, D., CHIERS, K., MARIEN, T., PATRUNO, M., FRANCO-OBREGON, A. & SPAAS, J. H. 2014. Equine epidermis: a source of epithelial-like stem/progenitor cells with in vitro and in vivo regenerative capacities. *Stem Cells Dev,* 23**,** 1134-48.

CHAPMAN, R. E. 1986. Hair, Wool, Quill, Nail, Claw, Hoof, and Horn. *In:* BEREITER-HAHN, J., MATOLTSY, A. G. & RICHARDS, K. S. (eds.) *Biology of the Integument.* Springer Berlin Heidelberg.

CLARKE, B. 2008. Normal bone anatomy and physiology. *Clin J Am Soc Nephrol,* 3 Suppl 3**,** S131-9.

CORNETTE, R., TRESSET, A. & HERREL, A. 2015. The shrew tamed by Wolff's law: do functional constraints shape the skull through muscle and bone covariation? *J Morphol,* 276**,** 301-9.

CRIPPS, P. J. & EUSTACE, R. A. 1999. Radiological measurements from the feet of normal horses with relevance to laminitis. *Equine Vet J,* 31**,** 427-32.

D'ARPE, L. & BERNARDINI, D. 2010. Digital venography in horses and its clinical application in Europe. *Vet Clin North Am Equine Pract,* 26**,** 339-59.

DARADKA, M. & POLLITT, C. C. 2004. Epidermal cell proliferation in the equine hoof wall. *Equine Vet J,* 36**,** 236-41.

DAVIES, H. M. S. & PHILIP, C. 2007. Gross anatomy of the equine digit. *In:* FLOYD, A. E. & MANSMANN, R. A. (eds.) *Equine Podiatry.* Missouri: Saunders Elsevier.

DAVIES, H. M. S., PHILIP, C. J. & MERRITT, J. S. 2007. Functional anatomy of the equine digit: determining function from structure. *In:* FLOYD, A. E. & MANSMANN, R. A. (eds.) *Equine Podiatry.* Missouri: Saunders Elsevier.

DELANY, A. M. & CANALIS, E. 2001. The metastasis-associated metalloproteinase stromelysin-3 is induced by transforming growth factor-beta in osteoblasts and fibroblasts. *Endocrinology,* 142**,** 1561-6.

DOUBE, M., KLOSOWSKI, M. M., ARGANDA-CARRERAS, I., CORDELIERES, F. P., DOUGHERTY, R. P., JACKSON, J. S., SCHMID, B., HUTCHINSON, J. R. & SHEFELBINE, S. J. 2010. BoneJ: Free and extensible bone image analysis in ImageJ. *Bone,* 47**,** 1076-9.

ENGILES, J. B. 2010. Pathology of the distal phalanx in equine laminitis: more than just skin deep. *Vet Clin North Am Equine Pract,* 26**,** 155-65.

ENGILES, J. B., GALANTINO-HOMER, H. L., BOSTON, R., MCDONALD, D., DISHOWITZ, M. & HANKENSON, K. D. 2015. Osteopathology in the Equine Distal Phalanx Associated With the Development and Progression of Laminitis. *Vet Pathol,* 52**,** 928-44.

EURELL, J. A. C. 2004. *Veterinary Histology,* Wyoming, Teton NewMedia.

EUSTACE, R. A. 2010. Clinical presentation, diagnosis, and prognosis of chronic laminitis in Europe. *Vet Clin North Am Equine Pract,* 26**,** 391-405.

FAWC. 2011. *Opinion on Lameness in Sheep* [Online]. Farm Animal Welfare Council. Available: http://webarchive.nationalarchives.gov.uk/20121007104210/http://www.fawc.org.uk/pdf/sheep-lameness-opinion-110328.pdf [Accessed 10. 11. 2015].

FLOYD, A. E. 2007. Grading the laminitic horse. *In:* FLOYD, A. E. & MANSMANN, R. A. (eds.) *Equine Podiatry.* Missouri: Saunders Elsevier.

FRAISL, P., MAZZONE, M., SCHMIDT, T. & CARMELIET, P. 2009. Regulation of angiogenesis by oxygen and metabolism. *Dev Cell,* 16**,** 167-79.

FRANKLIN, K., MUIR, P., SCOTT, T., WILCOCKS, L. & YATES, P. 2010. *Introduction to Biological Physics for the Health and Life Sciences,* Chichester, Wiley.

GAGE, G. J., KIPKE, D. R. & SHAIN, W. 2012. Whole animal perfusion fixation for rodents. *J Vis Exp*.

GAO, H. J. 2006. Application of fracture mechanics concepts to hierarchical biomechanics of bone and bone-like materials. *International Journal of Fracture,* 138**,** 101-137.

GILBERT, S. F. 2010. *Developmental Biology,* Massachusetts, Sinauer Associates.

GOODY, P. C. 2000. *Horse Anatomy: a pictorial approach to equine structure,* London, J. A. Allen.

HEYMERING, H. W. 2010. 80 causes, predispositions, and pathways of laminitis. *Vet Clin North Am Equine Pract,* 26**,** 13-9.

HIGGINS, C. B. & DEROOS, A. 2006. *MRI and CT of the Cardiovascular System,* Pennsylvania, Lippincott Williams & Wilkins.

HILL, C. & KLIMESH, R. 2009. *Horse Hoof Care,* Massachusetts, Storey Publishing.

HUNT, R. J. & WHARTON, R. E. 2010. Clinical presentation, diagnosis, and prognosis of chronic laminitis in North America. *Vet Clin North Am Equine Pract,* 26**,** 141-53.

IOLASCON, G., NAPOLANO, R., GIOIA, M., MORETTI, A., RICCIO, I. & GIMIGLIANO, F. 2013. The contribution of cortical and trabecular tissues to bone strength: insights from denosumab studies. *Clin Cases Miner Bone Metab,* 10**,** 47-51.

IRELAND, J. L., CLEGG, P. D., MCGOWAN, C. M., PLATT, L. & PINCHBECK, G. L. 2011. Factors associated with mortality of geriatric horses in the United Kingdom. *Prev Vet Med,* 101**,** 204-18.

KINAHAN, P. E., HASEGAWA, B. H. & BEYER, T. 2003. X-ray-based attenuation correction for positron emission tomography/computed tomography scanners. *Seminars in Nuclear Medicine,* 33**,** 166-179.

KINI, U. & NANDEESH, B. N. 2012. Physiology of Bone Formation, Remodeling, and Metabolism. *In:* FOGELMAN, I., GNANASEGARAN, G. & VAN DER WALL, H. (eds.) *Radionuclide and Hybrid Bone Imaging.* Springer Berlin Heidelberg.

LAMBERS, F. M., BOUMAN, A. R., TKACHENKO, E. V., KEAVENY, T. M. & HERNANDEZ, C. J. 2014. The effects of tensile-compressive loading mode and microarchitecture on microdamage in human vertebral cancellous bone. *Journal of Biomechanics,* 47**,** 3605-3612.

MILLER, W. H., GRIFFIN, C. E. & CAMPBELL, K. L. 2013. *Muller and Kirk's Small Animal Dermatology,* Missouri, Elsevier.

MISHRA, P. C. & LEACH, D. H. 1983. Extrinsic and intrinsic veins of the equine hoof wall. *J Anat,* 136**,** 543-60.

MIZUTANI, R. & SUZUKI, Y. 2012. X-ray microtomography in biology. *Micron,* 43**,** 104-15.

MURRAY, B. & WILSON, D. J. 2001. A study of metabolites as intermediate effectors in angiogenesis. *Angiogenesis,* 4**,** 71-7.

NAKAHAMA, K. 2010. Cellular communications in bone homeostasis and repair. *Cell Mol Life Sci,* 67**,** 4001-9.

NASU, T., YAMANAKA, T., NAKAI, M. & OGAWA, H. 1998. Scanning electron microscopic study of the vascular supply of the equine hoof. *J Vet Med Sci,* 60**,** 855-8.

NIEUWHOF, G. J. & BISHOP, S. C. 2005. Costs of the major endemic diseases of sheep in Great Britain and the potential benefits of reduction in disease impact. *Animal Science,* 81**,** 23-29.

O'BRIEN, K. 2007. *Essential Horse Health,* Ohio, David & Charles.

O'CONNOR, J. P., TOFTS, P. S., MILES, K. A., PARKES, L. M., THOMPSON, G. & JACKSON, A. 2011. Dynamic contrast-enhanced imaging techniques: CT and MRI. *Br J Radiol,* 84 Spec No 2**,** S112-20.

PAZZAGLIA, U. E., CONGIU, T., SIBILIA, V. & QUACCI, D. 2014. Osteoblast-osteocyte transformation. A SEM densitometric analysis of endosteal apposition in rabbit femur. *J Anat,* 224**,** 132-41.

PEACOCK, M. 2010. Calcium metabolism in health and disease. *Clin J Am Soc Nephrol,* 5 Suppl 1**,** S23-30.

PEARSON, O. M. & LIEBERMAN, D. E. 2004. The aging of Wolff's "law": ontogeny and responses to mechanical loading in cortical bone. *Am J Phys Anthropol,* Suppl 39**,** 63-99.

PETERSEN, O. H. (ed.) 2007. *Lecture Notes on Human Physiology,* Oxford: Blackwell Publishing.

PHNG, L. K. & GERHARDT, H. 2009. Angiogenesis: a team effort coordinated by notch. *Dev Cell,* 16**,** 196-208.

POLLITT, C. C. 1994. The basement membrane at the equine hoof dermal epidermal junction. *Equine Vet J,* 26**,** 399-407.

POLLITT, C. C. Equine Laminitis: a Revised Pathophysiology. Annual Convention of the American Association of Equine Practitioners, 1999 Lexington. American Association of Equine Practitioners, 188-192.

POLLITT, C. C. 2004. Anatomy and physiology of the inner hoof wall. *Clinical Techniques in Equine Practice,* 3**,** 3-21.

POLLITT, C. C. 2007. Microscopic anatomy and physiology of the hoof. *In:* FLOYD, A. E. & MANSMANN, R. A. (eds.) *Equine Podiatry.* Missouri: Saunders Elsevier.

POLLITT, C. C. 2010. The anatomy and physiology of the suspensory apparatus of the distal phalanx. *Vet Clin North Am Equine Pract,* 26**,** 29-49.

POYNTON, A. 2015. *Treatment of Laminitis* [Online]. Kenilworth: British Farriers and Blacksmiths Association. [Accessed 24. 11. 2015].

PREIBISCH, S., SAALFELD, S. & TOMANCAK, P. 2009. Globally optimal stitching of tiled 3D microscopic image acquisitions. *Bioinformatics,* 25**,** 1463-5.

PROTHERO, D. R. 2001. Perissodactyla (Odd-Toed Ungulates Including Horses, Rhinoceroses and Tapirs). *eLS.* John Wiley & Sons, Ltd.

PUCHALSKI, S. M. 2012. Advances in equine computed tomography and use of contrast media. *Vet Clin North Am Equine Pract,* 28**,** 563-81.

RASBAND, W. 2003. *Grid Overlay Macro* [Online]. National Institutes of Health. Available: http://imagej.net/macros/examples/Grid_Overlay.txt [Accessed 17. 08. 2015].

RAUCH, C. & CHERKAOUI-RBATI, M. 2014. Physics of nail conditions: why do ingrown nails always happen in the big toes? *Phys Biol,* 11**,** 066004.

REDDEN, R. F., LITTLE, D. & SCHRAMME, M. C. 2007. Diagnostic Imaging: radiographic views of most value to farriers. *In:* FLOYD, A. E. & MANSMANN, R. A. (eds.) *Equine Podiatry.* Missouri: Saunders Elsevier.

RENDLE, D. 2014. *Laminitis in Horses* [Online]. National Animal Disease Information Service (NADIS). Available: http://www.nadis.org.uk/bulletins/laminitis-in-horses.aspx?altTemplate=PDF [Accessed 10. 11. 2015].

RENNIE, R. (ed.) 2015. *A dictionary of Physics,* Oxford: Oxford University Press.

ROONEY, J. R. 2007. Functional anatomy of the foot. *In:* FLOYD, A. E. & MANSMANN, R. A. (eds.) *Equine Podiatry.* Missouri: Saunders.

RUCKER, A. 2007. The digital venogram. *In:* FLOYD, A. E. & MANSMANN, R. A. (eds.) *Equine Podiatry.* Missouri: Saunders Elsevier.

RUCKER, A. 2010. Equine venography and its clinical application in North America. *Vet Clin North Am Equine Pract,* 26**,** 167-77.

RYAN, T. M. & KROVITZ, G. E. 2006. Trabecular bone ontogeny in the human proximal femur. *J Hum Evol,* 51**,** 591-602.

SANTORO, D. 2012. An approach to diseases of the claw and claw folds. *In:* JACKSON, H. & MARSELLA, R. (eds.) *BSAVA Manual of canine and feline dermatology.* 3rd ed. Glouster: British Small Animal Veterinary Association.

SCHINDELIN, J., ARGANDA-CARRERAS, I., FRISE, E., KAYNIG, V., LONGAIR, M., PIETZSCH, T., PREIBISCH, S., RUEDEN, C., SAALFELD, S., SCHMID, B., TINEVEZ, J. Y., WHITE, D. J., HARTENSTEIN, V., ELICEIRI, K., TOMANCAK, P. & CARDONA, A. 2012. Fiji: an open-source platform for biological-image analysis. *Nat Methods,* 9**,** 676-82.

SLATER, J. 2014. *National Equine Health Survey* [Online]. The Blue Cross. Available: http://www.bluecross.org.uk/files/nehs-report-may-2014.pdf [Accessed 24. 10. 2014].

STAPOR, P., WANG, X., GOVEIA, J., MOENS, S. & CARMELIET, P. 2014. Angiogenesis revisited - role and therapeutic potential of targeting endothelial metabolism. *J Cell Sci,* 127**,** 4331-41.

STEVENSON, A. & WAITE, M. (eds.) 2011. *Concise Oxford Dictionary,* Oxford: Oxford University Press.

STOCUM, D. L. 2012. *Regenerative Biology and Medicine,* London, Elsevier.

TAICHMAN, R. S. 2005. Blood and bone: two tissues whose fates are intertwined to create the hematopoietic stem-cell niche. *Blood,* 105**,** 2631-9.

TAYLOR, D., SPERANDEO, A., SCHUMACHER, J., PASSLER, T., WOOLDRIDGE, A., BELL, R., COONER, A., GUIDRY, L., MATZ-CREEL, H., RAMEY, I. & RAMEY, P. 2014. Clinical Outcome of 14 Obese, Laminitic Horses Managed with the Same Rehabilitation Protocol. *Journal of Equine Veterinary Science,* 34**,** 556-564.

TOMLINSON, J. E., TABERNER, E., BOSTON, R. C., OWENS, S. D. & NOLEN-WALSTON, R. D. 2015. Survival Time of Cross-Match Incompatible Red Blood Cells in Adult Horses. *J Vet Intern Med,* 29**,** 1683-8.

VAN EPS, A. W. 2010. Acute laminitis: medical and supportive therapy. *Vet Clin North Am Equine Pract,* 26**,** 103-14.

WEGST, U. G., BAI, H., SAIZ, E., TOMSIA, A. P. & RITCHIE, R. O. 2015. Bioinspired structural materials. *Nat Mater,* 14**,** 23-36.

WILLMOTT, P. 2011. *An introduction to synchrotron radiation: techniques and applications,* Chichester, John Wiley and Sons.

Appendices

Appendix I – Curvature/Angle Relationship Calculations

To deduce the equation for the centre of curvature, two important rules were kept in mind. These were Pythagoras' theorem (eq. A.1) and that a right angle is equal to a half of pi radians (eq. A.2).

$$(x - x_0)^2 + (y - y_0)^2 = R^2 \quad \text{(A.1 2.4.3.2)}$$

$$\theta + \alpha = \frac{\pi}{2} \quad \text{(A.2 2.4.3.3)}$$

where x and y are the coordinate pair of any point on the arc, and x_0 and y_0 are the coordinate pair of the centre of curvature.

As equation A.1 is applicable to any point on the arc, the two extremities give rise to equations A.3 and A.4.

$$(x_A - x_0)^2 + (y_A - y_0)^2 = R^2 \quad \text{(A.3 2.4.3.4)}$$

$$(x_B - x_0)^2 + (y_B - y_0)^2 = R^2 \quad \text{(A.4 2.4.3.5)}$$

where x_A and y_A are the coordinate pair of the point on the arc corresponding to the distal tip of the hoof, and x_B and y_B are the coordinate pair of the point on the arc corresponding to the proximal point of the hoof.

Rearranging equation A.1 produces equation A.5.

$$y = y_0 \pm \sqrt{R^2 - (x - x_0)^2} \quad \text{(A.5 2.4.3.6)}$$

The following stages differ depending on whether the foot's curvature is positive or negative, and the following workings out apply to those with positive curvature. When positively curved, the sign from equation A.5 becomes negative (eq. A.6).

$$y = y_0 - \sqrt{R^2 - (x - x_0)^2} \quad \text{(A.6)}$$

Differentiating, this gave eq. A.7 then A.8

$$\frac{dy}{dx} = \frac{x - x_0}{\sqrt{R^2 - (x - x_0)^2}} \quad \text{(A.7)}$$

$$\tan\theta = \frac{x_A - x_0}{\sqrt{R^2 - (x_A - x_0)^2}} \quad \text{(A.8)}$$

With eq. A.2 in mind, eq. A.8 gave eq. A.9.

$$\tan\theta = \tan\left(\frac{\pi}{2} - \alpha\right) = \frac{1}{\tan\alpha} \tag{A.9}$$

Noting the Pythagorean trigonometric identity (eq. A.10), equations A.11 to A.20 were borne.

$$\cos^2\alpha + \sin^2\alpha = 1 \tag{A.10}$$

$$\Leftrightarrow 1 + \tan^2\alpha = \frac{1}{\cos^2\alpha} \tag{A.11}$$

$$\Leftrightarrow \tan^2\alpha = \frac{1 - \cos^2\alpha}{\cos^2\alpha} \tag{A.12}$$

$$\Leftrightarrow \frac{1}{\tan^2\alpha} = \frac{\cos^2\alpha}{1 - \cos^2\alpha} \tag{A.13}$$

$$\Leftrightarrow \frac{(x_A - x_0)^2}{R^2 - (x_A - x_0)} = \frac{\cos^2\alpha}{1 - \cos^2\alpha} \tag{A.14}$$

$$\frac{(x_A - x_0)^2}{R^2 - (x_A - x_0)^2} = \cos^2\alpha\left[1 + \frac{(x_A - x_0)^2}{R^2 - (x_A - x_0)}\right] \tag{A.15}$$

$$\cos^2\alpha = \frac{(x_A - x_0)^2}{R^2} \tag{A.16}$$

$$1 = \frac{(x_A - x_0)\langle C\rangle}{\cos\alpha} \tag{A.17}$$

$$\Leftrightarrow (y_A - y_0) = -\sqrt{R^2 - (x_A - x_0)^2} \tag{A.18}$$

$$(y_B - y_0) = -\sqrt{R^2 - (x_B - x_0)^2} \tag{A.19}$$

$$\Leftrightarrow y_A - y_B = -\sqrt{R^2 - (x_A - x_0)^2} + \sqrt{R^2 - (x_B - x_0)^2} \tag{A.20}$$

The equation (A.20) was then rearranged (A.21) and solved using Microsoft Excel.

$$\sqrt{R^2 - (x_B - x_0)^2} - \sqrt{R^2 - (x_A - x_0)^2} - (y_A - y_B) = 0 \tag{A.21}$$

Appendix II – Anatomical Movies DVD

For the 3D rotating movies referred to in the text, please insert the DVD into the computer drive and open with Windows Media Player. Choose “select title” and use the arrows to navigate.

Appendix III – Immunohistochemistry Protocol

This protocol was carried out, and provided by Ramzi Al-Agele, PhD student of Dr Cyril Rauch and Dr Catrin Rutland, University of Nottingham.

"The antibody p63 (Anti p63 antibody, rabbit polyclonal [N2C1] Gene Text, USA) was utilised to visualise proliferating cells within the horse hoof tissue. PFA fixed specimens were washed in PBS, then dH_2O for 1hr and dehydrated in a series of graded ethanol at room temperature, then immersed in xylene for 3 hrs, and left in paraffin wax overnight. Samples were then orientated and embedded in paraffin blocks (EG1160 embedding station, Leica, Germany). Paraffin blocks were trimmed and serially sectioned using a microtome (Leica RM2255 Microsystems, Germany) at 8µm and mounted onto polysine coated slides (Fisher Scientific, UK).

Immunohistochemistry was carried out using p63 antibody (Anti p63 antibody, rabbit polyclonal [N2C1] Gene Text, USA). Sections were incubated at 60˚C for 15min, dewaxed in xylene for 5min, rehydrated via a series of graded ethanols 100% 5min; 90% 5min; 70% 5min and washed in dH_2O for 5min. Antigen retrieval was performed via a digital electric microwave, cooker (800W Compact Microwave, Sunny, China) in sodium citrate buffer solution pH6; (dilute 1mol $Na_3C_6H_5O_7$/ 10ml dH_2O) for 20min followed H_2O for 5min. Specimens were incubated with peroxidase block (Novocostra, Leica (Novolink™ Polymer Detection System, Novocastra, Leica Biosystems Newcastle, Ltd, NE128EW, UK), two drops/each slide for 30min at room temperature, followed by washing in PBS 2X 5min. Protein block (Novocostra, Leica (Novolink™ Polymer Detection System, Novocastra, Leica Biosystems Newcastle, Ltd.UK) were added to all sections and incubated for 30min. Sections were then incubated with primary antibody p63 (Anti p63 antibody, rabbit polyclonal [N2C1] Gene Text, USA) diluted in 5% FCS and covered with parafilm for 1hr at room temperature; negative control slides received FCS only. The primary antibody p63 was diluted into either 1:100, 1:300 or 1:500 in 5% FCS (Sigma® Life Science, Germany) by mixing 1µl p63/ 99µl FCS (1:100), 0.333µl p63/ 100µl FCS (1:300) and 1µl p63/ 499µl FCS (1:500). Following primary antibody incubation, slides were washed with PBS 2X 5min. Three drops of post primary (Novolink™ Polymer Detection System, Leica Biosystems, UK) were applied and incubated for 30min followed by washed with PBS 1X 5min then after three drops of polymer (Novolink™ Polymer Detection System, Leica Biosystems, UK) were added and incubated for 30min then washed with PBS 1X 5min. Sections were stained with chromagen solution (20µl Chromogen, DAB/1ml Leica substrate buffer solution, UK) for 2X 5min, followed by a wash in H_2O for 5min. Sections were counterstained with Mayer's haematoxylin (Sigma Aldrich, UK) for 10sec in order to contrast the nuclei which then appear purple, blued in tap water then rinsed in H_2O for 5min.

Sections were dehydrated with ethanol graded (70% 3min; 90% 3min; 100% 3min) finally dipped in xylene for 3min and mounted with glass coverslips using the DPX mounting medium. Sections were taken throughout the tissue and two sections photomicrographed (20X Mag. DM 5000B, Leica, Germany). Five systematic random photomicrographs were taken from each tissue section. This immunostain enabled visualisation of proliferating (stained brown) vs non-proliferating cells (stained purple). Every cell was counted and identified as either proliferating or non-proliferating and the mean±standard error of the mean was calculated for each sample using Excel software (Microsoft Windows, Microsoft Corporation, USA) and graphs constructed using GraphPad software (Prism 6, GraphPad Software, Inc., USA)."